Chalcophile elements track the fate of sulfur at Kīlauea Volcano, Hawai'i

Penny E. Wieser*[1], Frances Jenner[2], Marie Edmonds[1], John Maclennan[1], and Barbara E. Kunz[2].

[1]Department of Earth Sciences, University of Cambridge, Downing Street, Cambridge, UK, CB2 3EQ.
[2]School of Environment, Earth and Ecosystem Sciences, The Open University, Walton Hall, 7 Milton Keynes, Buckinghamshire, MK7 6AA.
Corresponding Author: pew26@cam.ac.uk
https://doi.org/10.1016/j.gca.2020.05.018

Abstract

Chalcophile element concentrations in melt inclusions and matrix glasses may be used to investigate low pressure degassing processes, as well as sulfide saturation during crustal fractionation, and mantle melting. Erupted products from Kīlauea Volcano, Hawaii record three stages of sulfide saturation (in the mantle, crust, and within lava lakes), separated by episodes of sulfide resorption (i.e., sulfide undersaturation) during ascent through the thick Hawaiian lithosphere, and during syn-eruptive degassing. The presence of residual sulfides in the mantle source throughout the melting interval accounts for the high S concentrations of Kīlauean primary melts (1387–1600 ppm). Residual sulfides retain chalcophile elements during melting, decoupling the variability of these elements in high MgO melts from that of lithophile elements. Decompression associated with magma ascent through the thick Hawaiian lithosphere drives an increase in the sulfide concentration at sulfide saturation ($SCSS^{2-}$), resulting in shallow storage reservoirs (∼1–5 km depth) being supplied with sulfide-undersaturated melts. A drop in temperature, coupled with major element changes during the fractionation of olivine, causes the $SCSS^{2-}$ to decrease. Combined with an increase in melt S contents during fractionation, this initiates a second stage of sulfide saturation at relatively high MgO contents (∼12 wt%). Syn-eruptive degassing of S drives the resorption of sulfides in contact with the carrier liquid. The covariance structure of Cu, MgO and Ni contents in melt inclusions and matrix glasses indicates that the dissolution of sulfides effectively liberates sulfide-hosted Cu and Ni back into the melt, rather than the vapour phase. The contrasting behaviour of Cu, Ni, Se and S during sulfide resorption indicates that the chalcophile element signature of the Kīlauean plume is largely controlled by silicate melt-vapour partitioning, rather than sulfide-vapour partitioning. The participation of dense sulfide liquids in shallow degassing processes may result from their direct attachment to buoyant vapour bubbles, or olivine crystals which were remobilized prior to eruption. Sulfide resorption obscures the textural and chemical record of sulfide saturation in matrix glasses, but not in melt inclusions, which are isolated from this late-stage release of chalcophile elements. The partitioning of S between the dissolving sulfide, melt and the vapour phase accounts for approximately 20% of the total S release into the atmosphere.

Please cite the published version in GCA: Wieser et al., 2020,
https://doi.org/10.1016/j.gca.2020.05.018

1 Introduction

Volcanic eruptions emit vast quantities of sulfur (S) and sulfur-loving (chalcophile) elements to the atmosphere, causing perturbations to the global climate system and regional air quality (Robock, 2000; Witham and Oppenheimer, 2004). For example, during the last 35 years, the near-continuous effusion of lava at Kīlauea Volcano, Hawaii has released globally significant amounts of S to the lower troposphere, culminating in fluxes of >50,000 t/day SO_2 during the lower East Rift Zone eruption in 2018 (Neal et al., 2019). These emissions have serious implications for regional air quality, respiratory health and agricultural productivity across the island (Longo et al., 2010; Nelson and Sewake, 2008; Tam et al., 2016; Whitty et al., 2020).

The concentrations of S and chalcophiles in primary melts entering basaltic systems are predominantly controlled by the behaviour of sulfide during mantle melting (Ding and Dasgupta, 2018). During crystallization in crustal magma chambers, S contents may increase due to the fractionation of S-poor silicate phases, or become buffered by the stabilization of an immiscible sulfide phase (Smythe et al., 2017). Tracking the pre-eruptive evolution of S is non-trivial; erupted lavas have typically lost ∼90% of their original S (Métrich and Mandeville, 2010), and evidence for sulfide fractionation may be obscured by the resorption of sulfides during low pressure degassing (Edmonds and Mather, 2017; Moore et al., 1980). These problems are often circumvented by measuring S contents in melt inclusions (pockets of melt trapped within growing crystals that are less susceptible to degassing than erupted carrier liquids), or through measurements of refractory chalcophile element abundances in quenched matrix glasses (Jenner et al., 2010; Reekie et al., 2019). However, these archives can be degraded by petrological processes; the concentrations of chalcophile elements in melt inclusions may be altered by the secondary growth of sulfide phases post-entrapment (e.g., Hartley et al., 2017). Additionally, S concentrations in melt inclusions at Kīlauea are highly variable within a given sample, possibly due to the mixing of degassed and undegassed melts at depth (identified in submarine glasses by Dixon et al., 1991), or the entrapment of melt inclusions during late-stage degassing (Thornber et al., 2015).

The alternative approach, where the concentrations of refractory chalcophile elements in matrix glasses are used as a proxy for S, relies on the assumption that these elements are significantly less volatile than S, so are resistant to low pressure degassing. For example, Se has been used to reconstruct the pre-degassing behaviour of S in subaqueous lavas under the assumption that it behaves identically to S (as available thermodynamic data indicated that SeO_2 would not be stable in the gas phase; Jenner et al., 2010; Reekie et al., 2019). However, measurements of significant fluxes of Se within volcanic plumes emitted at Kīlauea and other basaltic volcanoes indicate that Se has volatile tendencies, at least in subaerial eruptions (Crowe et al., 1987; Edmonds et al., 2018; Mather et al., 2012). Furthermore, lavas from Antuco, Chile, have recently been shown to have S and Se contents which are

Please cite the published version in GCA: Wieser et al., 2020,
https://doi.org/10.1016/j.gca.2020.05.018

significantly lower than mid-oceanic ridge basalts (MOR**b)**, supporting the hypothesis that Se degasses at low pressures (Cox et al., 2019).

In this paper, we track the behaviour of S and other chalcophile elements (Cu, Zn, Mo, Cd, In, Sn, Sb, W, Tl, Bi, Se, As) from the Hawaiian mantle source to the volcanic vent using a suite of melt inclusions and matrix glasses from Kīlauea Volcano. Previous studies investigating sulfide saturation and chalcophile element behaviour at Kīlauea have been restricted to subaerial lavas which have fractionated beyond olivine control (<6–7 wt% MgO; e.g., those erupted during the 1955 and 1977 eruption; Desborough et al., 1968; Helz and Wright, 1992; Moore et al., 1980). There has been a particular focus in the literature on chalcophile element behaviour in lava lakes formed by the ponding, and subsequent fractionation, of degassed melt in pre-existing pit craters (Greaney et al., 2017; Skinner and Peck, 1969; Fleet and Stone, 1990). Until now, the most primitive glass composition at Kīlauea analysed for chalcophile elements had a MgO content of only 6.1 wt% (Fig. 1a; Greaney et al., 2017). In contrast, the spatter and scoria samples investigated in this study span a range of MgO contents (5.7–10.0 wt% MgO; Wieser et al., 2019), and were rapidly quenched following eruption, providing new insights into the behaviour of chalcophile elements during mantle melting and fractional crystallization at Kīlauea.

Ratios of chalcophile to lithophile elements in erupted melts (e.g., Pb/Ce, S/Dy, Sb/Pr) are frequently used to gain insight into various aspects of mantle evolution (Jochum and Hofmann, 1997; Hofmann, 1997; Kelley et al., 2013; Newsom et al., 1986; Saal et al., 2002). These studies generally assume that lithophile and chalcophile elements behave similarly during mantle melting, neglecting the complex changes in chalcophile element concentrations with increasing melt fraction that occur when residual sulfides are present in the mantle source. The fate of sulfides during mantle melting for mid-ocean ridge and ocean island basalts remains uncertain (Ding and Dasgupta, 2018). Variations in the concentrations of platinum group elements (PGEs) in lavas across the Hawaiian islands, along with elevated Cu/Pd ratios, have been attributed to variable abundances of residual sulfide in the Hawaiian mantle plume (Bennett et al., 2000). In contrast, Greaney et al. (2017) estimate the chalcophile element concentration of the Kīlauean mantle source from the batch melting equation under the assumption of sulfide-absent melting. As the bulk partition coefficients between the mantle residue and melt (bulk K_D) for chalcophile elements are substantially higher if sulfides are present in the mantle source, sulfide-free melting models will underestimate the concentrations of these elements in the mantle source if residual sulfides are in fact present. Clearly, the fate of mantle sulfides during melting must be critically evaluated before chalcophile element signatures can be used to assess the presence or absence of recycled materials in the Hawaiian mantle plume (e.g., Greaney et al., 2017).

The point at which sulfides saturate during fractional crystallization in Hawaiian melts is also debated (Greaney et al., 2017; Bennett et al., 2000; Desborough et al., 1968; Dixon

et al., 1997; Helz et al., 2017; Tatsumi et al., 1999; Wallace and Anderson, 1998). It has been demonstrated, using the chalcophile element systematics of mid-ocean ridges and oceanic plateaux, that a second stage of sulfide saturation often occurs following ascent of magmas from the mantle and fractional crystallization of these sulfide-undersaturated melts in the crust (Jenner, 2017; Reekie et al., 2019). This second stage of sulfide saturation is driven by an increase in S concentrations during fractional crystallization (as S is incompatible in most silicate minerals), along with a concurrent decrease in the sulfide (S^{2-}) solubility at sulfide saturation (SCSS), due to dropping temperature and changes in melt chemistry (Smythe et al., 2017). Specifically, the SCSS describes the amount of S^{2-} present in a silicate melt in equilibrium with a sulfide phase (O'Neill, 2020; hereafter $SCSS^{2-}$ for clarity). While PGE fractionation trends in Hawaiian lavas have been attributed to sulfide saturation (Tatsumi et al., 1999), recent Cu measurements in whole-rock and glasses from the Kīlauea Iki lava lake show that Cu behaves incompatibly until ∼2 wt% MgO, leading to suggestions that sulfides only saturate following extensive fractional crystallization (Greaney et al., 2017; Fig. 1a). Furthermore, although sulfides are present in eruption pumices and lake samples from Kīlauea Iki with MgO>2 wt%, the wide variability in bulk sulfide composition has been attributed to sulfide formation during late-stage processes such as quenching, rather than during primary sulfide-liquid immiscibility (Stone and Fleet, 1991). Our new data challenges this dominant view, and instead supports a model where almost all erupting melts at Kīlauea (<12 wt% MgO) were sulfide-saturated prior to the onset of S degassing at shallow pressures (c.f. Ding and Dasgupta, 2018; Skinner and Peck, 1969; Greaney et al., 2017; Helz et al., 2017; Pitcher et al., 2009).

Finally, we investigate the effects of syn-eruptive degassing and sulfide resorption on chalcophile element systematics by comparing the compositions of matrix glasses and melt inclusions at Kīlauea, and undegassed submarine glasses from Lōi'hi volcano. While there is growing evidence that Se degasses during subaerial eruptions (Cox et al., 2019; Mather et al., 2012), until now, Se analyses could only be conducted with laser ablation spot sizes greater than 100 μm (Jenner and O'Neill, 2012b). This prevented in-situ analyses of melt inclusions, making it difficult to pinpoint the timing of Se loss in relation to other volatile species (e.g., S). In this study, we utilize a novel method by which Se and As are measured in melt inclusions using a 50 μm diameter laser line scan (Supplementary Fig. A1). This analysis demonstrates that Se and S degas almost concurrently at Kīlauea. Overall, comparisons between matrix glass and melt inclusion compositions allow us to estimate the influence of sulfide saturation, and subsequent resorption on the sulfur outgassing budget of Kīlauean eruptions.

Please cite the published version in GCA: Wieser et al., 2020,
https://doi.org/10.1016/j.gca.2020.05.018

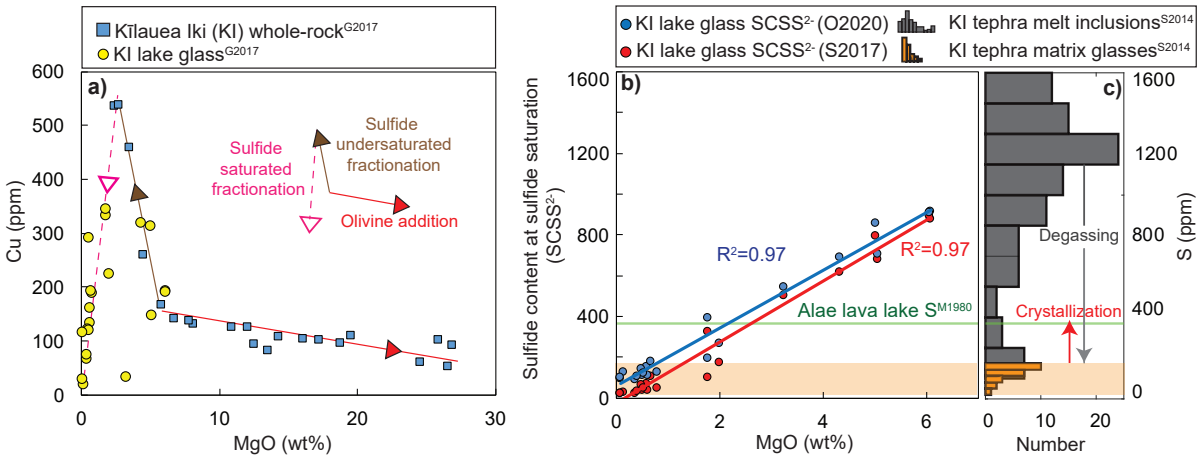

Figure 1: Chalcophile element behaviour in the Kīlauea Iki lava lake. **a)** Whole-rock Cu-MgO measurements from Kīlauea Iki (KI) define olivine-addition trends between 27 and 7 wt% MgO. Whole-rock and glass measurements show a rapid increase in Cu between 7 and 2 wt% MgO, followed by a rapid decrease at <2 wt% MgO (Greaney et al., 2017). The approximate vectors producing variability in Cu vs. MgO space are overlain. **b)** Calculated sulfide concentration at sulfide saturation ($SCSS^{2-}$) for the major element compositions of variably evolved glasses from the Kīlauea Iki lava lake (Greaney et al., 2017) using the Smythe et al. 2017 (S2017) and O'Neill, 2020 (O2020) (with Fe^{3+}/Fe_T=0.1). **c)** Degassing upon eruption causes melt S contents to drop from the high concentrations observed in Kīlauea Iki melt inclusions (PEC-corrected; grey histogram; Sides et al., 2014b) to the low concentrations observed in matrix glasses (Kīlauea Iki scoria; orange histogram and bar; Sides et al., 2014b). These degassed melts have significantly lower S contents than the $SCSS^{2-}$, so are sulfide undersaturated. Major element changes and a drop in temperature associated with extensive crystallization causes a decrease in the $SCSS^{2-}$. The lake became sulfide saturated when the $SCSS^{2-}$ dropped below the S content of the melt, which probably lay between the S content measured in Kīlauea Iki pumices (orange bar; Sides et al., 2014b) and that measured in a fractionated glass from Alae lava lake (green line; Moore et al., 1980).

2 Methods

2.1 Sample Details

Olivine-hosted melt inclusions and matrix glasses were analysed from rapidly-quenched spatter and tephra from four subaerial eruptions temporally associated with the East Rift Zone (ERZ) eruption at Mauna Ulu. Three eruptions occurred on Kīlauea's rift zones: (1) The highest fountaining phase of Mauna Ulu (Episode 12; December, 1969; ERZ, Swanson et al., 1979), (2) The Pauahi Crater eruption (November, 1973; ERZ), and (3) The Seismic South West Rift Zone (SSWRZ) fissure eruption of December, 1974 (Poland et al., 2014). The fourth eruption occurred within the summit caldera in August, 1971. To further constrain sulfide occurrence and chemistry at Kīlauea, scoria and lava samples from various locations across the Kīlauean edifice were examined (see Supplementary Fig. A2; Supplementary Table A1). To supplement this dataset from Kīlauea, 18 submarine glasses from Lōi'hi Volcano collected using submersibles at water depths of ~980–4700 m were analysed (Garcia et al., 1998; Garcia et al., 1993; Pietruszka et al., 2011).

2.2 Analytical Methodology

Glass chips were handpicked from jaw-crushed tephra and spatter samples and mounted in epoxy stubs. Melt inclusions were exposed by individually mounting picked olivine crystals on glass slides in Crystalbond^{TM} and grinding down to the level of melt inclusions with 250–1500 grade wet and dry paper. This method allowed embayments to be identified and discarded. Exposed melt inclusions were then mounted in epoxy and polished with progressively finer silicon pastes.

Major elements in Kīlauean melt inclusions, host olivines and matrix glasses were measured using the Cameca SX100 EPMA at the Department of Earth Sciences, University of Cambridge. Trace elements in Kīlauean matrix glasses and melt inclusions were analysed by laser ablation inductively coupled mass spectrometry (LA-ICP-MS/MS) at the School of Environment, Earth and Ecosystem Sciences at the Open University using a Photon Machines Analyte G2 193 nm excimer laser system coupled to an Agilent 8800 ICP-QQQ following the techniques described in Jenner et al. (2015) (additional details in Appendix a). Kīlauean matrix glasses were analysed with a spot size of 110 μm. Melt inclusions were analysed at varying spot sizes (65 μm, 50 μm, 40 μm and 25 μm) depending on the diameter of the inclusion. The surface of melt inclusions were pre-ablated (3 laser shots) prior to analysis. Analyses were performed manually to ensure that laser spots were placed such that they did not overlap with the host olivine, or vapour bubbles below the surface. Ni signals were monitored during each analysis and signals were carefully selected in Iolite software to only include the signal from the melt inclusion. Backgrounds were measured for 30 seconds prior to each analysis, followed by 20 seconds of signal and 50 seconds of washout. NIST-SRM 612 was used for external calibration and ^{43}Ca for internal calibration of trace element data. BCR-2G was used as the secondary standard to monitor precision and accuracy.

Major and lithophile element concentrations for the Kīlauean glasses and melt inclusions were reported in Wieser et al. (2019). Repeated analyses of secondary standards for these elements lie within ±5% of long-term (>2 years) Open University laboratory preferred values and preferred values for BCR-2G reported in Jenner and O'Neill (2012b). Repeated analyses of secondary standards for the chalcophile element concentrations reported in this study predominantly lie within ±5% for Ni, Cu, Zn, ±10% for Mo, Sb, W, As, and ±20–30% for Cd, In, Bi, Tl, Sn, Se of preferred values (see Appendix B for more detail). Variability in the latter elements may be attributed to standard heterogeneity and/or the low contents of these elements in standards (Jenner and Arevalo Jr, 2016). Precision (calculated from the standard deviation of 55 repeated standard analyses divided by the mean) was <5% for lithophile elements, and between 5 and 10% for most chalcophile elements (12% for Tl, 13% for Sn, 19% for Bi, 29 % for In, 44% for Cd). Lōi'hi matrix glasses were analysed by EPMA at the Smithsonian Institution (see Jenner et al. (2015) for description of analytical techniques). The composition of each glass was analysed three times, and

Please cite the published version in GCA: Wieser et al., 2020,
https://doi.org/10.1016/j.gca.2020.05.018

these measurements were averaged. SIMS and LA-ICP-MS analyses of the Lōi‘hi glasses were undertaken at the Carnegie Institution of Washington, and the Australian National University, respectively (Jenner et al., 2015), and the Open University (Se and As only).

Se and As are both affected by polyatomic and doubly charged interferences, and therefore require a different analytical protocol from the other trace elements. In Kīlauean and Lōi‘hi matrix glasses, Se and As were analysed using a spot size of 110 μm. Se and As in melt inclusions were measured using lines scans with a width of 50 μm. Line scans started and ended in the surrounding olivine, allowing careful selection of the signal from the melt inclusion in Iolite (Supplementary Fig. A1). Analyses were performed in oxygen mode using MS/MS mode, mass shifting $^{80}Se^{+}$ and $^{75}As^{+}$ to $^{96}SeO^{+}$ and $^{91}AsO^{+}$. This allowed effective elimination of all interferences, monitored by comparing analyses of in-house Se and As standards to preferred values (measured using isotope dilution ICP-MS). NIST SRM 612 was used for external calibration of data, with ^{29}Si used for internal calibration. NIST SRM 612 has considerably higher contents of some elements compared to volcanic materials (e.g., NIST SRM 612 has 15.2 ppm Se, Jenner et al., 2009). To avoid ‘phantom’ Se and other memory effects from analyses of these standards (Jenner and O’Neill, 2012b), repeat analyses of San Carlos olivine were undertaken prior to sample analyses. Accuracy was ±10% relative to in-house standards with Se and As concentrations close to those in our samples (see Jenner et al., 2015).

Sulfides were identified using an automated approach utilizing backscatter electron (BSE) and secondary electron (SE) imaging on a FEI Quanta 650FEG SEM at the University of Cambridge. BSE maps of epoxy mounts were collected with the brightness and contrast of the image adjusted such that only sulfides were visible. Concurrent collection of SE maps at normal brightness and contrast conditions allowed the position of sulfides within grains to be determined. While reflected light observations may bias observations towards larger sulfides, this method ensured that all sulfides greater than ∼1 μm (and some down to 0.5 μm) were identified. Bulk sulfide compositions were quantified by summing over energy dispersive x-ray spectroscopy (EDS) maps, as the fine scale exsolution features of many sulfides resulted in highly imprecise EPMA point analyses (even with a defocused beam). Quantification of EDS maps collected for secondary sulfide standards characterized by EPMA (pyrite, chalcopyrite and pentlandite) during each analytical session allowed assessment of the accuracy and the precision of this method. Precision for EDS quantification was <1%, and the accuracy relative to EPMA measurements of these standards was within ±5%. EDS results were corrected for consistent offsets from EPMA measurements by a factor of 0.96 for Fe, and 1.025 for Ni and Cu. Additional analytical details are provided in Appendix A.

Please cite the published version in GCA: Wieser et al., 2020,
https://doi.org/10.1016/j.gca.2020.05.018

3 Results

3.1 Glass and Melt Inclusion Chemistry

Matrix glasses from the three Kīlauean rift eruptions (Mauna Ulu, 1969, Pauhi Crater, 1973, and SSWRZ, 1974) are relatively primitive, with 7.4–10 wt% MgO (Fig. 2), and 10.2–11.2 wt% CaO (Supplementary Fig. A3). Their major element systematics, along with the absence of clinopyroxene and plagioclase crystals, indicate that these lavas experienced only olivine (+minor chrome-spinel) fractionation (Wright and Fiske, 1971; Supplementary Fig. A3). The high MgO contents of these glasses relative to the vast majority of subaerial Kīlauea deposits (Helz et al., 2014), combined with their simple fractionation trajectories, makes them suitable for assessment of the behaviour of chalcophile elements during mantle melting. Glasses from the 1971 summit eruption are more evolved than the three rift eruptions (5.7–6.6 wt% MgO, 10.7–11.1 wt% CaO; Fig. 2; Supplementary Fig. A3) and contain small crystals of clinopyroxene. Lōi‘hi glasses are variably evolved, with MgO contents between 5.1 and 7.9 wt% MgO (Fig. 2). Uncorrected Kīlauean melt inclusions have MgO contents which overlap with the MgO content of their co-erupted erupted matrix glasses (Fig. 2a; Wieser et al., 2019). The amount of post-entrapment crystallization calculated using the Petrolog3 Olivine MI tool (Danyushevsky and Plechov, 2011) at QFM assuming FeO*=11.33 wt% (for consistency with previous studies; Wieser et al., 2019; Sides et al., 2014b; Sides et al., 2014a) varies from -12 to 29%. Corrected melt inclusion MgO contents are between 6.9 and 13.3 wt% (Fig. 2b).

Please cite the published version in GCA: Wieser et al., 2020,
https://doi.org/10.1016/j.gca.2020.05.018

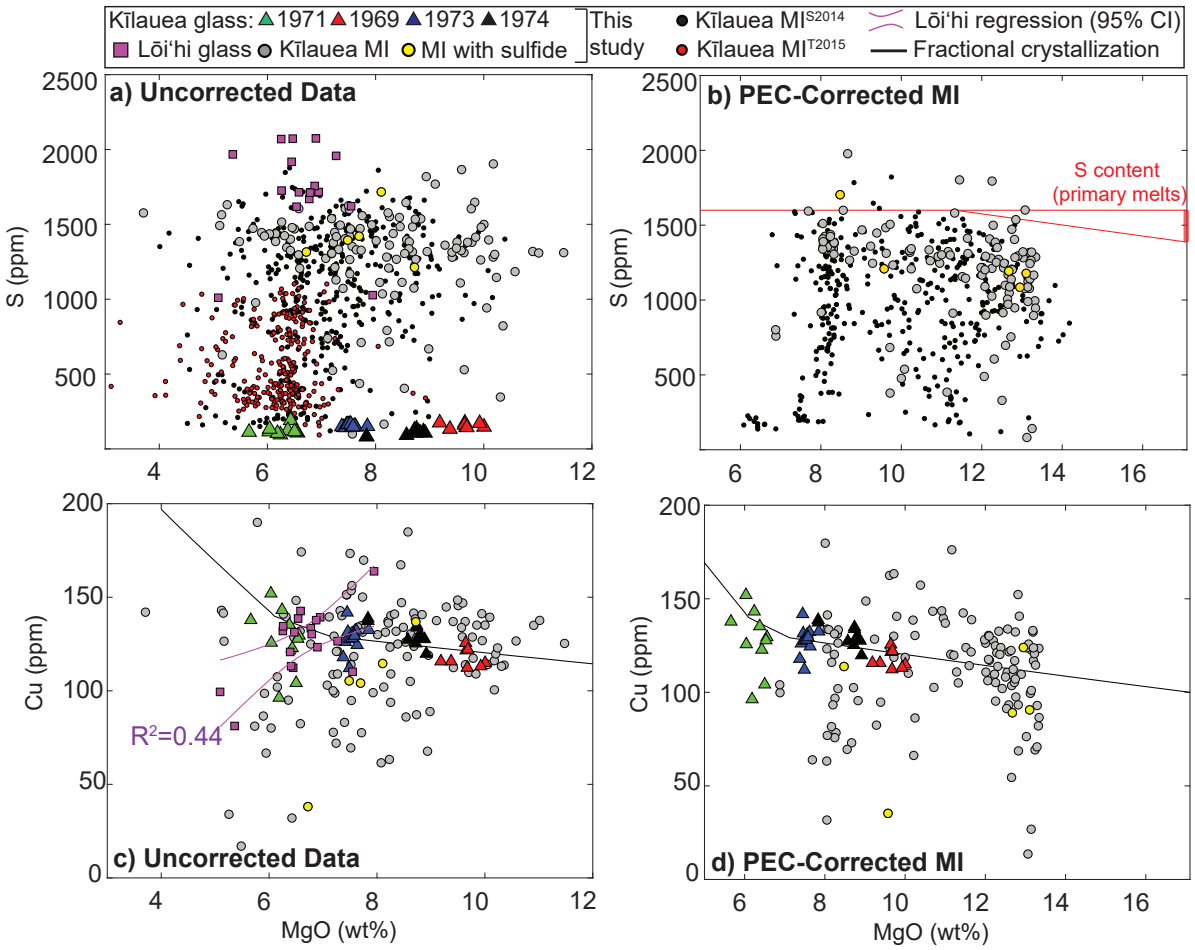

Figure 2: Cu, S and MgO systematics. **a)** S concentrations of Kīlauean melt inclusions, matrix glasses, and submarine matrix glasses from Lōi'hi. Literature melt inclusion data for Kīlauea from Sides et al. (2014b) and Sides et al. (2014a) (black dots) and Thornber et al. (2015) (red dots) are also show. Melt inclusions containing a sulfide (<0.1 vol%) are coloured yellow. **b)** Melt inclusion S and MgO systematics following a correction for post-entrapment crystallization (using the Olivine MI tool in Petrolog3). Estimated S concentrations of primary melts are shown with a vertical red line. The upper limit (1600 ppm) effectively brackets the vast majority of S-rich melt inclusions, while the lower limit (1387 ppm) was calculated by extrapolating back along olivine fractionation trends from 1600 ppm at 11.3 wt% MgO to ~17.1 wt% MgO (Clague et al., 1991) assuming S was entirely incompatible during olivine fractionation. **c)** Kīlauean matrix glasses show a slight increase in Cu contents with decreasing MgO, while Lōi'hi glasses show a decrease in Cu with decreasing MgO. Uncorrected melt inclusions with >10 wt% MgO plot alongside, and slightly above Kīlauean matrix glasses, while more evolved inclusions predominantly plot below matrix glasses. **d)** Following a correction for PEC ($K_{D,\ Cu}^{ol/melt} = 0.1$), melt inclusions form a cluster at ~13–14 wt% MgO, plotting on the fractionation trajectory defined by matrix glasses (black lines), although a number of inclusions lie significantly below this line. The fractional crystallization model for Cu was calculated from the Petrolog3 fractionation path buffered at QFM+0.3 described in the main text.

Uncorrected Kīlauean melt inclusion compositions from this study and the literature show variable S contents, from ∼100–1904 ppm (Fig. 2**a)**, while melt inclusion compositions corrected for post-entrapment crystallization (assuming S behaves incompatibly during crystallization of olivine) are between 82 and 1978 ppm (Fig. 2b). Kīlauean matrix glasses have substantially lower S contents (∼82–190 ppm) than melt inclusions, while submarine Lōi'hi matrix glasses have S contents which slightly exceed those in even the most S-rich Kīlauean melt inclusions (∼1010–2073 ppm; Fig. 2a). Melt inclusions with the highest S concentrations have Cl concentrations extending to higher values than erupted matrix glasses, although the correlation between Cl and S for the combined Kīlauean dataset is weak (R^2=0.14; Fig. 3a). In contrast, there is a strong correlation between S and Se (R^2=0.90; Fig. 3**b)**, and a moderate correlation between S and Bi (R^2=0.35; Fig. 3c). Lōi'hi glasses have similar Se, Bi, Cd and Cu concentrations to the most S-rich Kīlauean melt inclusions, but significantly higher Cl, and lower As concentrations (Fig. 3a, d).

Kīlauean matrix glasses show a slight increase in Cu with decreasing MgO (Fig. 2**c)**, consistent with literature observations of Cu systematics from the Kīlauea Iki lava lake (Greaney et al., 2017; Fig. 1a). In contrast, the more restricted sample set of Lōi'hi glasses shows a decrease in Cu with decreasing MgO (R^2=0.44; Fig. 2c; Supplementary Fig. A4). Uncorrected Kīlauean melt inclusions show Cu contents which overlap with and extend to significantly lower values than matrix glasses (Fig. 2c). Following a correction for post-entrapment crystallization (assuming $K_{D,\ Cu}^{ol/melt} = 0.1$; Greaney et al., 2017), approximately half of melt inclusions with high MgO contents (∼12–14 wt%) lie on the extension of the fractional crystallization trajectory defined by matrix glasses, while the other half plot to significantly lower Cu concentrations. The majority of inclusions with <10 wt % MgO have lower Cu contents than matrix glasses (Fig. 2d).

The trace element compositions of matrix glasses from the three rift eruptions which have not fractionated beyond olivine control (MgO>6.8 wt%; Wright and Fiske, 1971) were corrected for the effect of variable olivine fractionation by projecting back to 17.1 wt% MgO (Clague et al., 1991) using the reverse crystallization tool in Petrolog3. For simplicity, all elements except Cu ($K_{D,\ Cu}^{ol/melt} = 0.1$) were assumed to be entirely incompatible in olivine. Fractionation-corrected (F**c)** glass compositions exhibit strong positive correlations between highly incompatible lithophile elements (e.g., Ba vs. Ce, Ba vs. La; Fig 4a-b). In contrast, more compatible elements such as Yb, as well as Cu, Cd and Pb show weak, or even slightly negative correlations against Ba (Fig. 4c-f).

Please cite the published version in GCA: Wieser et al., 2020,
https://doi.org/10.1016/j.gca.2020.05.018

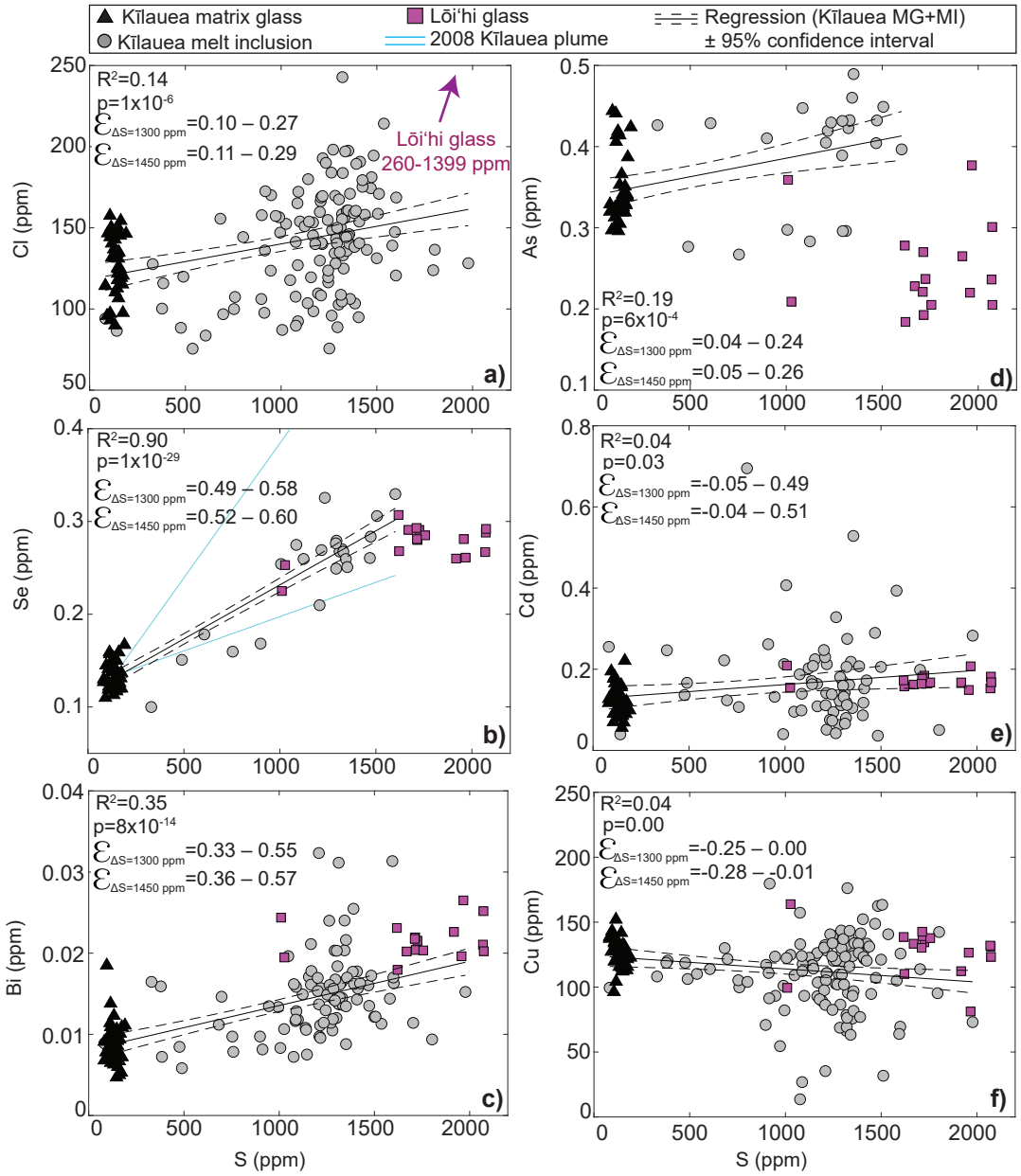

Figure 3: Assessing chalcophile element volatility. a-f) Plots of various chalcophile elements (and Cl) against S provide insights into elemental volatility. Linear regressions through the combined Kīlauea dataset (matrix glasses and melt inclusions from all 4 eruptions) are shown with 95% confidence intervals. The upper and lower limits of the initial and final concentrations of each element used to calculate emanation coefficients (ε) were estimated from the 95% confidence intervals of the regression lines for S_f=135, and S_i=1435 ppm and 1585 ppm (ΔS=1300 ppm and 1450 ppm respectively). Subaqueous Lōi'hi glasses have similar Se, Bi and Cd concentrations to those of the most S-rich Kīlauean melt inclusions, but lower As concentrations, and higher Cl concentrations. PEC-corrected concentrations are shown for melt inclusions, assuming that all elements except Cu ($K_{D,\ Cu}^{ol/melt} = 0.1$) are entirely incompatible in olivine. Note, that the y axis in **a)** has been cropped to emphasize the magnitude of Cl variation at Kīlauea, Lōi'hi glasses have Cl concentrations up to 1399 ppm. The range of S/Se ratios observed in the 2008 summit plume are shown in **b)** to demonstrate that the emanation coefficient of Se derived from petrological measurements is consistent with aerosol measurements (Mather et al., 2012). A full comparison of emanation coefficients calculated in this study and those of Mather et al. (2012) is shown in Fig. 13.

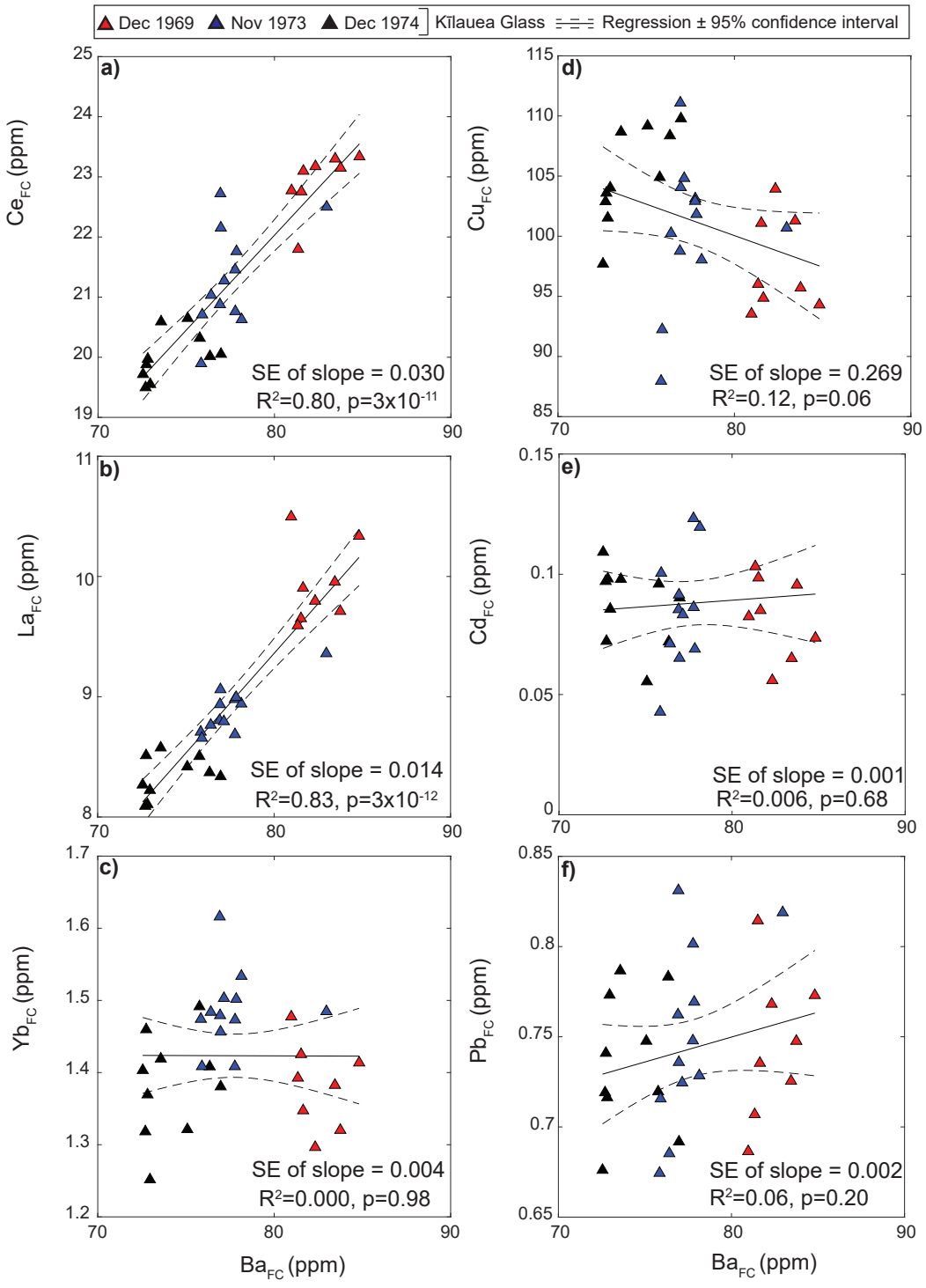

Figure 4: Fractionation-corrected trace element concentrations in matrix glasses from the three rift eruptions which have only fractionated olivine (+ minor chromite). . a-**b)** Ce and Le show strong positive correlations with Ba. c-f) In contrast, Yb, Cu, Cd and Pb show very weak correlations with Ba. Trace element contents were corrected for fractional crystallization (to 17.1 wt% MgO; Clague et al., 1991) assuming all elements except Cu ($K_{D,\ Cu}^{ol/melt} = 0.1$) were perfectly incompatible in olivine. The 95% confidence intervals on linear regressions through the data are shown, along with the standard error of the slope (and other statistical measures).

Please cite the published version in GCA: Wieser et al., 2020,
https://doi.org/10.1016/j.gca.2020.05.018

3.2 Sulfide Occurrence

Automated BSE-SE mapping identified sulfides in erupted products from seven different subaerial eruptions at Kīlauea (with glass MgO contents ranging from ∼6–10 wt%). Sulfides are relatively rare, but were observed in three textural contexts:

1. Included in olivine crystals (Fig. 5**a)**, often alongside spinels, and highly variable quantities of melt. Sulfide to melt volume proportions vary from >5% (Figs. 5f, g, h; Supplementary Fig. A5) to <0.2% (e.g., ∼0.04 vol% in Fig. 5e).
2. Within glassy, relatively open embayments with moderate to high S contents (Fig. 5c, d). In one instance, the sulfide is attached to the face of the olivine crystal (Fig. 5c).
3. In the walls of melt inclusion vapour bubbles and matrix glass vesicles (Fig. 5b; Supplementary Figs. A6–7).

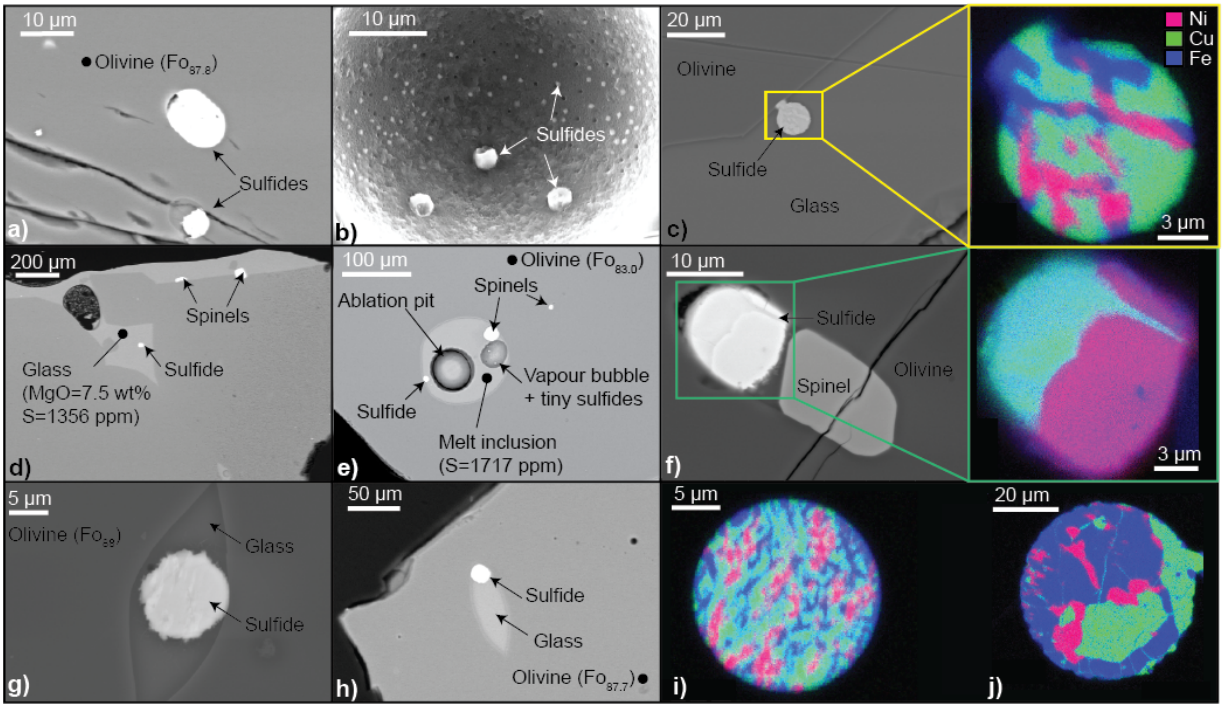

Figure 5: Textural and chemical characteristics of Kīlauean sulfides revealed with BSE and EDS mapping. **a)** Sulfides are hosted as inclusions within olivine crystals with high forsterite (Fo) contents. **b)** Sulfides with a bimodal size distribution within the wall of a melt inclusion vapour bubble. **c)** Sulfide attached to an olivine crystal within a relatively open embayment. EDS maps show that this sulfide consists of exsolved Fe, Ni and Cu-rich phases. **d)** Sulfide within an open, but undegassed embayment (S=1356 ppm). **e)** Sulfide within a melt inclusion, which also contains a vapour bubble with tiny <1 µm sulfides embedded in the bubble wall. **f)** Sulfide trapped within an olivine crystal alongside a spinel, and a small amount of melt. EDS maps show that this sulfide has exsolved 2 main phases at a relatively course scale. **g-h)** Sulfides trapped along with small pockets of melt within olivine crystals. **i-j)** EDS maps of sulfides showing fine and coarse exsolution of Cu-Ni-Fe rich phases (BSE images not shown).

Sulfides are roughly spherical to ellipsoidal, with diameters between 3 and 30 μm, except for sulfides in the walls of matrix glass vesicles and melt inclusion vapour bubbles, which have diameters of ∼0.5–3.0 μm (Fig. 5b). EDS mapping reveals that sulfides consist of exsolved Cu- and Ni-rich phases, often with a separate Fe-rich phase (Fig. 5c, f, i, j). These textures likely result from the exsolution of monosulfide-intermediate solid solution (MSS-ISS) phases from an immiscible sulfide liquid (Czamanske and Moore, 1977; Patten et al., 2012). These findings build on literature reports; sulfide inclusions have been noted in primitive olivines erupted in Kīlauea Iki pumices ($Fo_{88.5}$; Helz, 1987), and within silicate phases and matrix glass from the 1955 and 1977 eruptions of Kīlauea (Desborough et al., 1968; Helz and Wright, 1992; Moore et al., 1980). Interestingly, only three sulfides were found in Kīlauean matrix glasses in comparison to the 14 sulfides found when mapping a roughly equivalent area of olivine crystals. Sulfides within matrix glasses have complex external morphologies (Fig. 6; Supplementary Fig. A8) compared with the smooth, spherical morphology of sulfides hosted within olivine crystals, embayments, and melt inclusions (Fig. 5). EDS mapping reveals that sulfides with these complex morphologies are predominantly composed of Fe and O, with only small quantities of Cu, Ni and S-rich material (∼1 μm; Fig. 6; Supplementary Fig. A8). In contrast, spherical sulfides are O-poor (Supplementary Fig. A9). Approximately spherical, O-poor sulfides with comparable exsolution textures to those found within Kīlauean olivines and melt inclusions are relatively abundant within Lōi‘hi matrix glasses. No texturally complex, O-rich sulfides were observed in Lōi‘hi glasses.

Please cite the published version in GCA: Wieser et al., 2020,
https://doi.org/10.1016/j.gca.2020.05.018

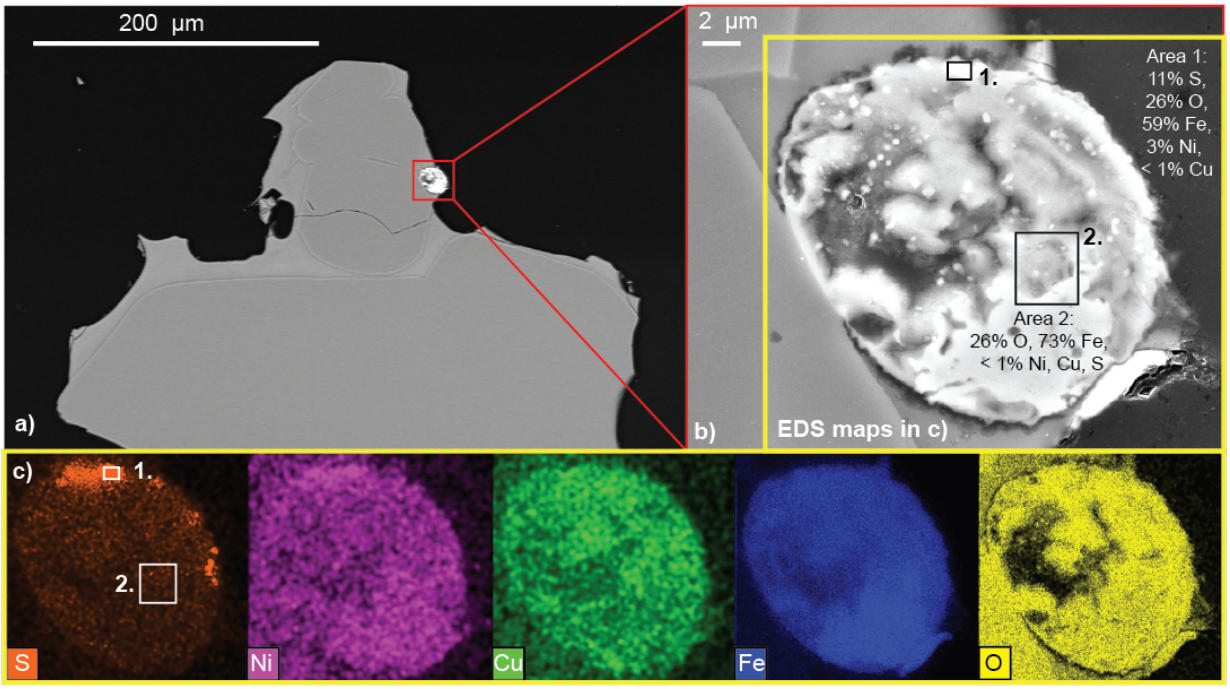

Figure 6: Textural and chemical characteristics of resorbed Kīlauean sulfides **a)** A BSE image of a resorbed sulfide attached to an olivine crystal. **b)** BSE image of the sulfide (red square in **a)**, which shows considerable textural complexity compared to the pristine sulfides shown in Fig. 5. **c)** EDS maps of the area indicated by the yellow rectangle in b). Most of the resorbed sulfide is very Ni, S and Cu poor, with counts only just above background (e.g., compare area 2 with Fig. 5 **c, f, i, j**). Small regions of more S (and Ni)-rich material survive (e.g. area 1). The areas indicated with black rectangles were quantified in Esprit2.1 to give an approximate indication of their composition in wt%. Resorbed sulfides contain considerable quantities of O (∼26 wt%), compared to pristine sulfides which generally contain <4 wt% O (Supplementary Fig. A9).

4 Discussion

4.1 Sulfides in Kilauea's Mantle Source

The fate of sulfides during mantle melting can be assessed by comparing the S concentrations of primary Kīlauean melts to models of the sulfide content at sulfide saturation ($SCSS^{2-}$). If residual sulfides are present during mantle melting, the concentration of S^{2-} in the melt in equilibrium with this mantle is equal to the $SCSS^{2-}$; once sulfides are exhausted, the S^{2-} concentration in melts drops to significantly lower values than the $SCSS^{2-}$ (Ding and Dasgupta, 2018). Thus, if residual sulfides are present throughout the melting interval, the calculated $SCSS^{2-}$ should be approximately equal to the S^{2-} concentrations in primary Kīlauean melts. In contrast, if the mantle has exhausted sulfide, primary melts should have significantly lower S^{2-} concentrations than the $SCSS^{2-}$.

The S content of primary melts at Kīlauea was estimated from PEC-corrected S contents in melt inclusions (this study and Sides et al. (2014b) and Sides et al. (2014a). The upper limit was set at 1600 ppm, based on the approximately constant upper limit of S in

PEC-corrected melt inclusion data (ignoring a small number of inclusions with significantly higher S; horizontal red line; Fig. 2b). As S behaves incompatibly during olivine-only fractionation, a minimum value for the primary S concentration of 1387 ppm was calculated by back-projecting the 1600 ppm observed at ∼11.3 wt% MgO to 17.1 wt% MgO (a reasonable upper limit of the MgO content for Kīlauean primary melts; Clague et al., 1991) assuming S is entirely incompatible in olivine (downward sloping red line; Fig. 2b).

For a given pressure, temperature, and melt composition, there are a variety of models which calculate the $SCSS^{2-}$ (e.g., Fortin et al., 2015; Li and Ripley, 2009; Li and Ripley, 2005; Smythe et al., 2017; O'Neill, 2020). However, most experiments used to calibrate $SCSS^{2-}$ models have been performed on FeS liquids, despite the fact that sulfides in basaltic lavas and mantle peridotites contain substantial quantities of Ni and Cu (Kiseeva et al., 2017; Patten et al., 2013; Smythe et al., 2017; Figs. 5c, f, i, j). The $SCSS^{2-}$ decreases as the ratio of Fe/(Fe+Ni+Cu) in the sulfide decreases, so $SCSS^{2-}$ models based on experiments with FeS sulfides will overestimate the predicted $SCSS^{2-}$ (Smythe et al., 2017). To account for this, only the two most recent $SCSS^{2-}$ models that include a correction for the Ni and Cu contents of sulfides were used (Smythe et al., 2017; O'Neill, 2020).

The $SCSS^{2-}$ along PT paths for a peridotitic mantle undergoing melting ascending from its solidus to the base of the lithosphere beneath the island of Hawaii were calculated for three different potential temperatures (1450°C, 1550°C, 1650°C; Fig. 7a). PT paths were calculated using Melt-PX (Lambart et al., 2016). The pressure at which melting terminated was calculated using estimated lithospheric thicknesses of 90–110 km (Li et al., 2004; Wölbern et al., 2006), assuming 15 km of crust with the density-depth profile of Putirka (2017), and a mantle with =3300 kgm^{-3}. For simplicity, and due to a lack of experimental data to reliably parameterize major element changes during melting at >3 GPa (Ghiorso et al., 2002), a constant primary melt composition was used for all points along the PT array in $SCSS^{2-}$ models. The primary melt composition was taken from Clague et al. (1991), reducing FeO_T by 3.2% to better fit the liquid line of descent for Kīlauea for the glasses measured in this study (Supplementary Fig. A3). The initial Cu and Ni contents of primary melts were set at Cu_i=100 ppm and Ni_i=900 ppm respectively, and the ratio of Fe^{3+}/Fe_T was set at 0.1 (Fig. 8a).

The $SCSS^{2-}$ models of O'Neill (2020) and Smythe et al. (2017) (hereafter O2020 and S2017 for brevity) calculate the composition of the co-existing sulfide. However, in both models (but particularly in the S2017 model), calculated sulfide compositions are more Ni-rich and Fe-poor than the vast majority of literature measurements of sulfide compositions within mantle peridotites and pyroxenites (Fig. 7b, see also Fig. 11 of O'Neill, 2020). Consequently, due to the strong influence of the sulfide Fe/(Fe+Cu+Ni) ratio on the $SCSS^{2-}$, model trajectories lie significantly below the range of S contents in primary melts at all pressures (Fig. 7c). Interestingly, the S2017 model shows a decrease in the $SCSS^{2-}$ with decreasing

Please cite the published version in GCA: Wieser et al., 2020,
https://doi.org/10.1016/j.gca.2020.05.018

pressure due to changes in the sulfide composition, which is the opposite trajectory to that expected from the strong pressure dependency on the $SCSS^{2-}$. The unusual behaviour of the S2017 model, as well as the underprediction of sulfide Fe/(Fe+Cu+Ni) ratios in both models, likely reflects the fact that the parametrizations for sulfide compositions are not suitable for use at the high pressures and temperatures relevant to mantle melting beneath Hawaii. For example, in the S2017 model, sulfide compositions are calculated using the sulfide-silicate partitioning behaviour determined by Kiseeva and Wood (2015) at 1.5 GPa. In the O2020 model, parameterizations for sulfide compositions were obtained by tuning the model to minimise the least squares difference between observed S contents and the SCSS in a dataset of ocean floor glasses (Jenner and O'Neill, 2012a). Due to the absence of constraints on the controls on sulfide compositions at pressures and temperatures relevant to mantle melting beneath Hawai'i, we favour $SCSS^{2-}$ models where the sulfide composition was fixed at 5 wt% Cu, 20 wt% Ni, 33 wt% S, 42 wt% Fe (Ding and Dasgupta, 2018; yellow square; Fig. 7b).

When the sulfide composition is fixed in the S2017 model (solid lines), only melts produced right at the base of the lithosphere (beige bar; Li et al., 2004; Wölbern et al., 2006) for the hottest potential temperatures (T_p=1650°C have $SCSS^{2-}$ values comparable to the S contents of primary melts (red bar; Fig. 7d). In contrast, when the sulfide composition is fixed in the O2020 model, the $SCSS^{2-}$ model trajectories (dashed lines, Fig. 7d) largely lie within the field defined by the S contents of primary melts. For a fixed sulfide composition, the differences between the O2020 and S2017 $SCSS^{2-}$ models largely result from their different sensitivities to the Fe^{3+}/Fe_Tratio (which primarily affects the $SCSS^{2-}$ through a decrease in $X_{FeO}^{Silmelt}$; O'Neill, 2020). An increase in Fe^{3+}/Fe_T from 0 to 0.2 causes the $SCSS^{2-}$ to increase by only 7% in the S2017 model, but 23% in the O2020 model. Given that both models were calibrated on a dataset of reduced melts, it is difficult to critically evaluate these different model sensitivities. However, the fact that both models show $SCSS^{2-}$ values that are less than, or equal to the S contents of primitive Kīlauean magmas demonstrates that the mantle source must remain sulfide saturated throughout the melting interval. If sulfides were exhausted during melting, the S contents of melt inclusions would be lower than modelled $SCSS^{2-}$ values.

Interestingly, the S2017 model trajectories indicate that mantle melts cannot dissolve enough S^{2-} to account for the high S contents observed in primitive melt inclusions, even if the mantle is sulfide saturated (Fig. 2, Fig. 7). This discrepancy may reflect the elevated oxidation state of Hawaiian melts relative to MORB (Brounce et al., 2017; Moussallam et al., 2019; Moussallam et al., 2016; Cottrell and Kelley, 2011; Berry et al., 2018; red bars, Fig. 8a). The speciation of S in basaltic melts undergoes an abrupt transition from S^{2-} and S^{6+} with increasing fO_2 between QFM and QFM+2 (Jugo et al., 2010). S^{6+} species are an order of magnitude more soluble than S^{2-} species in basaltic melts, only forming a separate sulfate phase such as anhydrite at very high melt S contents (∼1.5 wt%, Jugo

et al., 2005). Thus, in relatively S-poor melts such as those at Kīlauea (∼1600 ppm), the exponential increase in S^{6+} species with increasing fO_2 drives an exponential increase in the total solubility of S (Jugo et al., 2010). As models of sulfide solubility (e.g., S2017, O2020) only account for S^{2-} species, if S^{6+} species are present, a correction must be applied to $SCSS^{2-}$ model outputs to calculate the total solubility of S (hereafter $SCSS_{Tot}$):

$$SCSS_{Tot} = \frac{SCSS^{2-}}{1 - \frac{S^{6+}}{\Sigma S}} \tag{1.1}$$

For example, if the $SCSS^{2-}$ = 1300 ppm, and Kīlauean melts contained 10% S^{6+}, the $SCSS_{Tot}$ would equal 1444 ppm. Thus, the presence of even a relatively small proportion of S^{6+} species in mantle melts could account for the fact that primary Kīlauean melts have S contents exceeding the solubility limit for S^{2-} species in the S2017 model at pressures and temperatures relevant to melt generation in the mantle.

To our knowledge, there are no published measurements of S speciation from shield-stage tholeiitic lavas at Kīlauea. Early submarine alkalic lavas have S^{6+}/S_T ratios of 0.09–0.24 (determined by X-ray absorption near-edge structure- XANES; Jugo et al., 2010), although these lavas may be more oxidised than shield stage lavas (Sisson, 2003). Further constraints can be derived from other Hawaiian volcanoes: XANES measurements of submarine basalts from Mauna Kea and Lōi‘hi show S^{6+}/S_T ratios up to ∼0.08 (Brounce et al., 2017) and 0.31 respectively (Jugo et al., 2010). However, there is a lack of consistency between different studies; S^{6+}/S_T ratios in a set of Lōi‘hi glasses have been estimated using SKα peak shifts by Wallace and Carmichael (1994) (green circles) and XANES by Jugo et al. (2010) (magenta circles). The sample with the highest S^{6+}/S_T ratio measured using SKα peak shifts has the lowest S^{6+}/S_T ratio measured by XANES, while the samples with the lowest S^{6+}/S_T ratios measured by SKα peak shifts have the highest S^{6+}/S_T ratios measured by XANES (Fig. 8b). These discrepancies may reflect differences between SKα peak shift and XANES measurements, or the effects of beam damage (Smythe et al., 2017), but are concerning nonetheless.

An alternative approach to estimate the proportion of S^{6+} species utilizes the strong coupling of Fe and S redox states. Jugo et al. (2010) performed experiments on predominantly hydrous basaltic and andesitic melts at 1050°C, 200 MPa, yielding the following relationship:

$$\frac{S^{6+}}{S_T} = \frac{1}{1 + 10^{(2.1 - 2\Delta QFM)}} \tag{1.2}$$

Nash et al. (2019) performed experiments on basaltic-dacitic compositions at 1300°C, and 1 atmosphere. They attribute differences in the observed transition of S redox relative to Fe redox between their study and that of Jugo et al. (2010) to a strong temperature dependence, which is incorporated in their parameterization with T in K:

Please cite the published version in GCA: Wieser et al., 2020,
https://doi.org/10.1016/j.gca.2020.05.018

$$\log\frac{S^{6+}}{S^{2-}} = 8\log\frac{Fe^{3+}}{Fe^{2+}} + \frac{8.7436 \times 10^6}{T^2} - \frac{27703}{T} + 20.273 \quad (1.3)$$

However, while the differences in pressure between these two studies (0.1 vs. 200 MP**a)** are likely negligible (Nash et al., 2019), the speciation transition has been shown to shift by ∼1.5 log units of fO_2 between 0.5 and 1.5 GPa (Matjuschkin et al., 2016). Unfortunately, as experiments investigating the competing effects of pressure and temperature at conditions relevant to mantle melting beneath the thick Hawaiian lithosphere have not been performed, it would be unwise to apply existing low-pressure experimental parametrizations to estimate the S redox state of primary melts. In summary, $SCSS^{2-}$ models provide strong evidence that the Kīlauean mantle source must remain sulfide saturated throughout the melting interval to account for the high S contents of primitive melt inclusions. To resolve discrepancies between the S2017 and O2020 models, and assess whether primary melts contain S^{6+} species, significantly more experimental work is required to: 1) evaluate the differential sensitivities of the S2017 and O2020 models to the Fe^{3+}/Fe_T ratio, 2) accurately predict mantle sulfide compositions from silicate melt compositions at high pressures and temperatures, and 3) investigate the position of the speciation transition from S^{2-} to S^{6+} at high pressures and temperatures.

Please cite the published version in GCA: Wieser et al., 2020,
https://doi.org/10.1016/j.gca.2020.05.018

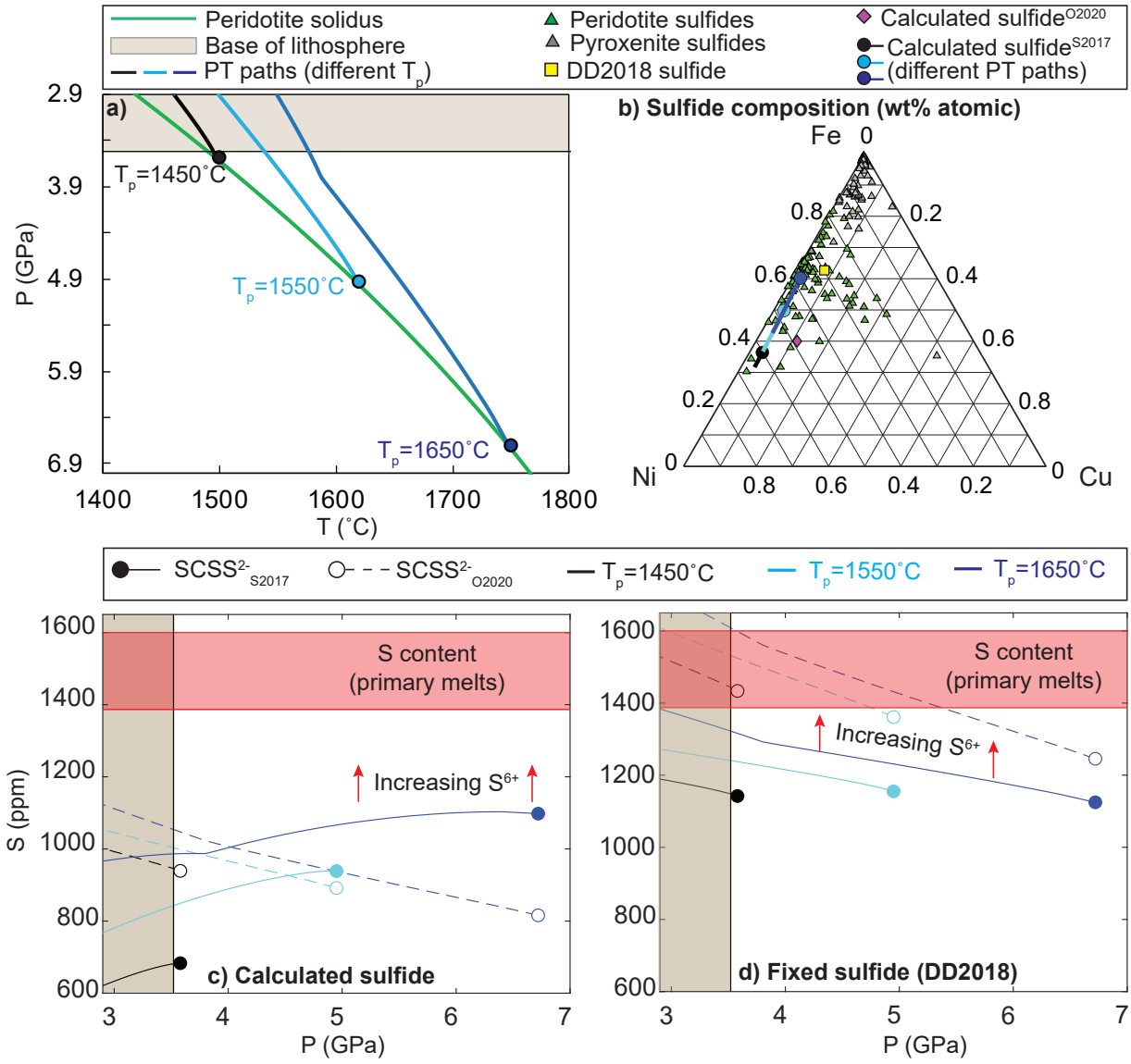

Figure 7: Modelling the $SCSS^{2-}$ at PT conditions relevant to mantle melting beneath Hawai'i. **a)** PT paths for an ascending peridotitic mantle undergoing melting for three different potential temperatures (calculated in Melt-PX; Lambart et al., 2016). **b)** Comparison of calculated sulfide compositions from $SCSS^{2-}$ models with measured sulfide compositions in mantle peridotites and eclogites/pyroxenites (Bulanova et al., 1996; Guo et al., 1999; Pearson et al., 1998; Richardson et al., 2001; Westerlund et al., 2006). The sulfide composition in the S2017 model changes along the PT path and deviates from measured sulfide compositions, particularly near the top of the melting column. The calculated sulfide composition from the O2020 model (magenta diamond; which does not change along the PT path) also plots away from the composition of most mantle sulfides. The fixed sulfide composition used in the models shown in **d)** is marked with a yellow square (after Ding and Dasgupta, 2018). **c)** Calculated $SCSS^{2-}$ trajectories following the PT paths in **a)** using calculated sulfide compositions. The decrease in the $SCSS^{2-}$ in the S2017 model with decreasing pressure is an artefact of the change in the composition of the sulfide. As both models predict Fe-poor sulfides compared to measured mantle sulfides, the $SCSS^{2-}$ in both models are anomalously low. **d)** Calculated $SCSS^{2-}$ trajectories using a fixed sulfide composition (yellow square in **b)**). Except for melts generated right at the base of the lithosphere from a mantle with T_p=1650°C, model trajectories in the S2017 model plot below the estimated S contents of primary Kīlauean melts. In contrast, the O2020 model predicts $SCSS^{2-}$ values within the range of primary Kīlauean melts. These model differences reflect the increased sensitivity of the O2020 model to Fe^{3+}/Fe_T (set at 0.1 here, Fig. 8a).

Please cite the published version in GCA: Wieser et al., 2020,
https://doi.org/10.1016/j.gca.2020.05.018

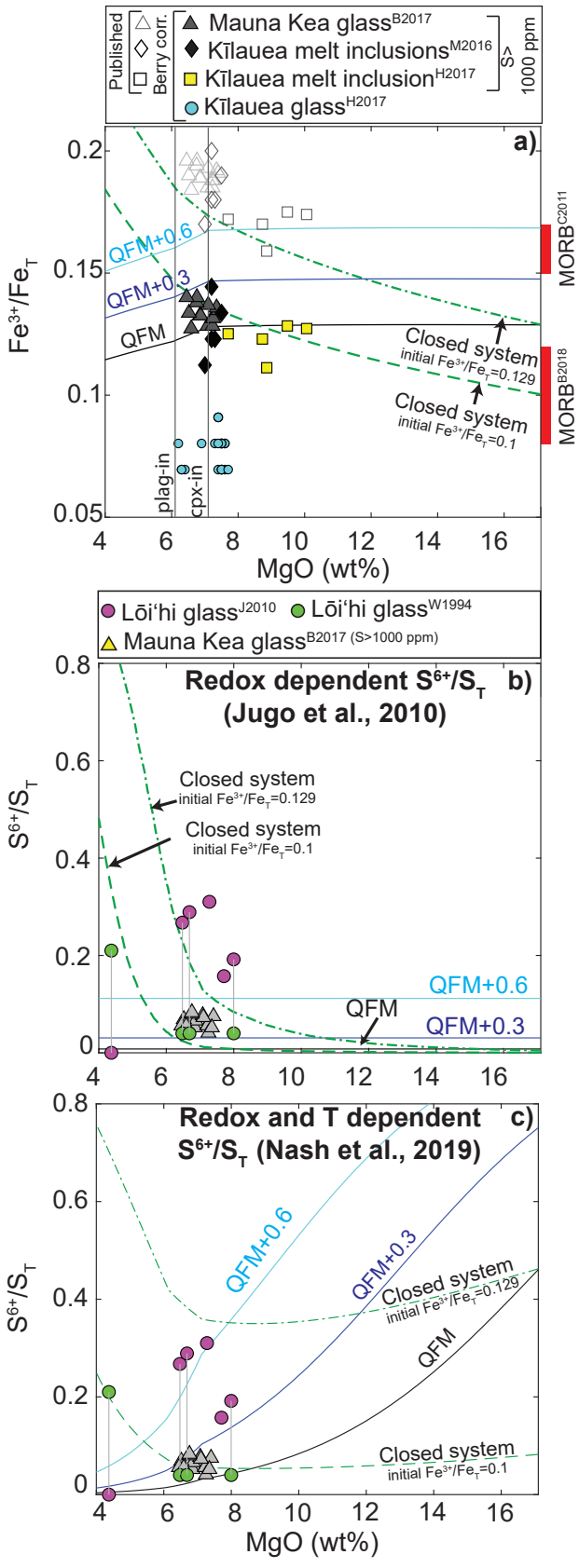

Figure 8: Models and observations of S and Fe redox in Hawaiian melts. **a)** Literature measurements of Fe^{3+}/Fe_T in Kīlauean melt inclusions (Moussallam et al., 2016; Helz et al., 2017) and Mauna Kea glasses (Brounce et al., 2017) with S>1000 ppm. Recent debates regarding the interpretation of Mossbauer spectra used for XANES calibration has led to suggestions that a correction must be applied to literature data. Published ratios are shown as hollow symbols, while ratios corrected using the equation of Berry et al. (2018) are shown as filled symbols. Prior to applying this correction, +0.01 was added to the data of Helz et al. (2017) to account for their slight adjustment to the calibration of Cottrell et al. (2009). Values corrected using the Zhang et al. (2018) method would lie in between published and Berry-corrected data. Trajectories from Petrolog3 models are overlain, as well as estimates of the oxidation state of MORB (Berry et al., 2018; Cottrell and Kelley, 2011). b-**c)** Available literature data for S redox from Lōi'hi (Wallace and Carmichael, 1994) and Mauna Kea (Brounce et al., 2017). The fractionation trajectories shown in **a)** were used to calculate the S^{6+}/S_T using the model of Jugo et al. (2010) in part **b)**, and Nash et al. (2019) in part c).

A complementary approach to quantify the longevity of residual sulfide in the Kīlauean mantle source utilizes the differential behaviour of lithophile and chalcophile elements during mantle melting. Lavas erupted at Kīlauea volcano show cyclic variations in trace element and isotope ratios (e.g., Nb/Y, $^{206}Pb/^{204}Pb$; Pietruszka and Garcia, 1999; Sides et al., 2014b), attributed to variations in melt extent and mantle source heterogeneity (Hofmann et al., 1984; Pietruszka et al., 2018). The suite of eruptions investigated in this study (1969–1974) incorporate some of the most rapid changes in lava chemistry over the past few hundred years (Pietruszka and Garcia, 1999; Wieser et al., 2019), and show chemical variations consistent with changes in extent of melting (Hofmann et al., 1984). Thus, they provide the ideal opportunity to evaluate the longevity of sulfides in the Hawaiian mantle source.

The concentration of chalcophile elements in mantle melts is controlled by the initial concentration in the mantle source (C_i), the melt extent (F), and the bulk partition coefficient between the silicate melt and the mantle residue (which may contain silicate and sulfide phases). The concentrations of two elements with low bulk K_Ds in suites of lavas spanning a range of melt extents are well-correlated (e.g., Ba vs. Ce and La; Fig. 4a-b; Hofmann et al., 1984). In contrast, if one element has a high K_D in a residual phase (e.g., Yb in garnet), giving it a bulk K_D close to 1, its concentration will be buffered across a wide range of melt extents. The gradient of a linear regression between this element and a highly incompatible element such as Ba will be ∼0 (e.g., Fig. 4c; Hofmann et al., 1984). In the past, such comparisons have been used to demonstrate that residual garnet is present throughout the melting interval at Kīlauea (Hofmann et al., 1984). Like Yb, many chalcophile elements show poor correlations with Ba (e.g. Cu, Cd, Pb; Fig. 4d-f). This implies that chalcophile element concentrations are buffered by the presence of a residual phase during melting in which these elements have a high K_D. Residual sulfide is the most likely candidate, as chalcophile elements have very high K_Ds in sulfides (e.g., $K_{D,\,Cu}^{sulf/melt}$ = 61–729 and $K_{D,\,Pb}^{sulf/melt}$ =7–145 for a wide range of melt FeO contents; Kiseeva and Wood, 2015; $K_{D,\,Cu}^{sulf/melt}$ = 800–4600 and $K_{D,\,Pb}^{sulf/melt}$ =24–170 in basaltic-rhyolitic melts; Li and Audétat, 2015), but low K_Ds in silicates (Lee et al., 2012; Liu et al., 2014). However, it is also worth noting that while $K_{D,\,Cd}^{sulf/melt}$= 12-201 (Kiseeva and Wood, 2015), previous studies have demonstrated that the major host for Cd in the mantle is likely clinopyroxene (Witt-Eickschen et al., 2009).

To demonstrate the variable response of chalcophile and lithophile elements during mantle melting, we model the behaviour of Cu and Ba in aggregated batch melts (after Lee et al., 2012) calculated at very small ΔF values (ΔF=0.0001; see Appendix A for details). For simplicity, it was assumed that all the S in the mantle was held within sulfides and the concentration of S in mantle melts produced while sulfides were present in the residue was 1600 ppm (Fig. 2b). The amount of residual sulfide present at each step was calculated assuming that mantle sulfides contain 33 wt% S. The concentration of Ba and Cu in the mantle prior to the onset of melting were set at 6.85 and 20 ppm respectively

Please cite the published version in GCA: Wieser et al., 2020,
https://doi.org/10.1016/j.gca.2020.05.018

(Palme and O'Neill, 2014). The partition coefficient of Cu in sulfide varies as a function of temperature and sulfide composition (Kiseeva and Wood, 2015). Assuming a sulfide composition of 20% Ni, 5% Cu (Fig. 7b; Ding and Dasgupta, 2018) and a liquid FeO content of 11.33 wt% (Supplementary Figure A3), $K_{D,\,Cu}^{sulf/melt}$ varies from ∼250 to ∼150 for T=1500 and 1700°C respectively (Fig. 7a; Kiseeva and Wood, 2015). However, previous studies modelling Cu during mantle melting have used values of $K_{D,\,Cu}^{sulf/melt}$ as high as 800 (Lee et al., 2012). To reflect the uncertainty in this parameter, models were run for $K_{D,\,Cu}^{sulf/melt}$ = 200 and 800. Model melt compositions were compared to fractionation-corrected glass compositions from the three rift eruptions of this study which have only fractionated olivine (and minor chrome-spinel; MgO >6.8 wt%, Wright and Fiske, 1971).

At the onset of melting, the presence of residual sulfide in the mantle raises the bulk K_D for Cu, causing aggregated melts to have significantly lower Cu concentrations than melts produced in a sulfide-free mantle (magenta vs. green lines; Fig. 9a-d). The concentration of Cu in the first melts produced at the onset of melting decreases with increasing initial mantle S contents, as the higher the proportion of sulfide, the higher the bulk K_D, Cu. Rapid changes in Ba (which is highly incompatible) combined with the buffering of Cu by residual sulfide (Fig. 9a-d) results in the gradient of Cu vs. Ba being close to zero (Fig. 9c-f). The production of S-rich melts results in the amount of sulfide in the mantle source declining throughout the melting interval. This drives rapid changes in the bulk K_D of Cu until the point at which sulfide is exhausted (black star), after which Cu acts incompatibly (bulk K_D=0.046). For $K_{D,\,Cu}^{sulf/melt}$=800, Cu concentrations in aggregated melts peak slightly after the exhaustion of sulfides (Fig. 9b, d; Lee et al., 2012). For $K_{D,\,Cu}^{sulf/melt}$=200, Cu concentrations in aggregated melt remains approximately constant until sulfides are exhausted (black star, Fig. 9a, c). In both models, as the point of sulfide exhaustion is approached, there is a rapid change in the trajectory of the gradient vs. Ba. For $K_{D,\,Cu}^{sulf/melt}$ =200, the gradient becomes strongly positive after sulfides are exhausted. For $K_{D,\,Cu}^{sulf/melt}$=800, the gradient starts increasing (Fig. 9f) once sulfides are exhausted, with a delay before the gradient becomes positive (aligning with the prominent peak in Cu vs. F and Cu vs. Ba space; Fig. 9b, d). In both models, after the exhaustion of sulfides, melt Cu concentrations gradually approach the compositions of melts produced from a mantle which was sulfide free from the onset of melting (green lines), and the gradients become strongly positive (Fig. 9e-f).

The concentration of Cu and the gradient of Cu vs. Ba in fractionation-corrected matrix glasses analysed in this study, along with prior constraints on the extent of mantle melting at Kīlauea, provide insight into the fate of mantle sulfides. Previous studies of trace element abundances in Kīlauean samples have suggested that the mantle source undergoes 5–10% melting (grey box; Fig. 9a-b; Bennett et al., 2000; Norman et al., 2002). The range of Ba concentrations observed in the glasses investigated in this study are consistent with melt extents between F=0.08 and 0.095 (Supplementary Fig. A11). In models where sulfides are

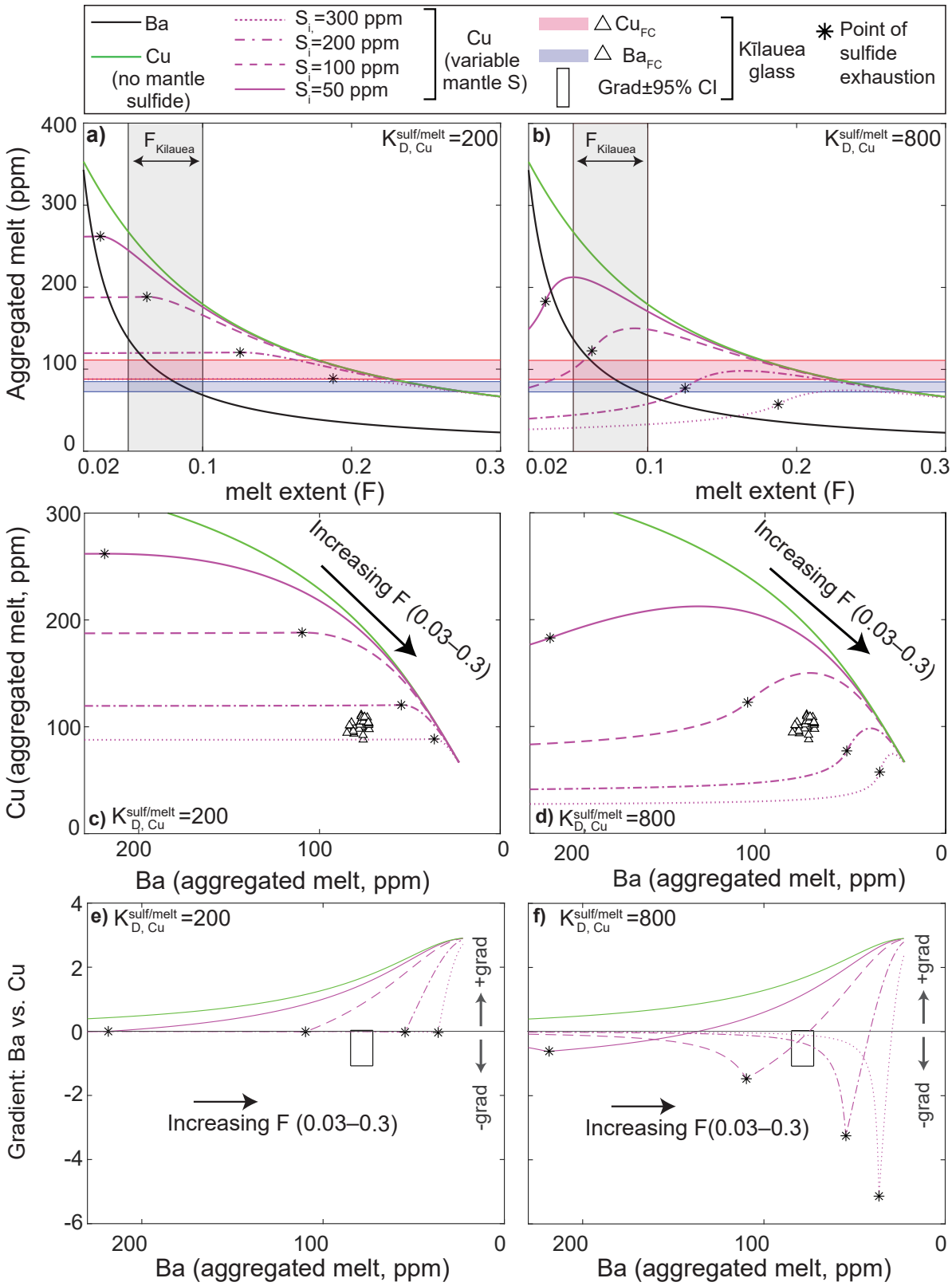

Figure 9: (Caption next page.)

Please cite the published version in GCA: Wieser et al., 2020,
https://doi.org/10.1016/j.gca.2020.05.018

Figure 9: Models of Cu and Ba contents in aggregated fractional melts with changing melt extents (F) and initial mantle S contents S_i assuming Cu_i = 20 ppm. a-**b)** Changes in the Cu contents of aggregated melts with increasing F for two different values of $K_{D,\ Cu}^{sulf/melt}$. Ba rapidly decreases with increasing melt extents (black line). If there are no sulfides in the mantle source, Cu shows a less dramatic increase (green line). The magenta lines show the evolution of Cu for four different S_i values. The point at which sulfides are exhausted (black star) moves to progressively higher F values as $S_{i/,Per}$ increases. The light pink and light blue bar show the range of Cu and Ba concentrations in fractionation-corrected Kīlauean glasses (taken to represent primary melts) from the three rift eruptions which have not fractionated beyond olivine control. In **a)**, Cu concentrations in melts produced at F=0.05–0.1 with $S_{i/,Per}$ = 200–300 ppm bracket the range of primary melt Cu contents, while in **b)**, models with $S_{i/,Per}$ = 100–200 bracket the range of observed values. c-d) Cu concentrations in aggregated melts plotted against Ba to aid visual assessment of the changing gradients following sulfide exhaustion. e-f) The gradient of Ba vs. Cu in the model vs. the Ba concentration of aggregated melts. The black rectangle shows the range of Ba concentrations in fractionation-corrected glasses, and the 95% confidence interval on the observed gradient of Cu vs. Ba (see Fig. 4d).

exhausted very early (e.g., S_i = 50 ppm; solid magenta line), Cu concentrations produced at the melt extents relevant for Kīlauea (F=0.05–0.1) are similar to those expected from melting of a mantle source which was sulfide-free throughout the melting interval (solid green vs. solid magenta line; Fig. 9a-b). As Cu is relatively incompatible in mantle silicate phases, this model exhibits a strong positive correlation between Cu and Ba for the range of Ba concentrations in Kīlauean glasses (Fig. 9e-f). Even the upper bound of the 95% confidence interval of the gradient of Cu vs. Ba in the fractionation-corrected glass compositions is ∼30–50× lower than predicted by this model (black rectangle, Fig. 9e-f). In contrast, the observed range of fractionation-corrected glass Cu concentrations (light pink bar; Fig. 9a-b; triangles on Fig. 9c-d) are only ∼2–3× lower than predicted in this model. Changing the initial concentration of Cu in the source cannot resolve these discrepancies in both the gradient and the concentration of Cu. Sulfides are also exhausted within the melting interval at Kīlauea if S_i = 100 ppm. For $K_{D,\ Cu}^{sulf/melt}$=200, models with S_i = 100 ppm display positive gradients for Cu vs. Ba and overestimate the Cu concentrations of primary melts (Fig. 9c, **e)**. For $K_{D,\ Cu}^{sulf/melt}$=800, the model with S_i = 100 ppm passes through the observed gradients, but overpredicts melt Cu contents (Fig. 9b, d).

It could be argued that a model with S_i = 150 ppm and $K_{D,\ Cu}^{sulf/melt}$=800 would recreate observed Cu and Ba concentrations without exhausting sulfide. However, the calculated gradient for this model only passes through the very bottom of the observed 95% confidence interval (Supplementary Fig. A12). Additionally, based on the Kiseeva and Wood (2015) parameterization, $K_{D,\ Cu}^{sulf/melt}$ is very unlikely to be as high as 800. For the more realistic models with $K_{D,\ Cu}^{sulf/melt}$=200, the observed gradients and concentrations of Cu are only recreated in models where sulfides are present in the mantle source throughout the melting interval incorporated by the three primitive eruptions investigated in this study. Overall,

the gradient of Cu vs. Ba provides a far more robust measure of the presence or absence of sulfide than absolute concentrations, as it is far less sensitive to the choice of poorly constrained parameters such as mantle Cu contents (Cu_i).

Based on the assumption that sulfides were present throughout the melting interval, the minimum S concentration of the Kīlauean mantle source may be estimated from the S concentration of primary melts (Sprim) and the extent of melting (F) using the equation $S_{min}= S_{prim}\times F$. Assuming melt extents between F=0.08 and 0.095 (based on Ba concentrations; Supplementary Fig. A11), and primary S concentrations of 1600 ppm, the mantle source contains a minimum of ∼130–150 ppm S. Placing further constraints on the source S content is challenging; for low values of $K_{D,\,Cu}^{sulf/melt}$ (e.g., 200), once sulfides are residual throughout the melting interval, the gradient between Cu and Ba provides no further discriminatory power (all models have gradients of ∼0; Fig. 9e-f), and Cu concentrations in the melts are invariably a trade-off between S_i and Cu_i. More precise constraints on the S concentration of the Kīlauean mantle source will require better constraints on the concentrations of other chalcophile elements in the mantle, as well as sulfide-melt partition coefficients (which likely vary as a function of T, P and sulfide composition), so that inversions can be performed for more than one chalcophile element.

4.2 Sulfide Systematics During Magma Ascent and Fractionation

Due to the increase in the $SCSS^{2-}$ with decreasing pressure, a melt that is sulfide-saturated in the mantle will generally become sulfide-undersaturated during its ascent towards the surface (Mavrogenes and O'Neill, 1999). This process was modelled by calculating the $SCSS^{2-}$ for primary melts with the adjusted composition of Clague et al. (1991) ascending along the olivine liquidus (39.16°C/GPa; Putirka, 2008) for two mantle potential temperatures (T_p=1450°C and 1650°C). For each potential temperature, the trajectory of the hottest melt formed at the onset of melting and the coolest melt formed at the base of the lithosphere was modelled (after Matthews et al., 2016; Fig. 10a). As in Fig. 7c, the decrease in the $SCSS^{2-}$ with decreasing pressure in the S2017 model (Fig. 10**b)** is an artefact of changes in the calculated sulfide composition (due to the absence of suitable parameterizations at mantle pressures and temperatures). Using a fixed sulfide composition (after Ding and Dasgupta, 2018), the S2017 and O2020 models both show similar trajectories until ∼1 GPa, where the $SCSS^{2-}$ in the O2020 model decreases, while the S2017 model continues to increase (Fig. 10c). The paucity of experimental data collected between atmospheric pressure (100 kPa and 1 GPa (Smythe et al., 2017) makes it difficult to verify the validity of these different trajectories (O'Neill, 2020). However, regardless of the exact choice of SCSS model or potential temperature, this analysis demonstrates that dropping pressures cause the $SCSS^{2-}$ to exceed the S content of primary melts (Fig .10c). Thus, sulfide saturated primary melts become sulfide undersaturated (Fig. 10c) during their ascent through the thick Hawaiian

Please cite the published version in GCA: Wieser et al., 2020,
https://doi.org/10.1016/j.gca.2020.05.018

lithosphere into shallow crustal storage reservoirs at 1–5 km depth (Cervelli and Miklius, 2003; Poland et al., 2014). The probable presence of S^{6+} species in primary melts (Fig. 8b-**c)** will shift the $SCSS_{Tot}$ to higher S contents than the $SCSS^{2-}$ models shown in Fig .10, resulting in melts becoming sulfide undersaturated at even higher pressures during their ascent. Similarly, if melts were to ascend along an adiabatic gradient instead of the olivine liquidus, the temperature decrease upon ascent would be smaller, resulting in higher values of the $SCSS^{2-}$, and the onset of sulfide undersaturation at higher pressures.

Sulfide-undersaturated primary melts supplied to shallow crustal storage reservoirs at Kīlauea may experience a second phase of sulfide saturation during crystal fractionation. Recent work has concluded that the majority of erupted melts at Kīlauea are sulfide-undersaturated until ∼2 wt% MgO (Ding and Dasgupta, 2018; Greaney et al., 2017; Helz et al., 2017). However, this view is difficult to reconcile with the ubiquitous presence of sulfides in the relatively primitive eruption products investigated in this study (Fig. 5), unless sulfides form during late stage processes such as quenching, rather than primary sulfide immiscibility (Stone and Fleet, 1991). We assess the possibility that sulfides form upon quench by comparing bulk sulfide compositions measured using EDS mapping to the predicted sulfide compositions from $SCSS^{2-}$ models. Sulfides formed through primary sulfide immiscibility will progressively evolve towards more Cu-rich and Ni-poor compositions with increasing fractional crystallization. Conversely, sulfides formed during quench-induced segregation and cooling will show extreme compositional variability (Stone and Fleet, 1991; Fleet and Stone, 1990). The sulfide compositions predicted by $SCSS^{2-}$ models were calculated for Petrolog3 fractionation paths from the adjusted primary melt composition of Clague et al. (1991) at 1 kbar (Supplementary Fig. A3). The mineral models of Danyushevsky (2001) were used for olivine, clinopyroxene and plagioclase. Melt Ni concentrations were modelled assuming Ni_i=900 ppm, using $K_{D,\ Ni}^{ol/melt}$ from Beattie et al. (1991), $K_{D,\ Ni}^{cpx/melt} = 2.6$ from Mysen (1978), and $K_{D,\ Ni}^{plag/melt} = 0$. Melt Cu concentrations were modelled assuming Cu_i=100, using $K_{D,\ Cu}^{ol/melt} = 0.1$, $K_{D,\ Cu}^{cpx/melt} = 0.21$ (Greaney et al., 2017) and $K_{D,\ Cu}^{plag/melt} = 0.14$ (Bougault and Hekinian, 1974).

To assess changes in sulfide chemistry during fractionation (and to compare measured sulfide compositions to those predicted by $SCSS^{2-}$ models), the MgO content of the melt at the time of formation for each Kīlauean sulfide was estimated. Sulfides hosted in matrix glasses or embayments were allocated an equivalent melt MgO content equal to that of the host glass. For sulfides hosted in olivine crystals and melt inclusions, the forsterite content of the host olivine was compared to olivine compositions from the Petrolog3 model, and the sulfide was assigned the liquid MgO content at which the measured olivine composition fractionated.

Contrary to the observations of Stone and Fleet (1991) that bulk sulfide compositions from Kīlauea Iki are highly variable, bulk sulfide compositions measured in this study show

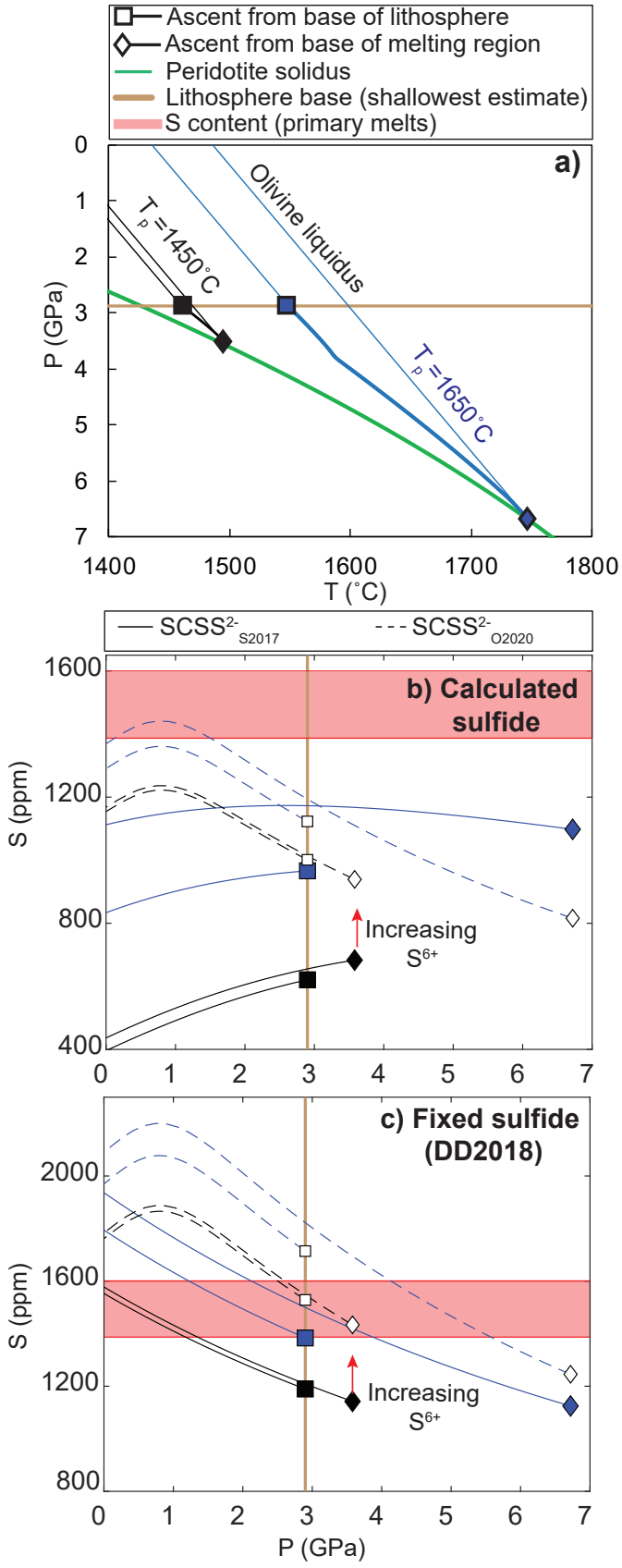

Figure 10: Modelling the $SCSS^{2-}$ during the ascent of melts from the mantle into shallow crustal storage reservoirs. **a)** PT paths tracking the ascent of mantle melts generated at bottom and top of the melting column along the olivine liquidus (39.16 °C/GPa; after Matthews et al., 2016). **b-c)** Calculated $SCSS^{2-}$ trajectories for these ascent paths, using the adjusted primary melt composition of Clague et al. (1991) for calculated (**b**) and fixed sulfide compositions (**c**). As in Fig. 7, the decrease in the $SCSS^{2-}$ with decreasing pressure in the 2017 model is an artefact of the changing sulfide composition. Similarly, calculated sulfide compositions are far more Fe-poor than measured sulfides, leading to anomalously low $SCSS^{2-}$ values. In **c**), all modelled trajectories except for the lowest T_p (1450 °C

in the S2017 model exceed the S concentrations of primary melts (red bar) at low pressures. The presence of even a very small amount of S^{6+} would mean that the $SCSS_{Tot}$ for this model would also exceed the S contents of primary melts. These models indicate that upon ascent, Kīlauean magmas become sulfide-undersaturated. The beige line marks the shallowest estimate for the base of the lithosphere beneath Kīlauea (Li et al., 2004; Wölbern et al., 2006.

coherent changes in Cu and Ni with decreasing melt MgO contents, and relatively little chemical variability (Fig. 11a-b). Furthermore, the Ni and Cu contents of the sulfides fall between the calculated sulfide compositions from the S2017 and O2020 $SCSS^{2-}$ models. Coherent variations in sulfide compositions have also been reported for sulfides in samples from the 1955 eruption (Helz and Wright, 1992). It is plausible that scatter in previously reported sulfide compositions from Kīlauea results from the analytical challenges associated with obtaining bulk compositions from EPMA spot analyses of exsolved sulfides. Thus, we conclude that observed sulfides are the result of primary sulfide fractionation.

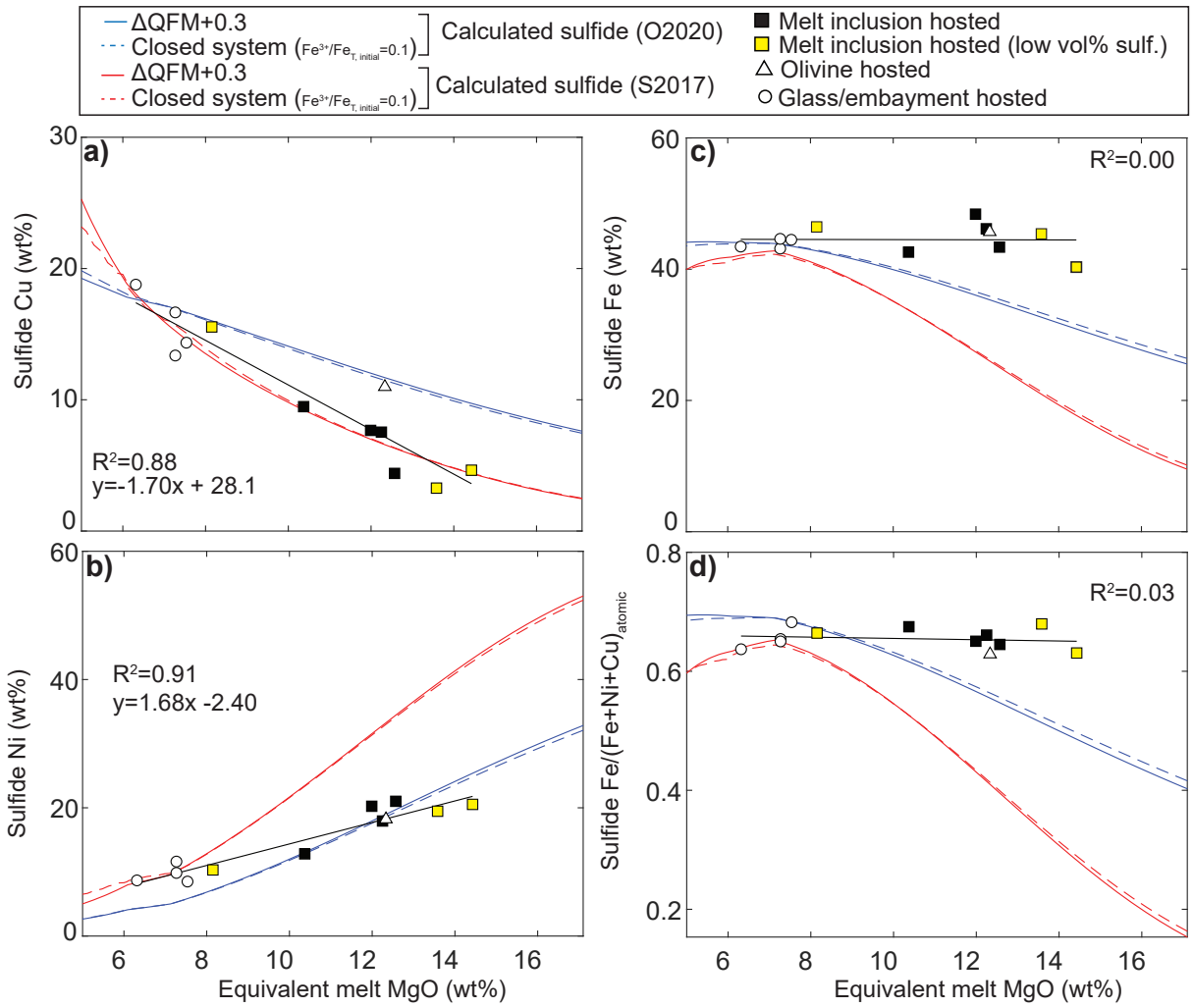

Figure 11: Comparison of measured sulfide compositions to those calculated from $SCSS^{2-}$ models. Bulk sulfide compositions were obtained from EDS maps (quantified by analysing sulfide standards in the same analytical session whose compositions were determined by EPMA). Equivalent melt MgO contents for each sulfide were allocated from glass MgO contents, or olivine Fo contents (see section 4.2). Modelled sulfide compositions were calculated for Petrolog3 fractionation path described in the text. Closed system and buffered models yield very similar calculated sulfide compositions (dashed vs. solid lines). Sulfides which could plausibly have grown following their entrapment in melt inclusions (based on volume proportions <0.2%) are colored yellow.).

Our hypothesis that sulfides form during primary sulfide saturation is supported by the presence of sulfides trapped within the cores of olivine crystals (Fig. 5**a)**, often associated with small pockets of melt and spinels (Fig. 5f-h). These textural associations cannot be explained by quenching processes, or the formation of sulfides following melt inclusion entrapment (e.g. Hartley et al., 2017), as there is simply not enough Cu, Ni and S in these small pockets of melt to form sulfides of the observed sizes after the melt inclusion became a closed system (Supplementary Fig. A5). Only sulfides hosted in melt inclusions where the volume ratio of the sulfide to melt is very low could have grown following melt inclusion entrapment (e.g., ∼0.04%, Fig. 5e, yellow squares on Fig. 11). The attachment of sulfides to olivine crystals (e.g., Fig. 5c, **f)** suggests that sulfides may have a stronger affinity for nucleation or attachment to silicate minerals than the silicate melt. The attachment of sulfides to the boundary layer of a growing crystal likely accounts for their incorporation as inclusions. In fact, this process may even trigger the formation of melt inclusions containing sulfides in a similar mechanism to that proposed for inclusions containing chrome-spinels (Maaløe and Hansen, 1982). Overall, our chemical and textural observations of sulfides are consistent with their formation through primary sulfide saturation during differentiation, followed by their subsequent entrapment within growing crystals (often alongside spinels and silicate melt; Nadeau et al., 2010). The occurrence of sulfides hosted within highly primitive olivine crystals (Fo_{87-88}) alongside very small quantities of melt (Fig. 5a, h, g, Supplementary Fig. A5) suggests that sulfides saturated at ∼12 wt% MgO.

We investigate this second stage of sulfide saturation by comparing fractionation trajectories for S (assuming S is incompatible in silicate phases) with $SCSS^{2-}$ models for each Petrolog3 fractionation path. The $SCSS^{2-}$ is sensitive to melt composition (particularly the FeO content), oxidation state (Fe^{3+}/Fe_T), temperature, pressure and the composition of co-existing sulfides (Smythe et al., 2017; O'Neill, 2020). During fractional crystallization at Kīlauea, olivine is the only silicate phase on the liquidus until 6.8 wt% MgO (Wright and Fiske, 1971). Over this fractionation interval, melt FeO contents remain approximately constant (Supplementary Fig. A3). Although $SCSS^{2-}$ models predict an increase in the ratio of Fe/(Fe+Cu+Ni) in sulfides with progressive fractionation, this ratio remains remarkably constant in measured bulk sulfide compositions (Fig. 11d), so we fix this parameter at 0.646 in all models. Use of calculated, rather than fixed sulfide compositions, results in spuriously low $SCSS^{2-}$ values (Supplementary Fig. A12). As magma storage (and fractionation) at Kīlauea is restricted to a narrow range of depths (∼1–5 km; Cervelli and Miklius, 2003), changing pressures during fractionation have a negligible effect on the $SCSS^{2-}$.

Changes in melt redox state during fractionation are less certain. Due to an absence of measurements of Fe^{3+}/Fe_T in Kīlauean melts with >10 wt% and <7 wt% MgO (Fig. 8**a)**, it is difficult to determine whether melts follow a redox buffer, or act as a closed system for oxygen. Additionally, the re-interpretation of Mössbauer spectra in glass standards which are integral

Please cite the published version in GCA: Wieser et al., 2020,
https://doi.org/10.1016/j.gca.2020.05.018

to XANES calibrations (Berry et al., 2018; Zhang et al., 2018) has resulted in significant uncertainty regarding the oxidation state of Kīlauean melts. Literature data utilizing the calibration of Cottrell et al. (2009) prior to the emergence of this Mössbauer-focused debate are well matched with models buffered at QFM+0.6 to 0.7, or closed system models for Fe^{3+}/Fe_T=0.129 (Fig. 8a). However, following the application of the Berry et al. (2018) correction, published data is best matched with models buffered at QFM to QFM+0.3, or closed system models with $Fe^{3+}/Fe_{T,\,initial}$=0.1 (Fig. 8**a**):

$$\frac{Fe^{3+}}{Fe_T}(\text{Corrected}) = \frac{\frac{Fe^{3+}}{Fe_T}(\text{Published}) - 0.065}{1 - 0.065},$$

The Zhang recalibration yields Fe^{3+}/Fe_T ratios between published values and those corrected using the equation of Berry et al. (2018). However, other than subtle changes in the MgO content at which clinopyroxene and plagioclase begin to crystallize, the closed system and buffered model show very similar major element systematics (Supplementary Fig. A3). Consequently, the $SCSS^{2-}$ trajectories for models with different redox conditions are very similar, with subtle differences resulting from the different sensitivities of the S2017 and O2020 model to the Fe^{3+}/Fe_T ratio.

$SCSS^{2-}$ models (Fig. 12a-b) intercept fractionation trajectories for S at high MgO (∼13–17 wt% MgO). Below ∼12 wt% MgO, the calculated $SCSS^{2-}$ is significantly lower than the measured S contents in melt inclusions, even accounting for the upper 1σ error envelope on the S2017 parameterization (red dotted line). This discrepancy indicates that Kīlauean melts likely contain S^{6+} species, which increase the total solubility of S (Equation 1). We perform several corrections to account for the presence of S^{6+}. The first, and most simplistic, assumes that the proportion of S^{6+} remains constant throughout the fractionation interval at Kīlauea. Based on available S-redox measurements in submarine glasses from Mauna Kea and Lōi‘hi (Jugo et al., 2010; Brounce et al., 2017; Wallace and Carmichael, 1994), this proportion may range from 0–30% (Fig. 8b-c). The S2017 $SCSS_{Tot}$ model with 30% S^{6+} and the O2020 model with 20% S^{6+} predict the onset of sulfide saturation at ∼12 wt% MgO (consistent with textural observations; Fig. 11), and approximately recreate the upper observed limit of S contents in melt inclusions at lower MgO contents (Fig. 12c-d).

The proportion of S^{6+} can also be estimated from the experimental parameterizations of Jugo et al. (2010) and Nash et al., 2019 (Equations 2-3). ΔQFM values for the Jugo et al. (2010) parameterization, and Fe^{2+}/Fe^{3+} ratios for the Nash et al. (2019) parameterization were calculated from Petrolog3 outputs, and melt temperatures were calculated using the geothermometer of Helz and Thornber, 1987. Unlike the subtle differences in $SCSS^{2-}$ models, the proportion of S^{6+}, and by extension, the $SCSS_{Tot}$, is highly sensitive to redox changes during fractionation. Closed system models show a gradual increase in the Fe^{3+}/Fe_T ratio during olivine-only fractionation (due to the removal of Fe^{2+}-rich olivine; Carmichael and

Ghiorso, 1986; Moussallam et al., 2016; Fig 8a). As clinopyroxene and plagioclase begin to fractionate, this ratio increases more rapidly per unit decrease in MgO. In contrast, the buffered model exhibits a constant Fe^{3+}/Fe_T ratio during olivine-only fractionation, followed by a slight decrease at lower MgO contents (Fig. 8a).

The proportion of S^{6+} predicted by the Jugo et al. (2010) model for the closed system fractionation path with $Fe^{3+}/Fe_{T,\,initial}$=0.1 is negligible until the onset of plagioclase fractionation at ∼6 wt% MgO. The closed system fractionation path starting at higher initial Fe^{3+}/Fe_T ratios (=0.129) is offset to higher S^{6+}/S_T ratios, but still predicts <10% S^{6+} during olivine (+minor chromite) fractionation. In the buffered model, by definition, the proportion of S^{6+} predicted by Jugo et al. (2010) remains constant at 0.8% (QFM), 3% (QFM+0.3), and 11% (QFM+0.6). Due to the dependency of the Nash et al. (2019) model on both temperature and Fe^{3+}/Fe_T, the proportions of S^{6+} follow significantly more complex trajectories. In the three buffered models the Fe^{3+}/Fe_T ratio is constant during olivine-only fractionation, so there is a rapid decrease in the S^{6+}/S_T ratio because of dropping temperatures. A slight drop in Fe^{3+}/Fe_T ratios during crystallization of plagioclase and pyroxene causes a kink in the downward trajectory of these curves. In contrast, the closed system models show an almost constant S^{6+}/S_T ratio during olivine-only fractionation, because of the competing effects of dropping temperatures and increasing Fe^{3+}/Fe_T ratios. During crystallization of plagioclase and pyroxene, increasing Fe^{3+}/Fe_T ratios overwhelm the effect of dropping temperatures, so the S^{6+}/S_T ratio increases rapidly. Based on the paucity of S-redox measurements in the literature, and the prominent differences between measurements in the same samples by different studies (e.g., cyan vs. green dots; Fig. 8 c), it is difficult to assess the validity of these different model outputs. For simplicity, the $SCSS_{Tot}$ was calculated for a fractionation path buffered at QFM+0.3, and for a closed system with $Fe^{3+}/Fe_{T,\,initial}$=0.1), to demonstrate the sensitivity of total sulfur solubility to S^{6+}/S_T ratios.

In the closed system model ($Fe^{3+}/Fe_{T,\,initial}$=0.1), the $SCSS_{Tot}$ calculated using the Jugo et al. (2010) or Nash et al. (2019) parameterization only deviate outside of the 1σ uncertainty of the $SCSS^{2-}$ after the onset of plagioclase fractionation at ∼6 wt% MgO (Fig. 12e-g). The upkick towards higher S contents is most pronounced in the Jugo et al. (2010) parameterization (Fig. 12e), because of the competing effects of increasing Fe^{3+}/Fe_T and dropping temperatures in the Nash et al. (2019) parameterization. Due to the low and constant proportion of S^{6+} (3%) in the model buffered at QFM+0.3 using the Jugo et al. (2010) parameterization, the $SCSS_{Tot}$ and the $SCSS^{2-}$ are almost identical. In contrast, the $SCSS_{Tot}$ calculated using the Nash et al. (2019) parameterization deviates substantially from $SCSS^{2-}$ models at high MgO contents (where high S^{6+}/S_T ratios are predicted due to high temperatures). The most significant deviation between these four $SCSS_{Tot}$ models occurs at MgO contents >14 wt% (e.g., Fig. 12h vs. Fig. 12e, f, g), and following the onset of plagioclase fractionation (e.g., Fig. 12e, g vs. Fig. 12f, h). The absence of published

Please cite the published version in GCA: Wieser et al., 2020,
https://doi.org/10.1016/j.gca.2020.05.018

Fe^{3+}/Fe_T and S^{6+}/S_T ratios for melt inclusions with these low and high MgO contents, as well as the absence of published S data for low MgO content melt inclusions, makes ground truthing these different model scenarios challenging.

Despite the differences between $SCSS_{Tot}$ models, all six predict that the onset of sulfide fractionation occurs at relatively high MgO contents ($\gg$2 wt% MgO; Wallace and Anderson, 1998; cf.Greaney et al., 2017), supporting our textural and chemical observations that the vast majority of erupted Kīlauean melts were sulfide-saturated at depth. Based on the absence of constraints for changes in S redox state with differentiation, we favour models using constant S^{6+} proportions, which recreate available textural and chemical constraints regarding the onset of sulfide saturation at Kīlauea (Fig. 11, Fig. 12a-b). These findings further support our inference that mantle melting occurred in the presence of residual sulfides, as melts generated in a mantle which had exhausted sulfide require large amounts of fractionation to intercept the $SCSS_{Tot}$ following ascent to low pressures (Liu et al., 2014).

Figure 12: Comparison of models for sulfide solubility during fractionation (for a specified sulfide composition of Fe/(Fe+Ni+Cu)=0.646) with PEC-corrected melt inclusion compositions. **a-b)** In models only accounting for S^{2-} species, the $SCSS^{2-}$ intercepts the fractionation trajectory for S at high MgO contents (blue bar shows interception for O2020), and underpredicts the S contents of most melt inclusions with <12 wt% MgO. The closed system and buffered model show very similar trajectories, and the O2020 and S2017 are within error of one another (the red dotted lines indicate the published 1 uncertainty on the S2017 model). **c-d)** $SCSS_{Tot}$ trajectories for constant proportions of S^{6+} during differentiation (10%, 20% and 30%). The S2017 model with 30% S^{6+} , and the O2020 model with 20% S^{6+} predict the onset of sulfide saturation at 10–12 wt% MgO (inline with textural observations, Fig. 11), and approximately bracket the upper limit of melt inclusion S contents. **e-f)** $SCSS_{Tot}$ trajectories following a correction for S^{6+} using the parameterization of Jugo et al. (2010; equation 2). The closed system and buffered model differ substantially following the onset of plagioclase fractionation (see Fig. 8b-c). **g-h)** SCSSTot trajectories following a correction for S^{6+} using the parameterization of Nash et al. (2019; equation 3). As in **e)**, the closed system model shows a sharp increase in S solubility during plagioclase fractionation. In the open system model, the strong temperature dependence on the proportion of S6+ results in very high estimates of S solubility at high MgO contents.

Please cite the published version in GCA: Wieser et al., 2020,
https://doi.org/10.1016/j.gca.2020.05.018

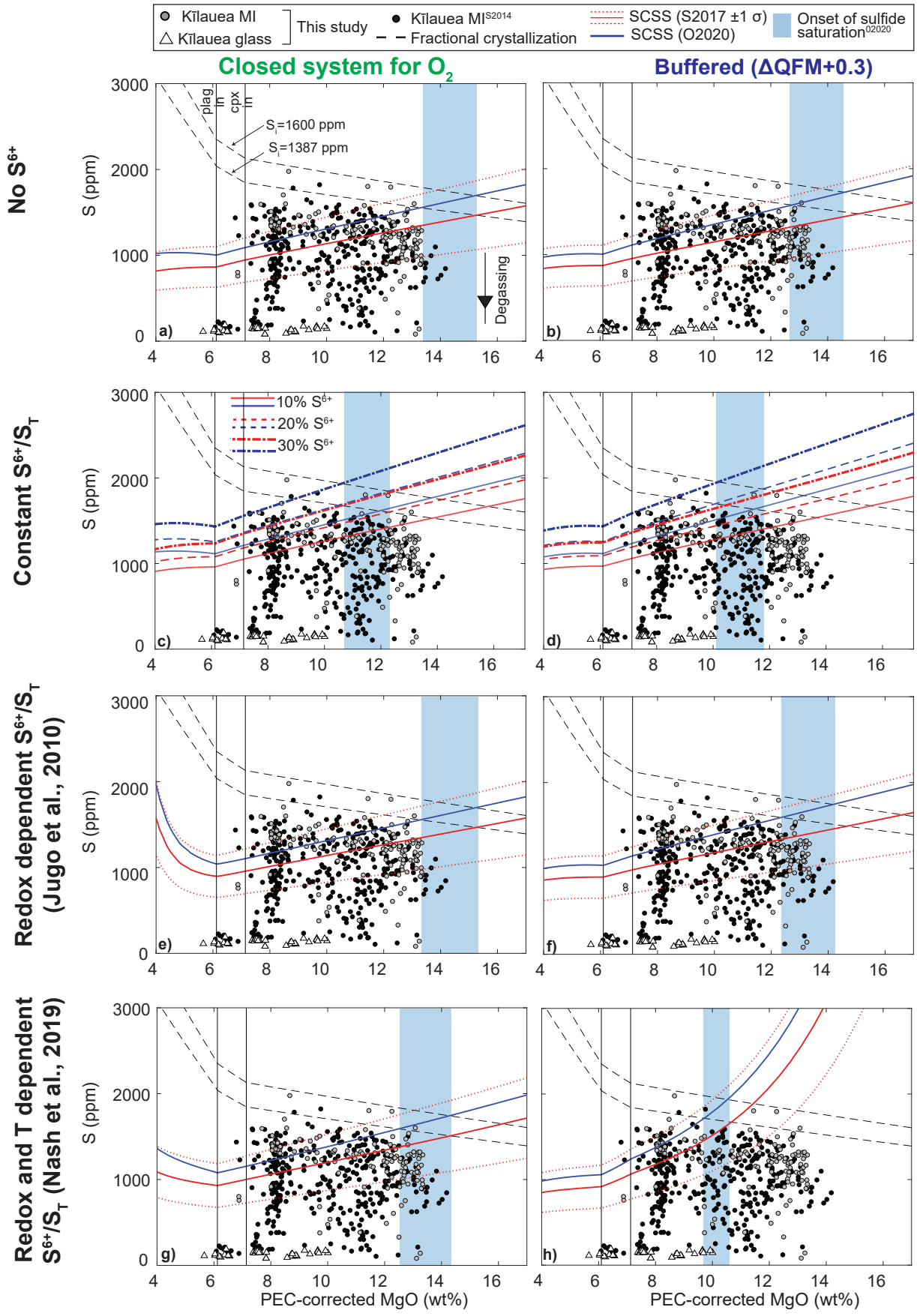

Figure 12: (Caption previous page.)

Please cite the published version in GCA: Wieser et al., 2020,
https://doi.org/10.1016/j.gca.2020.05.018

4.3 Sulfide Saturation in Lava Lakes

The prevalent view at Kīlauea that sulfides only saturate following extensive fractionation is not supported by our models of sulfide solubility, or textural observations of sulfide occurrence. This discrepancy may result from the focus of previous studies on chemical trajectories defined by samples collected from lava lakes (e.g., Greaney et al., 2017; Pitcher et al., 2009; Stone and Fleet, 1991). A comparison of the S contents of melt inclusions and matrix glasses clearly demonstrates that basaltic melts at Kīlauea degas >90% of their S during subaerial eruptions (∼1600 ppm to ∼135 ppm; Fig. 1c; Fig. 2a-b). Kīlauea Iki and Alae lava lakes formed by the ponding of S-poor melt within existing pit craters, followed by extensive fractionation (Wright et al., 1976). As the erupted melts filling these lava lakes have similar MgO contents to those examined in this study, it is reasonable to assume that these magmas were sulfide-saturated prior to their ascent to the surface. However, extensive degassing upon eruption would have caused the S content of the melt to fall well below the $SCSS_{Tot}$, driving sulfide resorption (Edmonds and Mather, 2017; Moore et al., 1980; Reekie et al., 2019). Subsequent fractionation within these lava lakes may then have proceeded under sulfide-undersaturated conditions.

We model the onset of sulfide saturation within lava lakes by calculating the $SCSS^{2-}$ using the major element compositions of variably evolved glasses from the Kīlauea Iki lava lake (Fig. 1b; Greaney et al., 2017). For simplicity, the amount of S^{6+} in the fractionating lava lake was assumed to be negligible, as extensive degassing of S upon eruption causes a significant drop in the Fe^{3+}/Fe_T ratio (Fig. 8a, Moussallam et al., 2016). The evolution of S during progressive fractionation within the lake is uncertain; while the crystallization of silicate minerals drives melt S contents up, the presence of vesicles within lake lava samples and observations of gas release along drill holes suggests that lava lakes continued to lose volatiles during differentiation (Helz and Wright, 1983; Peck, 1978; Wright et al., 1976). To incorporate this uncertainty, we consider the interception of the regression lines for the calculated $SCSS^{2-}$ vs. MgO with the range of S contents in degassed glasses from Kīlauea Iki pumices (orange histogram; Fig 1b; Sides et al., 2014b), and the S content measured in Alae lava lake (green line; Moore et al., 1980; Fig. 1b). These models predict that the third stage of sulfide saturation at Kīlauea will occur at ∼2 wt % MgO, which is consistent with observations that Cu suddenly decreases below 2 wt% MgO in the Kīlauea Iki lava lake (Fig. 1a; Greaney et al., 2017). This third stage of sulfide saturation has been attributed to the uptake of Fe^{3+} in Fe-Ti oxides (Greaney et al., 2017) driving S reduction in a mechanism similar to the "magnetite crisis" in arc basalts (Jenner et al., 2010). However, our modelling successfully predicts the onset of sulfide saturation without incorporating changes in redox state (Fig. 1b). Instead, the decrease in the $SCSS^{2-}$ is largely driven by changes in the major element concentration of the melt, with a contribution from dropping temperatures. Overall, while lava lakes provide useful insights into the mechanism and timing of sulfide saturation in extensively degassed melts, they are clearly not representative of the fractionation path of undegassed melts within crustal storage reservoirs at Kīlauea.

Please cite the published version in GCA: Wieser et al., 2020,
https://doi.org/10.1016/j.gca.2020.05.018

4.4 Degassing of Chalcophile Elements

Aerosol measurements at Kīlauea reveal that, in addition to conventionally volatile elements (e.g., CO2, H2O, S, Cl and F), the volcanic plume also contains considerable quantities of chalcophile elements (Edmonds et al., 2018; Mather et al., 2012). The extent to which an element degasses is represented by the emanation coefficient (ε), which quantifies the proportion of an element lost during degassing:

$$\varepsilon = \frac{[X]_i - [X]_f}{[X]_i} \tag{1.4}$$

Where $[X]_i$ and $[X]_f$ are the concentrations of element X in the initial undegassed and final degassed melt respectively (Edmonds et al., 2018; Lambert et al., 1985). Previous petrological work investigating chalcophile element degassing at various Hawaiian volcanoes utilized suites of variably degassed submarine glasses to estimate emanation coefficients (Norman et al., 2004). They observed degassing trends for S (ε=0.86–0.92), Re (ε=0.5–0.74), Bi (ε=0.44–0.45), and Cd (ε=0.19–0.27). However, as Norman et al. (2004) compare glasses from different Hawaiian islands (Ko'olau and Moloka'i), it is difficult to deconvolve the effects of degassing from variations in the original chalcophile contents of these melts.

In this study, emanation coefficients were evaluated by comparing chalcophile element concentrations in melt inclusions (which are variably degassed) and matrix glasses (which have extensively degassed; Fig. 3). However, such comparisons rely on the assumption that melt inclusions are genetically related to their matrix glasses. Lithophile trace element ratios in olivine-hosted melt inclusions from the three rift eruptions investigated in this study show considerable overlaps, despite statistically significant changes in the composition of the co-erupted matrix glass. This indicates that these melt inclusions were trapped from a variety of magma batches present within Kīlauea's plumbing system over centuries, and subsequently brought to the surface in an unrelated magma batch (Wieser et al., 2019, see also Tuohy et al., 2016). Only the 1971 summit eruption contains a crystal cargo that crystallized from the carrier liquid, permitting a direct comparison between melt inclusions and co-erupted glasses. Fortunately, the presence of residual sulfides in the mantle source means that chalcophile element concentrations do not differ as much as lithophile element concentrations between different magma batches (Fig. 4). Thus, degassing can be assessed by comparing the matrix glasses and melt inclusions, considering the data from all four eruptions together.

Emanation coefficients were calculated using Equation 4. $[X]_f$ was calculated from regression line of a given element [X] against S for S=135 ppm (the average S content of degassed matrix glasses). The value of $[X]_i$ calculated from the regression lines is sensitive to the amount of S degassed (ΔS); to incorporate this uncertainty, $[X]_i$ was calculated from the regression lines at S=1435 ppm and S=1585 ppm (ΔS=1300 ppm and ΔS=1450 ppm respectively). The uncertainty on the emanation coefficient for a given ΔS was estimated using the 95% confidence intervals of the regression (see Supplementary Fig. A13).

Please cite the published version in GCA: Wieser et al., 2020,
https://doi.org/10.1016/j.gca.2020.05.018

The concentrations of many chalcophile elements in melt inclusions and matrix glasses overlap (Loewen, 2013), making it difficult to accurately assess the emanation coefficient, and determine whether a given element is degassing (Fig. 3d-f). We consider several possible criteria to robustly assess whether an element shows petrological evidence for degassing. The first criterion is based on the fact that gaseous observations indicate that Cl partially degasses at Kīlauea (Edmonds et al., 2009). Melt inclusion Cl contents overlap with and extend to higher values than matrix glasses, with the most S-rich (least degassed) inclusions generally having higher Cl contents (Fig. 3a). We classify a chalcophile element as showing evidence for subaerial degassing if a regression line between that element and S exhibits a higher R^2 value than Cl vs. S (R^2=0.14). This criterion classifies Se (R^2=0.90), Bi (R^2=0.35) and As (R^2=0.19) as degassed (Fig. 3).

The second criterion is based on a comparison of mean concentrations of chalcophile elements in PEC-corrected melt inclusions and matrix glasses from the 1971 summit eruption (where melts trapped within crystals and the co-erupted matrix glass have similar trace element signatures; Wieser et al., 2019) using the ANOVA test. The small diameter of melt inclusions from this eruption meant that As and Se could not be measured. An element was classified as degassed if $p<0.05$. This criterion only classifies Bi as degassed ($p=9\times10^{-4}$), with no distinguishable differences between matrix glasses and PEC-corrected melt inclusion compositions for Cu (p=0.08), Zn (p=0.66), Mo (p=0.77), Cd (p=0.27), In (p=0.90), Sn (p=0.28), Sb (p=0.21), W (p=0.60), or Tl (p=0.16), despite the fact that aerosol measurements indicate that these elements are present in the volcanic plume at Kīlauea (Mather et al., 2012).

The third criterion involves a comparison of the concentrations of chalcophile elements in Kīlauean and Lōi‘hi glasses. Lōi‘hi glasses were erupted at water depths of ∼1000–4700 m (Pietruszka et al., 2011), so remain largely undegassed with respect to H_2O and S (Fig. 3a). For certain elements (e.g., Se, Bi, Cd), Lōi‘hi glasses plot with the least degassed Kīlauean melt inclusions, supporting the hypothesis that these elements have degassed from Kīlauean matrix glasses during subaerial eruptions. However, As concentrations in Lōi‘hi glasses are lower than in Kīlauean melt inclusions (Fig. 3d), suggesting that Lōi‘hi and Kīlauea magmas may have slightly different chalcophile element signatures (perhaps attributable to differences in the mantle source, or the fact that Lōi‘hi glasses have experienced clinopyroxene fractionation).

To reconcile the lack of petrological evidence for degassing of many chalcophile elements which are detected in volcanic plumes, we calculate the expected change in the concentration of each chalcophile element for ΔS=1300 ppm using the X/S ratios measured in the 2008 summit plume (Mather et al., 2012). For many elements, this change is far smaller than the median analytical precision of in-situ melt inclusion measurements estimated from the 2σ variation in the LA-ICP-MS signal during melt inclusion ablation (from Iolite). For

example, the 2σ variation is $\sim$411$\times$ larger than the predicted loss of Cu during degassing ($\sim$7$\times$ for As and Zn, $\sim$9$\times$ for Bi, $\sim$10$\times$ for Cd, $\sim$23$\times$ for Pb, $\sim$23$\times$ for Tl, 367$\times$ for Mo, and $>$1000$\times$ for Tl). is perhaps unsurprising that the only element that shows unambiguous petrological evidence for degassing is Se, where the analytical precision is only $\sim$0.15$\times$ the expected loss during degassing.

While the degassing of most chalcophile elements is obscured by analytical noise and natural variability in melt compositions, a crucial finding of this study is that S and Se exhibit a strong positive correlation in melt inclusions and glasses, indicating that these elements are degassing concurrently (Fig. 3b, R^2=0.90). Extensive degassing of Se during subaerial eruptions is consistent with aerosol measurements at Kīlauea (Crowe et al., 1987; Edmonds et al., 2018; Mather et al., 2012) and whole-rock analyses of lavas from Antuco, Chile (Cox et al., 2019). However, in subaqueous eruptions (e.g., MORB and oceanic plateau basalts), Se is thought to be less volatile than S and is often used to reconstruct the behaviour of S prior to degassing (Brenan, 2015; Jenner et al., 2012; Jenner et al., 2010; Jenner et al., 2015; Reekie et al., 2019; Patten et al., 2013). The preservation of high Se contents in Lōi'hi glasses erupted at depths $>$1000 m indicates that the onset of Se degassing takes place at pressures of $<$0.1 kbar. Experimental work assessing the volatility of Se is ambiguous. During preparation of glass reference materials, Se is retained while S is lost (Jenner et al., 2009; Jochum et al., 2006). Yet, experiments on sulfides in the Se-S system (Helmy and Fonseca, 2017), and on chondritic meteorites (Wulf et al., 1995), demonstrate that Se has a similar volatility to S. Thus, although the exact cause of Se degassing at Kīlauea is beyond the scope of this study, we caution that the assumption that Se is less volatile than S may be invalid at low pressures. As metal emissions for Se at arc volcanoes are elevated above those at Kīlauea (Edmonds et al., 2018), it seems likely that Se degasses during subaerial eruptions in a wide variety of tectonic settings.

4.5 Sulfide Resorption During Magma Degassing

The strong partitioning of S into the gas phase during ascent and eruption causes melt S contents to drop below the $SCSS_{Tot}$, destabilizing sulfide liquids (Edmonds and Mather, 2017; Gerlach and Nordlie, 1975; Fig. 1, Fig. 12a). At hotspot volcanoes, emanation coefficients calculated from aerosol measurements of volcanic plumes have been shown to broadly correlate with sulfide-silicate melt partition coefficient (Edmonds et al., 2018). This, along with literature observations of sulfides attached to bubbles, has led to suggestions that chalcophile elements held within sulfides are directly transferred to the gas phase during sulfide resorption (Mungall et al., 2015; Nadeau et al., 2010). Alternatively, the quantity of chalcophile elements released into the gas phase may depend on the three-way partitioning between sulfide, melt and vapour (Edmonds et al., 2018).

Please cite the published version in GCA: Wieser et al., 2020,
https://doi.org/10.1016/j.gca.2020.05.018

The near-absence of sulfides in matrix glasses from subaerial eruptions at Kīlauea, but presence of sulfides as inclusions in silicate minerals and within undegassed embayments, is convincing evidence that sulfides in contact with the degassing melt resorb (Fig.5; Gerlach and Nordlie, 1975; Moore et al., 1980; Reekie et al., 2019). Further evidence is provided by the presence of resorbed features (∼20 μm in size) in degassed matrix glasses, which predominantly consist of Fe and O, with small regions of Cu-S rich material (∼1 μm; Fig. 6; Supplementary Fig. A8). Their chemistry and texture is highly indicative of the breakdown of sulfides to form Fe-oxide phases (e.g., magnetite) which are metal poor (Berlo et al., 2014; Edmonds and Mather, 2017; Nadeau et al., 2010). Only sulfides which are isolated from the degassing melt, including those trapped within olivine crystals, melt inclusions, and S-rich embayments, survive syn-eruptive degassing (Fig. 5).

However, differences in chalcophile element concentrations in melt inclusions and matrix glasses do not support a model where sulfide breakdown releases chalcophile elements "almost quantitatively" into the gas phase Mungall et al., 2015). Firstly, there is no correlation between sulfide-melt K_Ds and the emanation coefficients estimated in this study from comparisons of melt inclusion and matrix glass concentrations (Fig. 3; Fig. 13). Our emanation coefficients for Cd, Bi and S are remarkably similar to those estimated by Norman et al. (2004) and overlap with those calculated from the X/S ratios in the 2008 plume for Cu, Ni, Cd, and Se (Mather et al., 2012; Fig. 13). These published emanation coefficients also show no correlation with sulfide-melt K_Ds.

A comparison of Cu (and Ni) contents in melt inclusions and matrix glasses provides further insights into elemental partitioning between sulfides, melt, and vapour. A significant proportion of melt inclusions have lower Cu contents than matrix glasses (Fig. 2c, 3f, 14a-b, Loewen, 2013). These compositional differences between melt inclusions and matrix glasses are most obvious in the 1971 summit eruption (where trace element ratios indicate that olivine crystals grew in their carrier melts; Wieser et al., 2019). Raw and PEC-corrected Ni and Cu contents of these melt inclusions follow trajectories consistent with the removal of sulfides with compositions estimated from the regression lines in Fig. 11a-b (see caption, Fig. 14a; Supplementary Fig. 14). In contrast, matrix glasses mostly plot along the sulfide-free fractional crystallization trajectory (red line; Fig. 14a). Although the melt inclusion record in the other three eruptions is complicated by the fact that host olivines trapped a diverse range of melt compositions present in the plumbing system over centuries, when these three eruptions are considered together, melt inclusions form a wedge towards lower Cu and Ni contents that is bracketed by fractionation lines for predicted sulfide compositions at ∼8 and ∼12 wt% MgO (Fig. 14b).

Differences between the trajectory of melt inclusions and glasses in Ni-Cu space could be interpreted in two ways. Firstly, Fe-loss associated with PEC may have triggered the growth of a sulfide, sequestering melt inclusion Ni and Cu from the melt inclusion (Danyushevsky

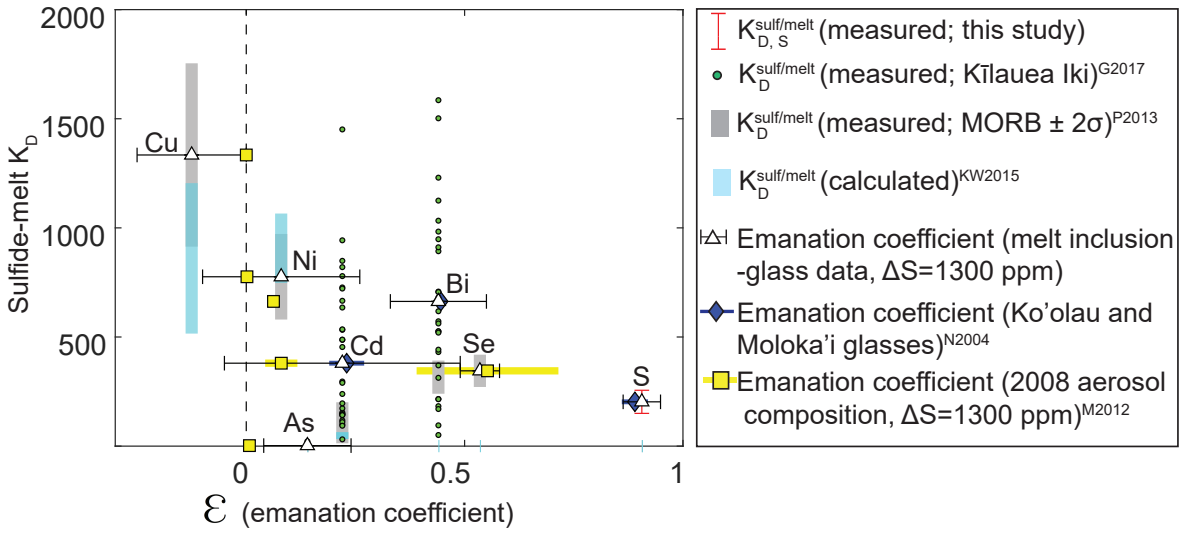

Figure 13: Comparison of emanation coefficients and sulfide-liquid partition coefficients. Emanation coefficients from this study (white triangles and error bars) were calculated from the regression line of each element versus S (see Fig. 3; Supplementary Fig. A13). Due to its compatible behaviour during PEC and fractionation, the emanation coefficient for Ni was calculated using a regression for uncorrected melt inclusion data. Emanation coefficients were calculated from X/S ratios from the 2008 plume (Mather et al., 2012), with the numerator ($[X]_i$-$[X]_f$) calculated from $\frac{X}{S} \times \Delta S_{degassed}$ and the denominator ($[X]_i$) calculated from $[X]_f + \frac{X}{S} \times \Delta S_{degassed}$ where $[X]_f$ is the average composition of the 1971 matrix glass (most similar in major element composition to the 2008 summit eruption), for ΔS=1300 ppm. Emanation coefficients from Norman et al. (2004) are also overlain. Measured sulfide-silicate partition coefficients from Kīlauea Iki lava lake samples are shown in green (Greaney et al., 2017). The range of measured partition coefficients for MORBs are shown with a grey bar (mean $\pm 2\sigma$; Patten et al., 2013). The light blue bar shows the range of partition coefficients calculated from Kiseeva and Wood (2015) for compositions with MgO contents between 6 and 14 wt% MgO (using the regressions shown in Fig. 11 to estimate the Ni and Cu composition in the sulfide, and the geothermometer of Helz and Thornber, 1987 to obtain T). The partition coefficient of S was calculated using the range of measured S concentrations in sulfides, assuming melt S contents of 1387–1600 ppm. There is no correlation between sulfide-liquid partition coefficients and emanation coefficients defined using petrology, or aerosol chemistry.

et al., 2002; Métrich et al., 1999; Savelyev et al., 2018). As Kīlauean liquids undergoing only olivine (+ minor chromite) fractionation have near-constant FeO contents (∼11.33 wt%), the extent of Fe-loss is inversely proportional to the measured FeO content of the melt inclusion. The absence of correlations between melt inclusion Ni, Cu and S concentrations and melt inclusion FeO contents (Supplementary Fig A14) suggests that the trajectories towards lower Ni and Cu contents do not result from sulfide saturation following Fe-loss. Even without extensive Fe-loss, PEC could drive sulfide saturation because of the crystallization of S-poor olivine, combined with a drop in the temperature of the melt. However, there is also no correlation between raw or corrected melt inclusion S, Cu and Ni contents and the amount of PEC calculated in Petrolog3. Finally, transmitted light observations reveal that only a very small proportion (∼5%) of melt inclusions contain sulfide blebs (Fig. 5e, letter "S" on Fig. 14). While some sulfides were inevitably lost during grinding to expose

the centre of each melt inclusion, this would only account for the loss of approximately half of the sulfides formed during PEC, which doesn't explain why the vast majority of inclusions with low Cu and Ni contents don't contain sulfides. Although a few of the inclusions containing sulfides have relatively low Cu and Ni contents, others plot near matrix glasses (inclusions marked with an "S" on Fig. 14**b)**, supporting our previous assertion that some sulfides within melt inclusions may have been co-entrapped.

An alternative explanation for the trajectory towards lower Ni and Cu contents is that olivine crystals grew and incorporated pockets of melt over a period in which sulfide liquids were progressively forming, and depleting the melt of Ni and Cu. In order to produce the higher Cu and Ni concentrations of matrix glasses compared with melt inclusions, the resorption of sulfides upon eruption must have released almost all of the Ni and Cu held within sulfide liquids back into the melt. If the Cu (and Ni) entered the gas phase directly, matrix glasses would plot with the most Cu and Ni depleted melt inclusions (Fig. 14a). The low emanation coefficients of Ni and Cu from aerosol measurements (0.15 and 0.01% respectively; Mather et al., 2012; Fig. 13) support a model in which sulfide-hosted Ni and Cu are released back into the melt during resorption of sulfides upon eruption (e.g., Fig 5), causing matrix glasses to follow a silicate-only fractionation trajectory. In contrast, melt inclusions would be isolated from this late-stage release of Ni and Cu, preserving the chemical trajectories of sulfide fraction prior to the onset of degassing. The fact that matrix glasses lie on a silicate-only fractionation trajectory has implications for the mechanism, and efficiency of sulfide mobilization upon eruption. The high density of sulfide droplets should result in their fractionation from the melt once they grow to a critical size. The involvement of sulfides in volcanic degassing has previously been attributed to the attachment of sulfide melts onto vapour bubbles, producing a compound drop with elevated buoyancy (Edmonds and Mather, 2017; Mungall et al., 2015). Interestingly, we also observe the attachment of sulfide globules onto the faces of olivine crystals (Fig. 5c). The remobilization of settled olivine crystals (Wieser et al., 2019; Wieser et al., 2020) upon eruption could provide an additional mechanism by which fractionated sulfides can participate in syn-eruptive degassing.

Chalcophile systematics in Lōi'hi glasses further support our assertion that the different trajectories defined by Cu, Ni and MgO in Kīlauea matrix glasses and melt inclusions are the result of sulfide fractionation, followed by sulfide resorption during low pressure degassing. Unlike Kīlauean glasses, Lōi'hi glasses show a positive correlation between Cu and MgO (Fig. 1c; R^2=0.44) and Cu and Ni (Fig. 14b; Supplementary Fig. A4; R^2=0.4), which is indicative of sulfide fractionation. The trajectory of these glasses in Ni vs. Cu space is remarkably similar to that defined by the 1971 melt inclusions (Fig. 14a). Furthermore, abundant sulfides (0.3–10% vol) have been reported in Lōi'hi xenoliths (Roedder, 1983), and we observe relatively abundant, spherical sulfides within Lōi'hi matrix glasses, providing strong textural evidence that Lōi'hi magmas were sulfide-saturated. Textural and chemical evidence

for sulfide saturation is preserved in Lōi‘hi matrix glasses due to the lack of syn-eruptive degassing of S in subaqueous eruptions; these samples provide a vital analogue for the evolution of sulfides within Kīlauean melts before the onset of syn-eruptive degassing.

The behaviour of Se allows further investigation of the relationship between sulfide resorption and chalcophile element degassing. In the previous section, the excellent correlation between S and Se (Fig. 3**b)**) was interpreted as concurrent degassing of these elements. However, the compound drop theory suggests that Se could be released directly from sulfides into the gas phase (Mungall et al., 2015). Thus, we entertain the possibility that the S-Se trajectory defined by melt inclusions and matrix glasses is recording the removal of Se and S from the melt into the sulfide phase, followed by direct transfer from the sulfide to the gas phase during sulfide resorption. The chemical trajectories associated with the removal of sulfides with 30 wt% S, and Se contents calculated from the likely range of $K_{D,\ Se}^{sulf/melt}$ (271 – 1012; Brenan, 2015; Patten et al., 2013) were modelled, and compared with the subset of melt inclusion and glasses with Se data. While sulfide removal with $K_{D,\ Se}^{sulf/melt}$=271 approximately recreates the observed trajectories, the low Se concentrations of matrix glasses require removal of >0.4 wt% sulfide (Fig. 14c). Removal of this quantity of sulfides is inconsistent with observed trends in Cu vs. S space for the same subset of melt inclusions and glasses (for $K_{D,\ Cu}^{sulf/melt}$=628–1754; Fig. 14d). Consequently, as the combined systematics of Cu, Se and S cannot be recreated by the removal of sulfide liquids, the excellent correlation of S and Se must result from syn-eruptive degassing from the silicate melt. This is further supported by the fact that Lōi‘hi glasses, which contain visible sulfides, still have Se concentrations plotting close to the least degassed melt inclusions at Kīlauea (Fig. 3b).

These observations provide new insights into the relative importance of vapour-sulfide, vapour-melt, and sulfide-melt partitioning in controlling the chalcophile element budget of volcanic plumes. We suggest that sulfide resorption releases chalcophile elements into the silicate melt-vapour system, with the partitioning between these two phases depending on element volatility 15d). This is best demonstrated by comparing the behaviour of Cu and Se. The spread of melt inclusion Ni and Cu contents relative to matrix glasses indicate that approximately 0.1% sulfide resorption may occur upon eruption (Fig. 14a-b). While resorption of ∼0.1 wt% sulfide leads to the release of relatively large quantities of Cu (∼50 ppm; Fig. 14a-**b)**,the high Cu contents of matrix glasses indicate that almost all of this Cu ends up back in the melt, because of the relatively low volatility of Cu in Kīlauean melts (X/S ratios measured in the 2008 Kīlauean plume indicate that only ∼0.01% of Cu degasses; Mather et al., 2012; Fig. 13). In contrast, even if all the Se released from the resorption of 0.1 wt% sulfide liquid entered the gas phase (∼0.08 ppm), a similar quantity of Se would also have to directly degass from the melt (Fig. 14c). Given that there is no evidence that sulfide-hosted Cu enters the gas phase directly, it seem likely that Se released from sulfides first enters the melt, then partitions along with S into the vapour phase (Fig. 14c).

Please cite the published version in GCA: Wieser et al., 2020,
https://doi.org/10.1016/j.gca.2020.05.018

Sulfide resorption upon eruption provides a significant, but previously unquantified flux of S to the atmosphere during Kīlauean eruptions. Resorption of 0.1 wt% sulfide corresponds to the release of 300 ppm of S (as measured sulfides contain ∼30 wt% S). This represents an additional source of error when using the "petrological method" in basaltic systems to quantify total S release (in addition to uncertainty in erupted lava volumes). This source of error can be circumvented if the Cu-Ni-S systematics of melt inclusions are carefully evaluated when choosing S concentrations to compare to co-erupted matrix glasses. The best constraint on the S release during eruptions is provided by melt inclusions with Cu concentrations overlapping those in co-erupted matrix glasses. In the 1971 summit eruption, these melt inclusions have PEC-corrected S concentrations between 1360 and 1425 ppm. Accounting for the incomplete degassing of basaltic melts (1971 matrix glasses have average S contents of 121 ppm), these measurements suggest that ∼1240–1300 ppm of S was released. In more primitive eruptions, melt inclusions with Ni and Cu systematics similar to matrix glasses have PEC-corrected S contents of ∼1600 ppm, so the S release upon eruption could reach 1465 ppm (accounting for the average glass S content of 135 ppm). SO_2 emissions at Kīlauea have been used to calculate lava effusion rates (Sutton et al., 2003; Sutton et al., 2001) using much lower estimates of S release from C/S ratios measured in volcanic gases (e.g., 861 ppm – Greenland, 1984; Greenland et al., 1988; 745 ppm – Sutton et al., 2003). Our significantly higher estimates of S release highlight the importance of detailed petrological work to accurately constrain lava effusion rates.

Please cite the published version in GCA: Wieser et al., 2020,
https://doi.org/10.1016/j.gca.2020.05.018

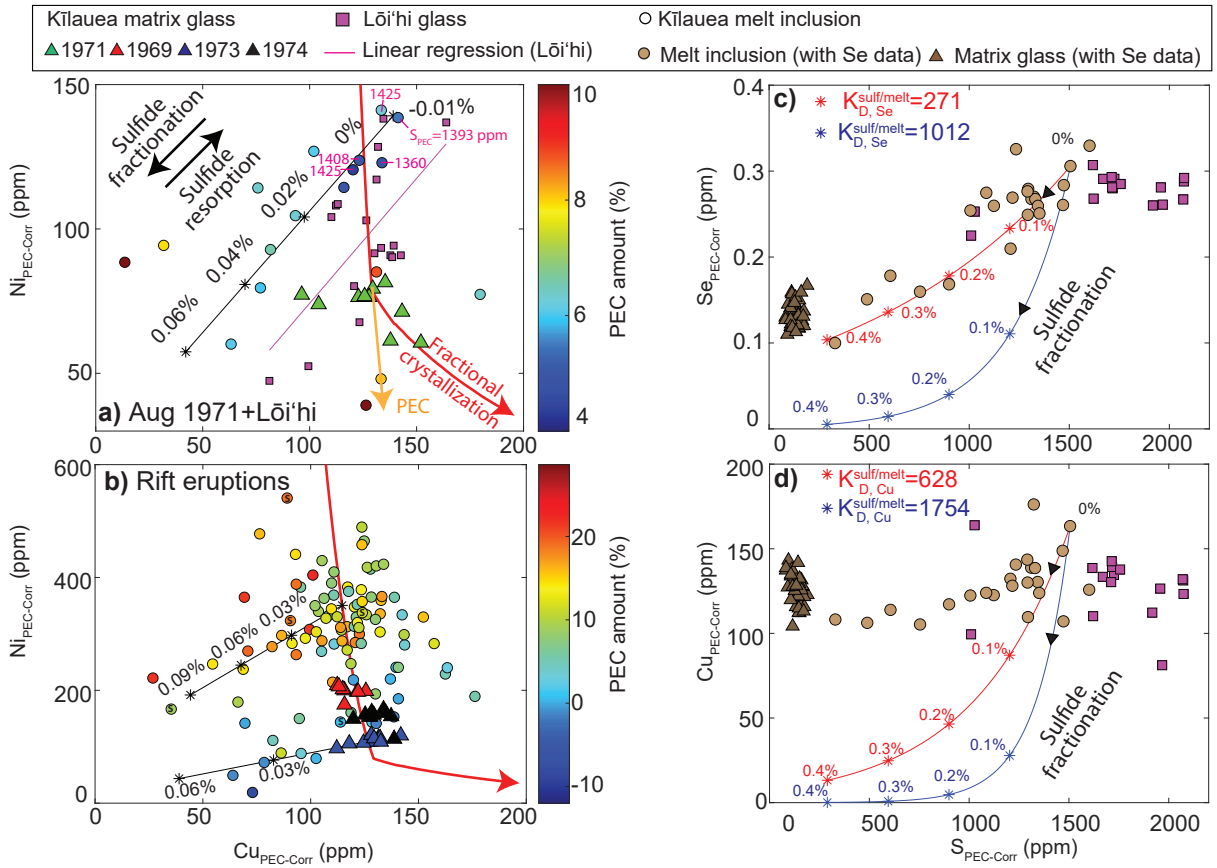

Figure 14: Differentiating sulfide resorption and degassing. **a)** Cu-Ni systematics for the 1971 summit eruption (where melt inclusions and carrier melts show a clear genetic relationship, Wieser et al., 2019). Matrix glasses largely plot along the sulfide-free fractional crystallization trajectory. Melt inclusion compositions corrected for post-entrapment crystallization follow two trajectories; that of silicate-only fractionation (red line), and decreasing Cu and Ni concentrations indicative of sulfide fractionation (black line). The black lines represent the removal of a sulfide composition calculated from the regression lines in Fig. 11 for MgO = 8.4 wt% (the mean PEC-corrected melt inclusion MgO content for this eruption). A linear regression through the composition of matrix glasses from Lōi'hi follows a remarkably similar trajectory (magenta line). **b)** Cu-Ni systematics for matrix glasses and melt inclusions from the three rift-zone eruptions are bracketed by fractional crystallization and sulfide fractionation trends (lower and upper sulfide removal trend for ∼7 and 12 wt% MgO). Melt inclusions containing a sulfide are marked with an "S". **c)** Models of the trajectory for sulfide fractionation in Se. vs. S space for different values of $K_{D,\ Se}^{sulf/melt}$. While sulfide fractionation for the lower limit of published estimates for the $K_{D,\ Se}^{sulf/melt}$ pass through melt inclusion data, fractionation of large quantities (∼0.4%) of sulfide are required to recreate the low Se concentrations of matrix glasses. **d)** Fractionation of this quantity of sulfides is inconsistent with observed Cu-S concentrations in the subset of matrix glass and melt inclusion compositions with Se data. The minimum value for $K_{D,\ Se}^{sulf/melt}$ (=271) is from Patten et al. (2013) - mean -2σ), and the maximum (=1012) is from the parametrization of Brenan (2015) for FeO=11.33 wt%. The maximum $K_{D,\ Cu}^{sulf/melt}$ (=1754) is from Patten et al., 2013 - mean +2σ), and the minimum (=628) was calculated from the parameterization of Kiseeva and Wood (2015) for the sulfide composition calculated from the regressions in Fig. 11 for 14 wt% MgO, and temperatures from Helz and Thornber, 1987.

Please cite the published version in GCA: Wieser et al., 2020,
https://doi.org/10.1016/j.gca.2020.05.018

5 Conclusions

Chalcophile element behaviour at Kīlauea Volcano, Hawai'i, is predominantly controlled by three separate stages of sulfide saturation, combined with the effects of sulfide resorption and degassing upon ascent to the site of eruption. The decoupled variability of chalcophile and lithophile elements during mantle melting in primitive samples (>6.8 wt% MgO) indicates that the concentrations of chalcophile elements in Kīlauea's mantle source are buffered by the presence of residual sulfides (Fig. 15a). These residual sulfides (and the possible presence of non-negligible proportions of S^{6+} species) are responsible for the high S contents of primary Kīlauean melts (1387–1600 ppm). The increase in sulfide solubility with decreasing pressures as melts ascend through the thick Hawaiian lithosphere results in crustal magma chambers being supplied with sulfide-undersaturated melts (Fig. 15b). The inclusion of sulfides within primitive olivine crystals, combined with models of sulfide solubility during fractional crystallization, indicates that a second stage of sulfide saturation within the crust occurs after relatively small amounts of crystal fractionation (∼12 wt% MgO; Fig. 15c).

Syn-eruptive degassing causes melt S contents to drop below the $SCSS_{Tot}$, driving the resorption of sulfides which are in contact with the degassing melt (Fig. 15d). This releases Cu, Ni, S and other chalcophile elements back into the vapour-melt-(sulfide) system. Elements with high vapour-melt partition coefficients enter the gas phase (e.g., S, Se), while elements with lower vapour-melt partition coefficients (e.g., Ni, Cu) predominantly remain in the melt. The resorption of sulfides, and the release of their chalcophile element budget back into the melts, obscures the textural and chemical record of sulfide saturation in matrix glasses. The coincidence of Cu-MgO and Cu-Ni systematics in matrix glasses with the trends predicted from sulfide-undersaturated fractionation demonstrates that the vast majority of immiscible sulfide liquids participated in the degassing process; perhaps due to their attachment to buoyant vapour bubbles, or remobilized olivine crystals. Fortunately, the chalcophile element systematics within melt inclusion populations (which are isolated from the late stage release of chalcophile elements into the melt), along with the preservation of visible sulfides within olivine crystals and undegassed embayments, faithfully record the fractionation of sulfides.

Previous studies investigating chalcophile element systematics have focused on lava lakes, formed through the ponding and fractionation of degassing melt within pre-existing pit craters. This has led to suggestions that sulfide saturation at Kīlauea only occurs after significant amounts of crystal fractionation (∼2 wt% MgO). We demonstrate that the loss of S to the gas phase upon eruption resulted in previously sulfide-saturated magmas becoming sulfide undersaturated once more. Due to their low S contents, these melts reach a third phase of sulfide saturation following significant amounts of cooling and fractionation. This phase is unique to the fractionation path taken by degassed melts, and is not representative of the evolution of undegassed melts in crustal magma chambers (Fig. 15d).

Please cite the published version in GCA: Wieser et al., 2020,
https://doi.org/10.1016/j.gca.2020.05.018

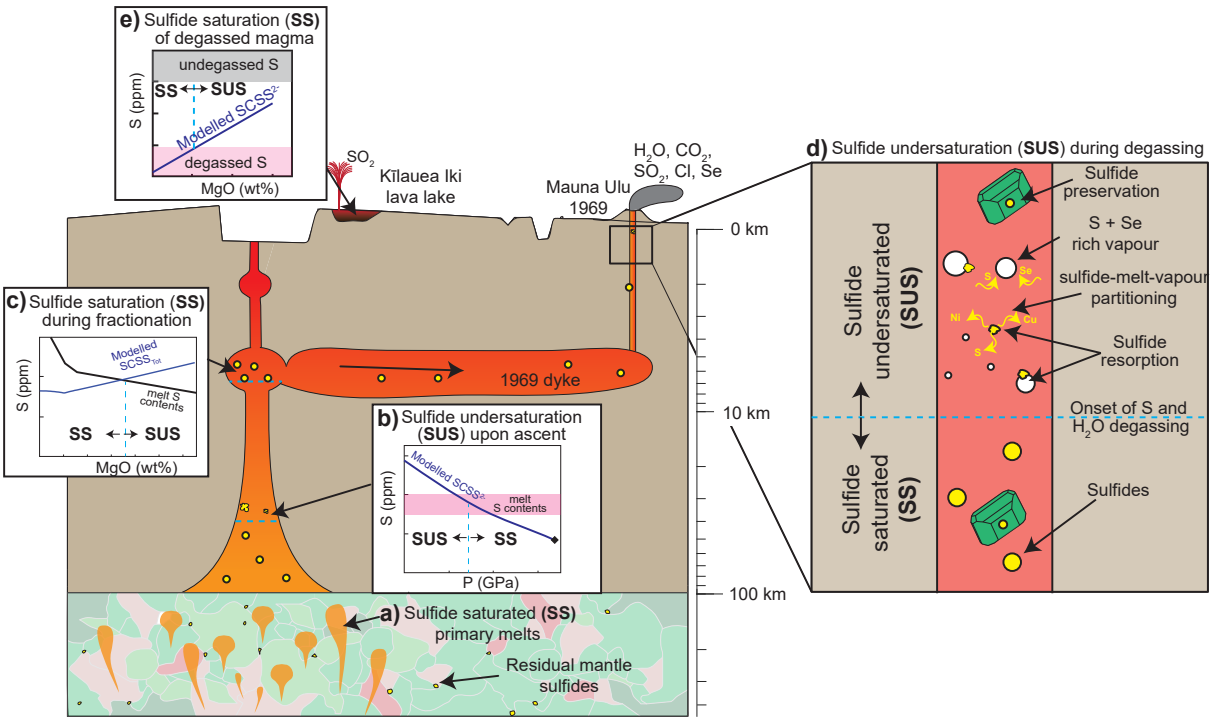

Figure 15: Summary diagram of processes affecting chalcophile element concentrations at Kīlauea. **a)** Residual sulfides are present in the mantle source throughout the melting interval of the eruptions analysed in this study (F=∼0.05–0.1), buffering the concentrations of chalcophile elements relative to lithophile elements during changes in melt extent. The presence of residual sulfides accounts for the high S contents of primary melts (1387–1600 ppm). **b)** Upon ascent through the thick Hawaiian lithosphere, the increase in the SCSS2- with decreasing pressure results in melts becoming sulfide undersaturated (SUS). c) During fractionation in crustal magma chambers, decreasing temperatures, major element changes, and an increase in melt S contents during crystal fractionation drives the melts towards sulfide saturation once more (∼12 wt% MgO). **d)** At low pressures as magma ascends towards the site of eruption, S partitions strongly into a vapour phase. This causes sulfides to resorb, releasing their chalcophile element load (S, Ni, Cu, Se etc.) back into the melt. These elements then partition between the melt and vapour phase, resulting in volatile elements such as S and Se mostly partitioning in the gas phase, and more refractory elements such as Ni and Cu remaining in the melt. **e)** The lava filling the Kīlauea Iki lava lake was S-poor (and therefore sulfur undersaturated) due to extensive degassing upon eruption. Extensive amounts of cooling and fractionation were required to reach sulfide saturation from such a S-poor melt.

5.1 Author Contributions

PW prepared and analysed the Kīlauean melt inclusions, glasses and sulfides by EPMA and EDS. PW performed LA-ICP-MS analyses under the guidance of FJ and BK. FJ analysed the Lōi'hi glasses. PW interpreted the data and wrote the manuscript with help from all authors.

Please cite the published version in GCA: Wieser et al., 2020,
https://doi.org/10.1016/j.gca.2020.05.018

5.2 Research Data

The melt inclusion and glass chalcophile element compositions used in this study are provided as an excel spreadsheet in Appendix B, along with information on standards run in each session. A Jupyter notebook of the mantle melting models used in this study, along with Appendix B, has been uploaded to GitHub (`https://github.com/PennyWieser/Sulfide_Present_Melting_GCA_Wieser2020`)

5.3 Acknowledgements

We thank Callum Reekie and Duane Smythe for helpful discussions about sulfide saturation. We thank Hugh O'Neill for his comments regarding the importance of S^{6+} corrections, and re-interpretation of literature XANES data. We thank Giulio Lampronti and Iris Buisman for help collecting EDS and EPMA data; John Craven and Sally Gibson for providing sulfide standards, and Michael Garcia and Aaron Pietruszka for supplying the Lōi'hi samples. Isobel Sides (funded by a Natural Environment Research Council [NERC] studentship) and Don Swanson (U.S. Geological Survey) collected the Kīlauean samples used in this study. Nick Barber is thanked for his comments and help making the Juptyer notebook released with this study as user-friendly as possible. PW is funded by NERC DTP studentship NE/L002507/1. BK is funded by NERC grant 'From Arc Magmas to Ore Systems (FAMOS): a Mineral Systems Approach (NE/P017045/1). FJ acknowledges technique development funding from the NERC grant 'Mantle volatiles: processes, reservoirs and fluxes (NE/M000427/1). The authors thank Paul Wallace, Clifford Patten, and Yuan Li for helpful reviewers which substantially increased the clarity of the manuscript.

Works Cited

Beattie, P., Ford, C., and Russell, D. (1991). Partition coefficients for olivine-melt and orthopyroxene-melt systems. *Contributions to Mineralogy and Petrology*, **109**, pp. 212–224.

Bennett, V., Norman, M., and Garcia, M. (2000). Rhenium and platinum group element abundances correlated with mantle source components in Hawaiian picrites: sulphides in the plume. *Earth and Planetary Science Letters*, **183**, pp. 513–526.

Berlo, K. et al. (2014). Sulfide breakdown controls metal signature in volcanic gas at Kawah Ijen volcano, Indonesia. *Chemical Geology*, **371**, pp. 115–127.

Berry, A. J. et al. (2018). A re-assessment of the oxidation state of iron in MORB glasses. *Earth and Planetary Science Letters*, **483**, pp. 114–123.

Bougault, H. and Hekinian, R. (1974). Rift valley in the Atlantic Ocean near 36° 50 N: petrology and geochemistry of basaltic rocks. *Earth and Planetary Science Letters*, **24**, pp. 249–261.

Brenan, J. M. (2015). Se–Te fractionation by sulfide–silicate melt partitioning: implications for the composition of mantle-derived magmas and their melting residues. *Earth and Planetary Science Letters*, **422**, pp. 45–57.

Brounce, M., Stolper, E., and Eiler, J. (2017). Redox variations in Mauna Kea lavas, the oxygen fugacity of the Hawaiian plume, and the role of volcanic gases in Earth's oxygenation. *Proceedings of the National Academy of Sciences*, **114**, pp. 8997–9002.

Bulanova, G. et al. (1996). Trace elements in sulfide inclusions from Yakutian diamonds. *Contributions to Mineralogy and Petrology*, **124**, pp. 111–125.

Carmichael, I. S. and Ghiorso, M. S. (1986). Oxidation-reduction relations in basic magma: a case for homogeneous equilibria. *Earth and Planetary Science Letters*, **78**, pp. 200–210.

Cervelli, P. F. and Miklius, A. (2003). The shallow magmatic system of Kilauea Volcano. *US Geological Survey Professional Paper*, **1676**, pp. 149–163.

Clague, D., Weber, W. S., and Dixon, J. E. (1991). Picritic glasses from Hawaii. *Nature*, **353**, p. 553.

Cottrell, E. and Kelley, K. A. (2011). The oxidation state of Fe in MORB glasses and the oxygen fugacity of the upper mantle. *Earth and Planetary Science Letters*, **305**, pp. 270–282.

Cottrell, E. et al. (2009). High-precision determination of iron oxidation state in silicate glasses using XANES. *Chemical Geology*, **268**, pp. 167–179.

Cox, D. et al. (2019). Chalcophile element processing beneath a continental arc stratovolcano. *Earth and Planetary Science Letters*, **522**, pp. 1–11.

Crowe, B. M. et al. (1987). Trace element geochemistry of volcanic gases and particles from 1983–1984 eruptive episodes of Kilauea volcano. *Journal of Geophysical Research: Solid Earth*, **92**, pp. 13708–13714.

Czamanske, G. K. and Moore, J. G. (1977). Composition and phase chemistry of sulfide globules in basalt from the Mid-Atlantic Ridge rift valley near 37 N lat. *Geological Society of America Bulletin*, **88**, pp. 587–599.

Danyushevsky, L. V. (2001). The effect of small amounts of H_2O on crystallisation of mid-ocean ridge and backarc basin magmas. *Journal of Volcanology and Geothermal Research*, **110**, pp. 265–280.

Danyushevsky, L. V., McNeill, A. W., and Sobolev, A. V. (2002). Experimental and petrological studies of melt inclusions in phenocrysts from mantle-derived magmas: an overview of techniques, advantages and complications. *Chemical Geology*, **183**, pp. 5–24.

Danyushevsky, L. V. and Plechov, P. (2011). Petrolog3: Integrated software for modeling crystallization processes. *Geochemistry, Geophysics, Geosystems*, **12**.

Desborough, G. A., Anderson, A. T., and Wright, T. L. (1968). Mineralogy of sulfides from certain Hawaiian basalts. *Economic Geology*, **63**, pp. 636–644.

Ding, S. and Dasgupta, R. (2018). Sulfur inventory of ocean island basalt source regions constrained by modeling the fate of sulfide during decompression melting of a heterogeneous mantle. *Journal of Petrology*, **59**, pp. 1281–1308.

Dixon, J. E., Clague, D. A., and Stolper, E. M. (1991). Degassing history of water, sulfur, and carbon in submarine lavas from Kilauea Volcano, Hawaii. *The Journal of Geology*, **99**, pp. 371–394.

Dixon, J. E. et al. (1997). Volatiles in alkalic basalts form the North Arch Volcanic Field, Hawaii: extensive degassing of deep submarine-erupted alkalic series lavas. *Journal of Petrology*, **38**, pp. 911–939.

Edmonds, M., Gerlach, T. M., and Herd, R. A. (2009). Halogen degassing during ascent and eruption of water-poor basaltic magma. *Chemical Geology*, **263**, pp. 122–130.

Edmonds, M. and Mather, T. A. (2017). Volcanic sulfides and outgassing. *Elements*, **13**, pp. 105–110.

Edmonds, M., Mather, T. A., and Liu, E. J. (2018). A distinct metal fingerprint in arc volcanic emissions. *Nature Geoscience*, **11**, pp. 790–794.

Fleet, M. E. and Stone, W. E. (1990). Nickeliferous sulfides in xenoliths, olivine megacrysts and basaltic glass. *Contributions to Mineralogy and Petrology*, **105**, pp. 629–636.

Fortin, M.-A. et al. (2015). The effect of water on the sulfur concentration at sulfide saturation (SCSS) in natural melts. *Geochimica et Cosmochimica Acta*, **160**, pp. 100–116.

Garcia, M. O. et al. (1993). An evaluation of temporal geochemical evolution of Loihi summit lavas: results from Alvin submersible dives. *Journal of Geophysical Research: Solid Earth*, **98**, pp. 537–550.

Garcia, M. O. et al. (1998). Petrology and geochronology of basalt breccia from the 1996 earthquake swarm of Loihi seamount, Hawaii: magmatic history of its 1996 eruption. *Bulletin of Volcanology*, **59**, pp. 577–592.

Gerlach, T. M. and Nordlie, B. E. (1975). The COHS gaseous system; Part I, Composition limits and trends in basaltic cases. *American Journal of Science*, **275**, pp. 353–376.

Ghiorso, M. S. et al. (2002). The pMELTS: A revision of MELTS for improved calculation of phase relations and major element partitioning related to partial melting of the mantle to 3 GPa. *Geochemistry, Geophysics, Geosystems*, **3**, pp. 1–35.

Greaney, A. T. et al. (2017). The behavior of chalcophile elements during magmatic differentiation as observed in Kilauea Iki lava lake, Hawaii. *Geochimica et Cosmochimica Acta*, **210**, pp. 71–96.

Greenland, L. (1984). Gas composition of the January 1983 eruption of Kilauea Volcano, Hawaii. *Geochimica et Cosmochimica Acta*, **48**, pp. 193–195.

Greenland, L., Okamura, A., and Stokes, J. (1988). Constraints on the mechanism of eruption, in: The Pu'u O' O Eruption of Kilauea Volcano, Hawai'i: Episodes 1 through 20. *US Geological Survey Professional Paper 1463*, pp. 155–164.

Guo, J., Griffin, W. L., and O'Reilly, S. Y. (1999). Geochemistry and origin of sulphide minerals in mantle xenoliths: Qilin, Southeastern China. *Journal of Petrology*, **40**, pp. 1125–1149.

Hartley, M. E. et al. (2017). Olivine-hosted melt inclusions as an archive of redox heterogeneity in magmatic systems. *Earth and Planetary Science Letters*, **479**, pp. 192–205.

Helmy, H. M. and Fonseca, R. O. (2017). The behavior of Pt, Pd, Cu and Ni in the Se-sulfide system between 1050 and 700° C and the role of Se in platinum-group elements fractionation in sulfide melts. *Geochimica et Cosmochimica Acta*, **216**, pp. 141–152.

Helz, R. T. (1987). Diverse olivine types in lava of the 1959 eruption of Kilauea volcano and their bearing on eruption dynamics. *Volcanism in Hawaii*, **1**, pp. 691–722.

Please cite the published version in GCA: Wieser et al., 2020,
https://doi.org/10.1016/j.gca.2020.05.018

Helz, R. T. and Thornber, C. R. (1987). Geothermometry of Kilauea Iki lava lake, Hawaii. *Bulletin of volcanology*, **49**, pp. 651–668.

Helz, R. T. and Wright, T. L. (1992). Differentiation and magma mixing on Kilauea's east rift zone. *Bulletin of Volcanology*, **54**, pp. 361–384.

Helz, R. T. and Wright, T. L. (1983). Drilling report and core logs for the 1981 drilling of Kilauea Iki lava lake, Kilauea volcano, Hawaii, with comparative notes on earlier (1967-1979) drilling experiences. *Open-File Report 83-326, United States Geological Survey*, pp. 1–68.

Helz, R. et al. (2017). Olivine-melt relationships and syneruptive redox variations in the 1959 eruption of Kılauea Volcano as revealed by XANES. *Journal of Volcanology and Geothermal Research*, **333**, pp. 1–14.

Hofmann, A. W. (1997). Mantle geochemistry: the message from oceanic volcanism. *Nature*, **385**, pp. 219–229.

Hofmann, A. W., Feigenson, M. D., and Raczek, I. (1984). Case studies on the origin of basalt: III. Petrogenesis of the Mauna Ulu eruption, Kilauea, 1969–1971. *Contributions to Mineralogy and Petrology*, **88**, pp. 24–35.

Jenner, F. E. and Arevalo Jr, R. D. (2016). Major and trace element analysis of natural and experimental igneous systems using LA–ICP–MS. *Elements*, **12**, pp. 311–316.

Jenner, F. E. and O'Neill, H. S. C. (2012a). Analysis of 60 elements in 616 ocean floor basaltic glasses. *Geochemistry, Geophysics, Geosystems*, **13**.

Jenner, F. E. and O'Neill, H. S. C. (2012b). Major and trace analysis of basaltic glasses by laser-ablation ICP-MS. *Geochemistry, Geophysics, Geosystems*, **13**.

Jenner, F. E. (2017). Cumulate causes for the low contents of sulfide-loving elements in the continental crust. *Nature Geoscience*, **10**, pp. 524–529.

Jenner, F. E. et al. (2012). Chalcophile element systematics in volcanic glasses from the northwestern Lau Basin. *Geochemistry, Geophysics, Geosystems*, **13**.

Jenner, F. E. et al. (2009). Determination of selenium concentrations in NIST SRM 610, 612, 614 and geological glass reference materials using the electron probe, LA-ICP-MS and SHRIMP II. *Geostandards and Geoanalytical Research*, **33**, pp. 309–317.

Jenner, F. E. et al. (2010). The magnetite crisis in the evolution of arc-related magmas and the initial concentration of Au, Ag and Cu. *Journal of Petrology*, **51**, pp. 2445–2464.

Jenner, F. E. et al. (2015). The competing effects of sulfide saturation versus degassing on the behavior of the chalcophile elements during the differentiation of hydrous melts. *Geochemistry, Geophysics, Geosystems*, **16**, pp. 1490–1507.

Jochum, K. P. et al. (2006). MPI-DING reference glasses for in situ microanalysis: New reference values for element concentrations and isotope ratios. *Geochemistry, Geophysics, Geosystems*, **7**.

Jochum, K. and Hofmann, A. (1997). Constraints on earth evolution from antimony in mantle-derived rocks. *Chemical geology*, **139**, pp. 39–49.

Jugo, P. J., Luth, R. W., and Richards, J. P. (2005). An experimental study of the sulfur content in basaltic melts saturated with immiscible sulfide or sulfate liquids at 1300° C and 1 · 0 GPa. *Journal of Petrology*, **46**, pp. 783–798.

Jugo, P. J., Wilke, M., and Botcharnikov, R. E. (2010). Sulfur K-edge XANES analysis of natural and synthetic basaltic glasses: Implications for S speciation and S content as function of oxygen fugacity. *Geochimica et Cosmochimica Acta*, **74**, pp. 5926–5938.

Kelley, K. A., Kingsley, R., and Schilling, J.-G. (2013). Composition of plume-influenced mid-ocean ridge lavas and glasses from the Mid-Atlantic Ridge, East Pacific Rise, Galápagos Spreading Center, and Gulf of Aden. *Geochemistry, Geophysics, Geosystems*, **14**, pp. 223–242.

Kiseeva, E. S., Fonseca, R. O., and Smythe, D. J. (2017). Chalcophile elements and sulfides in the upper mantle. *Elements*, **13**, pp. 111–116.

Please cite the published version in GCA: Wieser et al., 2020,
https://doi.org/10.1016/j.gca.2020.05.018

Kiseeva, E. S. and Wood, B. J. (2015). The effects of composition and temperature on chalcophile and lithophile element partitioning into magmatic sulphides. *Earth and Planetary Science Letters*, **424**, pp. 280–294.

Lambart, S., Baker, M. B., and Stolper, E. M. (2016). The role of pyroxenite in basalt genesis: Melt-PX, a melting parameterization for mantle pyroxenites between 0.9 and 5 GPa. *Journal of Geophysical Research: Solid Earth*, **121**, pp. 5708–5735.

Lambert, G. et al. (1985). Volcanic emission of radionuclides and magma dynamics. *Earth and Planetary Science Letters*, **76**, pp. 185–192.

Lee, C.-T. A. et al. (2012). Copper systematics in arc magmas and implications for crust-mantle differentiation. *Science*, **336**, pp. 64–68.

Li, C. and Ripley, E. M. (2005). Empirical equations to predict the sulfur content of mafic magmas at sulfide saturation and applications to magmatic sulfide deposits. *Mineralium Deposita*, **40**, pp. 218–230.

Li, C. and Ripley, E. M. (2009). Sulfur contents at sulfide-liquid or anhydrite saturation in silicate melts: empirical equations and example applications. *Economic Geology*, **104**, pp. 405–412.

Li, X. et al. (2004). Rejuvenation of the lithosphere by the Hawaiian plume. *Nature*, **427**, pp. 827–829.

Li, Y. and Audétat, A. (2015). Effects of temperature, silicate melt composition, and oxygen fugacity on the partitioning of V, Mn, Co, Ni, Cu, Zn, As, Mo, Ag, Sn, Sb, W, Au, Pb, and Bi between sulfide phases and silicate melt. *Geochimica et Cosmochimica Acta*, **162**, pp. 25–45.

Liu, X. et al. (2014). Partitioning of copper between olivine, orthopyroxene, clinopyroxene, spinel, garnet and silicate melts at upper mantle conditions. *Geochimica et Cosmochimica Acta*, **125**, pp. 1–22.

Loewen, M. W. (2013). Volatile mobility of trace metals in volcanic systems. *PhD thesis, Oregon State University, Corvallis.*

Longo, B. M. et al. (2010). Acute health effects associated with exposure to volcanic air pollution (vog) from increased activity at Kilauea Volcano in 2008. *Journal of Toxicology and Environmental Health, Part A*, **73**, pp. 1370–1381.

Maaløe, S. and Hansen, B. (1982). Olivine phenocrysts of Hawaiian olivine tholeiite and oceanite. *Contributions to Mineralogy and Petrology*, **81**, pp. 203–211.

Mather, T. et al. (2012). Halogens and trace metal emissions from the ongoing 2008 summit eruption of Kılauea volcano, Hawaii. *Geochimica et Cosmochimica Acta*, **83**, pp. 292–323.

Matjuschkin, V., Blundy, J. D., and Brooker, R. A. (2016). The effect of pressure on sulphur speciation in mid-to deep-crustal arc magmas and implications for the formation of porphyry copper deposits. *Contributions to Mineralogy and Petrology*, **171**, p. 66.

Matthews, S., Shorttle, O., and Maclennan, J. (2016). The temperature of the I celandic mantle from olivine-spinel aluminum exchange thermometry. *Geochemistry, Geophysics, Geosystems*, **17**, pp. 4725–4752.

Mavrogenes, J. A. and O'Neill, H. S. C. (1999). The relative effects of pressure, temperature and oxygen fugacity on the solubility of sulfide in mafic magmas. *Geochimica et Cosmochimica Acta*, **63**, pp. 1173–1180.

Métrich, N. and Mandeville, C. W. (2010). Sulfur in magmas. *Elements*, **6**, pp. 81–86.

Métrich, N. et al. (1999). Transfer of sulfur in subduction settings: an example from Batan Island (Luzon volcanic arc, Philippines). *Earth and Planetary Science Letters*, **167**, pp. 1–14.

Moore, R. B. et al. (1980). The 1977 eruption of Kilauea volcano, Hawaii. *Journal of Volcanology and Geothermal Research*, **7**, pp. 189–210.

Moussallam, Y. et al. (2016). The impact of degassing on the oxidation state of basaltic magmas: a case study of Kılauea volcano. *Earth and Planetary Science Letters*, **450**, pp. 317–325.

Moussallam, Y. et al. (2019). Mantle plumes are oxidised. *Earth and Planetary Science Letters*, **527**, p. 115798.

Mungall, J. E. et al. (2015). Transport of metals and sulphur in magmas by flotation of sulphide melt on vapour bubbles. *Nature Geoscience*, **8**, pp. 216–219.

Mysen, B. (1978). Experimental determination of nickel partition coefficients between liquid, pargasite, and garnet peridotite minerals and concentration limits of behavior according to Henry's law at high pressure and temperature. *American Journal of Science*, **278**, pp. 217–243.

Nadeau, O., Williams-Jones, A. E., and Stix, J. (2010). Sulphide magma as a source of metals in arc-related magmatic hydrothermal ore fluids. *Nature Geoscience*, **3**, pp. 501–505.

Nash, W. M., Smythe, D. J., and Wood, B. J. (2019). Compositional and temperature effects on sulfur speciation and solubility in silicate melts. *Earth and Planetary Science Letters*, **507**, pp. 187–198.

Neal, C. et al. (2019). The 2018 rift eruption and summit collapse of Kılauea Volcano. *Science*, **363**, pp. 367–374.

Nelson, S. and Sewake, K. (2008). Volcanic emissions injury to plant foliage. *Plant Disease*, **47**.

Newsom, H. et al. (1986). Siderophile and chalcophile element abundances in oceanic basalts, Pb isotope evolution and growth of the Earth's core. *Earth and Planetary Science Letters*, **80**, pp. 299–313.

Norman, M. D., Garcia, M. O., and Bennett, V. C. (2004). Rhenium and chalcophile elements in basaltic glasses from Ko'olau and Moloka'i volcanoes: Magmatic outgassing and composition of the Hawaiian plume. *Geochimica et Cosmochimica Acta*, **68**, pp. 3761–3777.

Norman, M. D. et al. (2002). Olivine-hosted melt inclusions in Hawaiian picrites: equilibration, melting, and plume source characteristics. *Chemical Geology*, **183**, pp. 143–168.

O'Neill, H. (2020). Hughs SCSS paper in prep. *AGU*, **183**, pp. 143–168.

Palme, H. and O'Neill, H. (2014). Cosmochemical estimates of mantle composition. *Treatise on Geochemistry. Oxford: Elsevier-Pergamon*, pp. 1–39.

Patten, C., Barnes, S.-J., and Mathez, E. A. (2012). Textural variations in MORB sulfide droplets due to differences in crystallization history. *The Canadian Mineralogist*, **50**, pp. 675–692.

Patten, C. et al. (2013). Partition coefficients of chalcophile elements between sulfide and silicate melts and the early crystallization history of sulfide liquid: LA-ICP-MS analysis of MORB sulfide droplets. *Chemical Geology*, **358**, pp. 170–188.

Pearson, D. et al. (1998). Sulphide inclusions in diamonds from the Koffiefontein kimberlite, S Africa: constraints on diamond ages and mantle Re–Os systematics. *Earth and Planetary Science Letters*, **160**, pp. 311–326.

Peck, D. L. (1978). Cooling and vesiculation of Alae lava lake, Hawaii. *US Geological Survey Professional Paper*, **935A**, A1–A33.

Pietruszka, A. J. and Garcia, M. O. (1999). A rapid fluctuation in the mantle source and melting history of Kilauea Volcano inferred from the geochemistry of its historical summit lavas (1790–1982). *Journal of Petrology*, **40**, pp. 1321–1342.

Pietruszka, A. J. et al. (2011). Excesses of seawater-derived 234U in volcanic glasses from Loihi Seamount due to crustal contamination. *Earth and Planetary Science Letters*, **304**, pp. 280–289.

Pietruszka, A. J. et al. (2018). An Isotopic Perspective into the Magmatic Evolution and Architecture of the Rift Zones of Kılauea Volcano. *Journal of Petrology*, **59**, pp. 2311–2352.

Pitcher, L. et al. (2009). Fractionation of the platinum-group elments and Re during crystallization of basalt in Kilauea Iki Lava Lake, Hawaii. *Chemical Geology*, **260**, pp. 196–210.

Poland, M. P., Miklius, A., Montgomery-Brown, E. K., et al. (2014). "Magma supply, storage, and transport at shield-stage Hawaiian volcanoes". In: *Characteristics of Hawaiian volcanoes*. Vol. 1801. US Geological Survey, pp. 179–234.

Putirka, K. D. (2008). Thermometers and barometers for volcanic systems. *Reviews in mineralogy and geochemistry*, **69**, pp. 61–120.

Please cite the published version in GCA: Wieser et al., 2020,
https://doi.org/10.1016/j.gca.2020.05.018

Putirka, K. D. (2017). Down the crater: where magmas are stored and why they erupt. *Elements*, **13**, pp. 11–16.

Reekie, C. et al. (2019). Sulfide resorption during crustal ascent and degassing of oceanic plateau basalts. *Nature communications*, **10**, pp. 1–11.

Richardson, S. et al. (2001). Archean subduction recorded by Re–Os isotopes in eclogitic sulfide inclusions in Kimberley diamonds. *Earth and Planetary Science Letters*, **191**, pp. 257–266.

Robock, A. (2000). Volcanic eruptions and climate. *Reviews of geophysics*, **38**, pp. 191–219.

Roedder, E. (1983). Geobarometry of ultramafic xenoliths from Loihi Seamount, Hawaii, on the basis of CO_2 inclusions in olivine. *Earth and Planetary Science Letters*, **66**, pp. 369–379.

Saal, A. E. et al. (2002). Vapour undersaturation in primitive mid-ocean-ridge basalt and the volatile content of Earth's upper mantle. *Nature*, **419**, pp. 451–455.

Savelyev, D. P. et al. (2018). Immiscible sulfide melts in primitive oceanic magmas: Evidence and implications from picrite lavas (Eastern Kamchatka, Russia). *American Mineralogist*, **103**, pp. 886–898.

Sides, I. et al. (2014a). Eruption style at Kılauea Volcano in Hawai 'i linked to primary melt composition. *Nature Geoscience*, **7**, p. 464.

Sides, I. et al. (2014b). Magma mixing and high fountaining during the 1959 Kılauea Iki eruption, Hawai 'i. *Earth and Planetary Science Letters*, **400**, pp. 102–112.

Sisson, T. (2003). Native gold in a Hawaiian alkalic magma. *Economic Geology*, **98**, pp. 643–648.

Skinner, B. J. and Peck, D. L. (1969). An immiscible sulfide melts from Hawaii. *Econ. Geol. Monogr.*, **4**, pp. 310–322.

Smythe, D. J., Wood, B. J., and Kiseeva, E. S. (2017). The S content of silicate melts at sulfide saturation: new experiments and a model incorporating the effects of sulfide composition. *American Mineralogist*, **102**, pp. 795–803.

Stone, W. E. and Fleet, M. E. (1991). Nickel-copper sulfides from the 1959 eruption of Kilauea Volcano, Hawaii: Contrasting compositions and phase relations in eruption pumice and Kilauea Iki lava lake. *American Mineralogist*, **76**, pp. 1363–1372.

Sutton, A. J., Elias, T., and Kauahikaua, J. (2003). Lava-effusion rates for the Pu'u'O'o–Kupaianaha eruption derived from SO2 emissions and very low frequency (VLF) measurements. *US Geol Surv Prof Pap*, **1676**, pp. 137–148.

Sutton, A. et al. (2001). Implications for eruptive processes as indicated by sulfur dioxide emissions from Kılauea Volcano, Hawai 'i, 1979–1997. *Journal of Volcanology and Geothermal Research*, **108**, pp. 283–302.

Swanson, D. A. et al. (1979). Chronological narrative of the 1969-71 Mauna Ulu eruption of Kilauea Volcano, Hawaii.

Tam, E. et al. (2016). Volcanic air pollution over the Island of Hawai'i: Emissions, dispersal, and composition. Association with respiratory symptoms and lung function in Hawai'i Island school children. *Environment international*, **92**, pp. 543–552.

Tatsumi, Y., Oguri, K., and Shimoda, G. (1999). The behaviour of platinum-group elements during magmatic differentiation in Hawaiian tholeiites. *Geochemical Journal*, **33**, pp. 237–247.

Thornber, C. R. et al. (2015). Petrologic testament to changes in shallow magma storage and transport during 30+ years of recharge and eruption at Kılauea Volcano, Hawai 'i. *Hawaiian Volcanoes: From Source to Surface*, **208**, p. 147.

Tuohy, R. M. et al. (2016). Magma transport and olivine crystallization depths in Kılauea's east rift zone inferred from experimentally rehomogenized melt inclusions. *Geochimica et Cosmochimica Acta*, **185**, pp. 232–250.

Wallace, P. J. and Anderson, A. T. (1998). Effects of eruption and lava drainback on the H 2 O contents of basaltic magmas at Kilauea Volcano. *Bulletin of volcanology*, **59**, pp. 327–344.

Please cite the published version in GCA: Wieser et al., 2020,
https://doi.org/10.1016/j.gca.2020.05.018

Wallace, P. J. and Carmichael, I. S. (1994). S speciation in submarine basaltic glasses as determined by measurements of S Kα X-ray wavelength shifts. *American Mineralogist*, **79**, pp. 161–167.

Westerlund, K. et al. (2006). A subduction wedge origin for Paleoarchean peridotitic diamonds and harzburgites from the Panda kimberlite, Slave craton: evidence from Re–Os isotope systematics. *Contributions to Mineralogy and Petrology*, **152**, p. 275.

Whitty, R. C. et al. (2020). Spatial and Temporal Variations in SO 2 and PM 2.5 Levels Around Kılauea Volcano, Hawai'i During 2007–2018. *Frontiers in Earth Sciences*, **8**, p. 36.

Wieser, P. E. et al. (2019). Crystal scavenging from mush piles recorded by melt inclusions. *Nature Communications*, **10**, pp. 1–11.

Wieser, P. E. et al. (2020). Microstructural constraints on magmatic mushes under Kılauea Volcano, Hawaii. *Nature Communications*, **11**, pp. 1–14.

Witham, C. S. and Oppenheimer, C. (2004). Mortality in England during the 1783–4 Laki Craters eruption. *Bulletin of Volcanology*, **67**, pp. 15–26.

Witt-Eickschen, G. et al. (2009). The geochemistry of the volatile trace elements As, Cd, Ga, In and Sn in the Earth's mantle: New evidence from in situ analyses of mantle xenoliths. *Geochimica et Cosmochimica Acta*, **73**, pp. 1755–1778.

Wölbern, I. et al. (2006). Deep origin of the Hawaiian tilted plume conduit derived from receiver functions. *Geophysical Journal International*, **166**, pp. 767–781.

Wright, T. L. and Fiske, R. S. (1971). Origin of the differentiated and hybrid lavas of Kilauea volcano, Hawaii. *Journal of Petrology*, **12**, pp. 1–65.

Wright, T. L., Peck, D. L., and Shaw, H. R. (1976). Kilauea lava lakes: natural laboratories for study of cooling, crystallization, and differentiation of basaltic magma. *The geophysics of the Pacific Ocean basin and its margin*, **19**, pp. 375–390.

Wulf, A., Palme, H., and Jochum, K. (1995). Fractionation of volatile elements in the early solar system: evidence from heating experiments on primitive meteorites. *Planetary and Space Science*, **43**, pp. 451–468.

Zhang, H. L. et al. (2018). Determination of Fe3+/ΣFe of XANES basaltic glass standards by Mössbauer spectroscopy and its application to the oxidation state of iron in MORB. *Chemical Geology*, **479**, pp. 166–175.

Please cite the published version in GCA: Wieser et al., 2020,
https://doi.org/10.1016/j.gca.2020.05.018

Appendix A: Chalcophile elements track the fate of sulfur at Kīlauea Volcano, Hawai'i

*Penny E. Wieser[1], Frances E. Jenner[2], Marie Edmonds[1]
John Maclennan[1] and Barbara E. Kunz[2]

[1]Department of Earth Sciences, University of Cambridge,
Downing Street, Cambridge, UK, CB2 3EQ.

[2]School of Environment, Earth and Ecosystem Sciences
The Open University, Walton Hall, 7 Milton Keynes, Buckinghamshire, MK7 6AA.
***Corresponding Author: penny.wieser@gmail.com**

1. Additional Figures

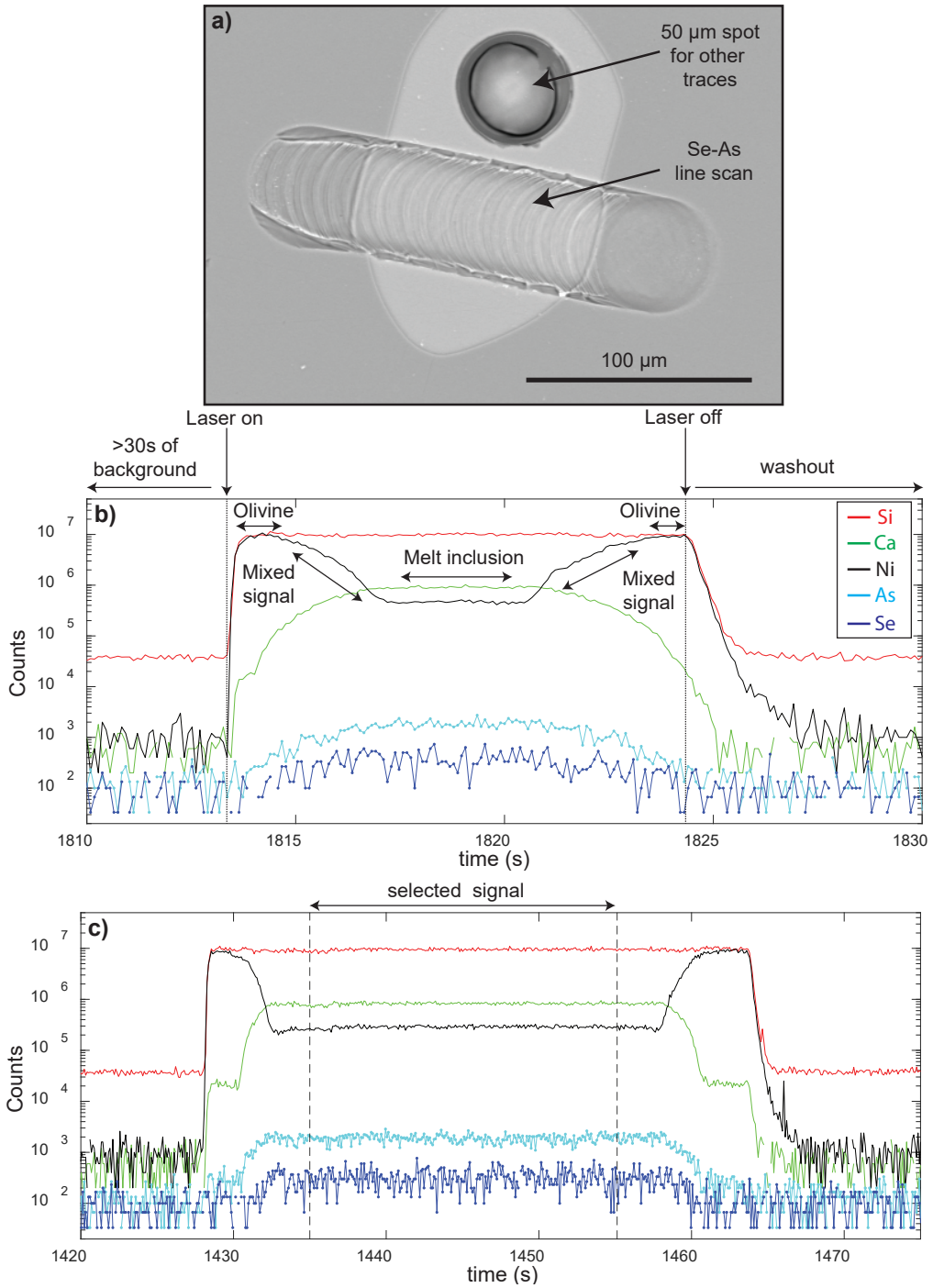

Figure A1: Examples of Se-As line scans. **a)** BSE image of melt inclusion with a 50 μm laser spot and a Se-As line scan. **b)** Raw signal for the Se-As line scan shown in **a)**. The line scan starts in the host olivine crystal (which has high Ni, and low Ca contents). The rapid drop in Ni, and increase in Ca occurs as the signal from the melt inclusion and host olivine mix, with a flat plateau in these elements once the signal derives from just the melt inclusion. The selected signal in this instance was relatively short (2.04 s) due to the relatively small size of the melt inclusion. **c)** Line scan signals from a significantly larger melt inclusion (selected signal = 20.1 s).

Table A1: Information for samples analysed in this study. Melt inclusion analyses were conducted on samples indicated with an asterisk (*). The other samples were examined for sulfide occurrence.

Sample Code	Eruption Date	Description	Location	GPS
KL0908*	Dec 30th, 1969	Ep. 12 Mauna Ulu	ERZ	19° 20.839' N, 155° 12.518' W
KL0910*	Nov 10th, 1973	Pau'ahi Crater	ERZ	19° 22.313' N, 155° 13.510' W
KL0916*	Aug 14th, 1971	Spatter ramparts in summit caldera	Intracaldera	19° 24.137' N, 155° 16.644' W
KL0919*	Late Dec, 1974	Ka'u Desert	SSWRZ	19° 22.649' N, 155° 17.609' W
KL0920	Late Dec, 1974	Ka'u Desert	SSWRZ	19° 22.603' N, 155° 17.713' W
KL0905	July 19th-22nd, 1974	Lua Manu Crater	Extracaldera	19° 23.935' N, 155° 15.337' W
KL0914	September 24th-29th , 1971	Spatter ramparts in summit caldera	Intracaldera	19° 24.580' N, 155° 16.631' W
KL0921	~1700 CE	Spatter ramparts	SSWRZ	19° 22.989' N, 155° 17.464 'W

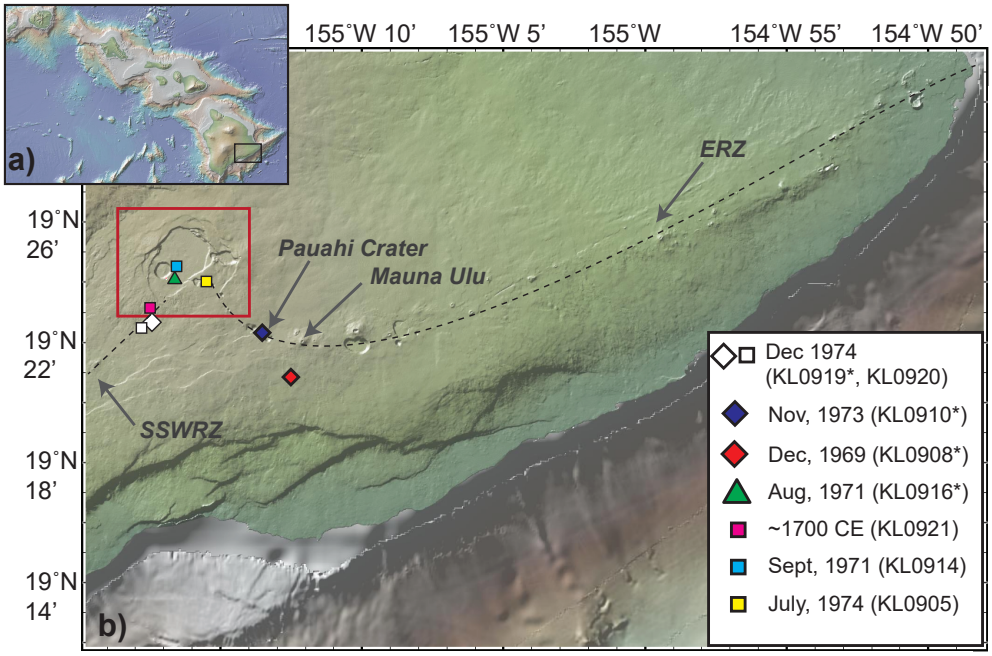

Figure A2: Sample locations for eruptions examined in this study. Samples used for melt inclusion work are indicated with an asterisk. Other samples shown were found to contain sulfides during BSE-SE mapping. Maps were produced in GeoMap App (`http://www.geomapapp.org`; Ryan et al. 2009), and show the topography of Kīlauea before the onset of the 2018 summit collapse.

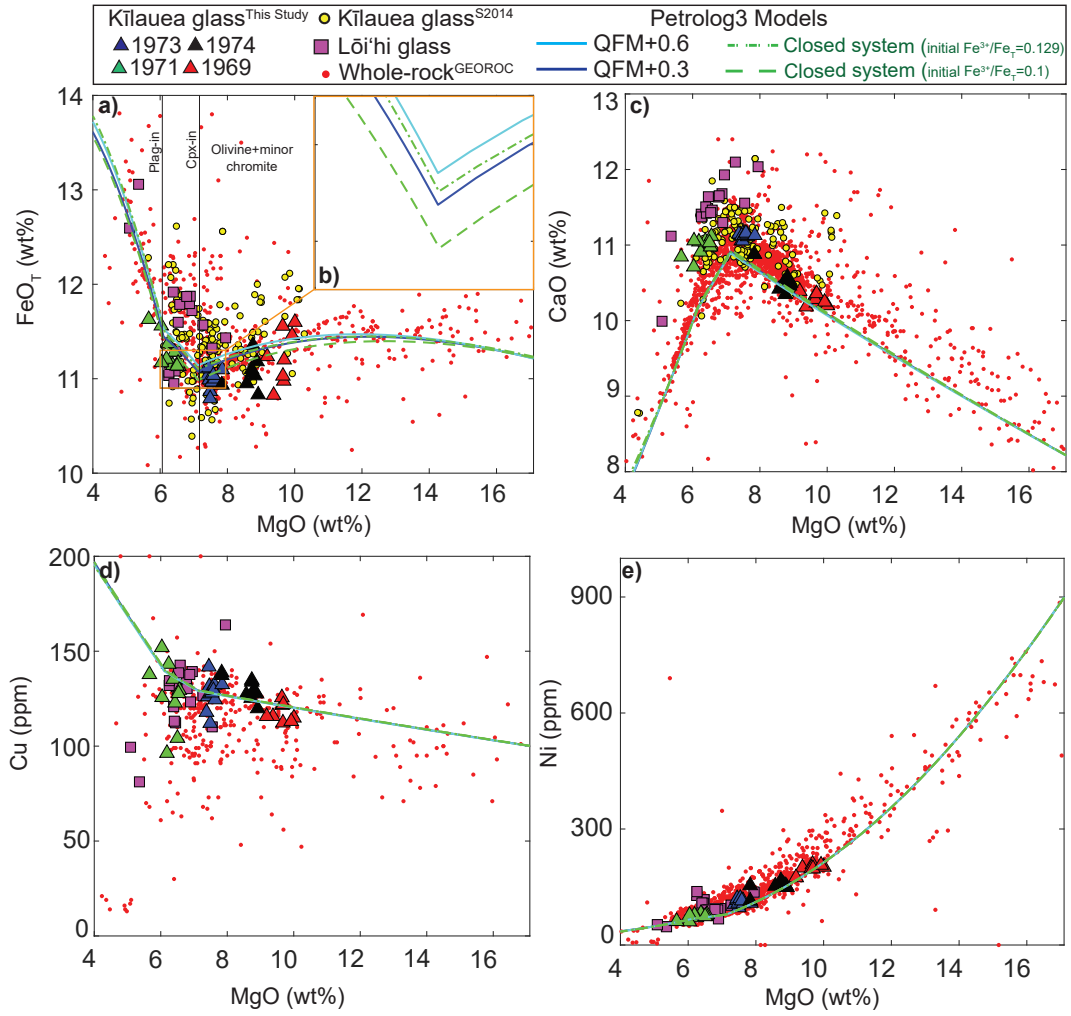

Figure A3: **a-c)** Glass major element compositions demonstrate that the three rift eruptions investigated in this study (1969, 1973, 1974) have not fractionated beyond olivine control. The 1971 summit eruption shows a relative enrichment in FeO, and depletion in CaO, indicative of clinopyroxene fractionation. Lōi'hi glasses are more evolved, plotting along a trajectory of clinopyroxene and plagioclase fractionation. Kilauean glass compositions from Sides et al. (2014) and whole-rock measurements from GEOROC are overlain. Fractionation paths from Petrolog3 are shown for buffered and closed systems. The major and trace element trajectories of these models are extremely similar (see inset **b**). The FeO_T content of primary melts was reduced from that of Clague et al. (1991) by 3.2% to improve the model fit. Particular detail was paid to the fit of FeO_T as this strongly controls the SCSS. **d-e)** This fractionation model with Ni_i=900, and Cu_i=100 recreates available Ni and Cu data (model details in main text).

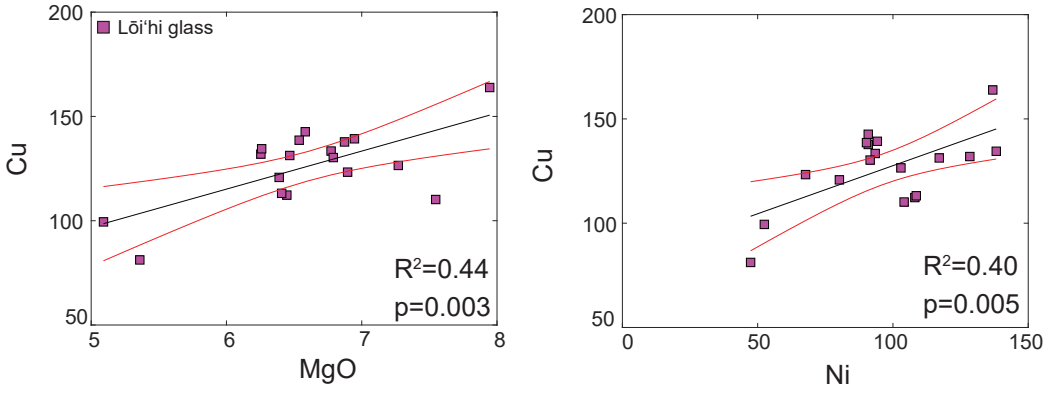

Figure A4: Lōi'hi glasses show a positive correlation between Cu and MgO, and Cu and Ni (indicative of sulfide fractionation).

Figure A5: A large sulfide within a small olivine-hosted melt inclusion (host Fo=87.5). From a mass balance perspective, due to the large volume fraction of the sulfide, it is not possible that this sulfide grew after melt inclusion entrapment (the melt would have needed 5-15 wt% Cu and Ni).

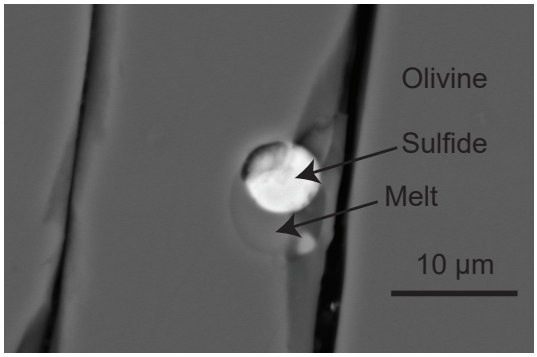

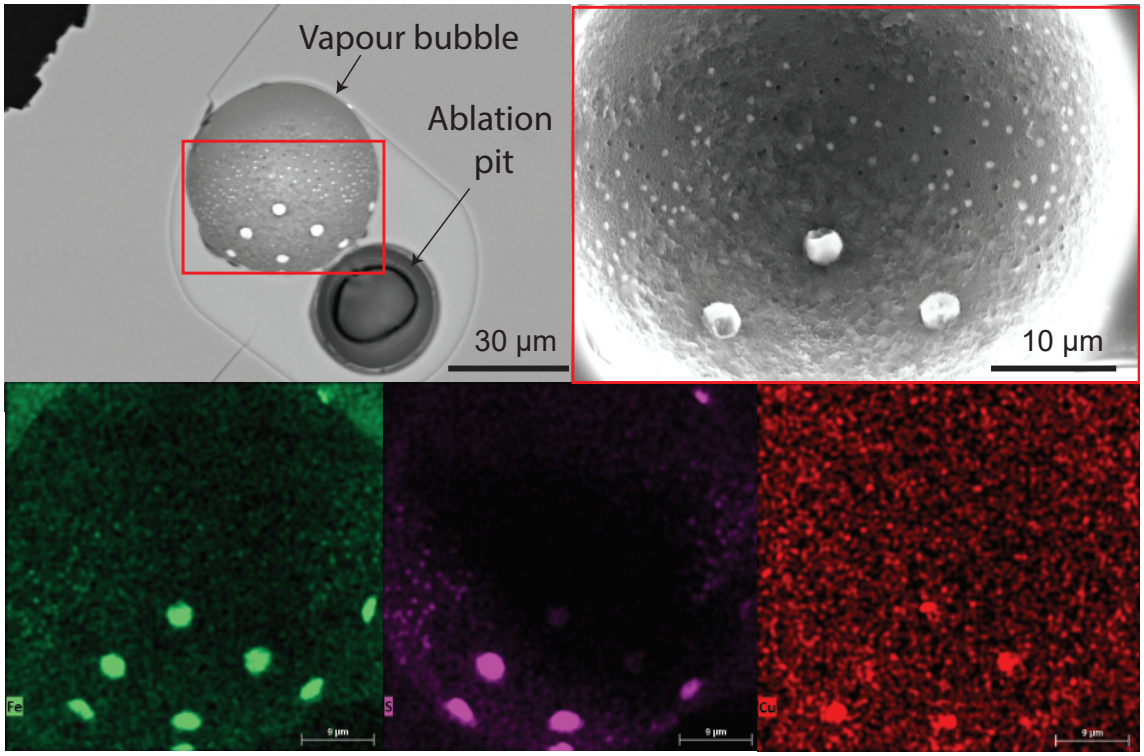

Figure A6: Bimodal-sized Fe-Cu rich sulfides within a melt inclusion vapour bubble.

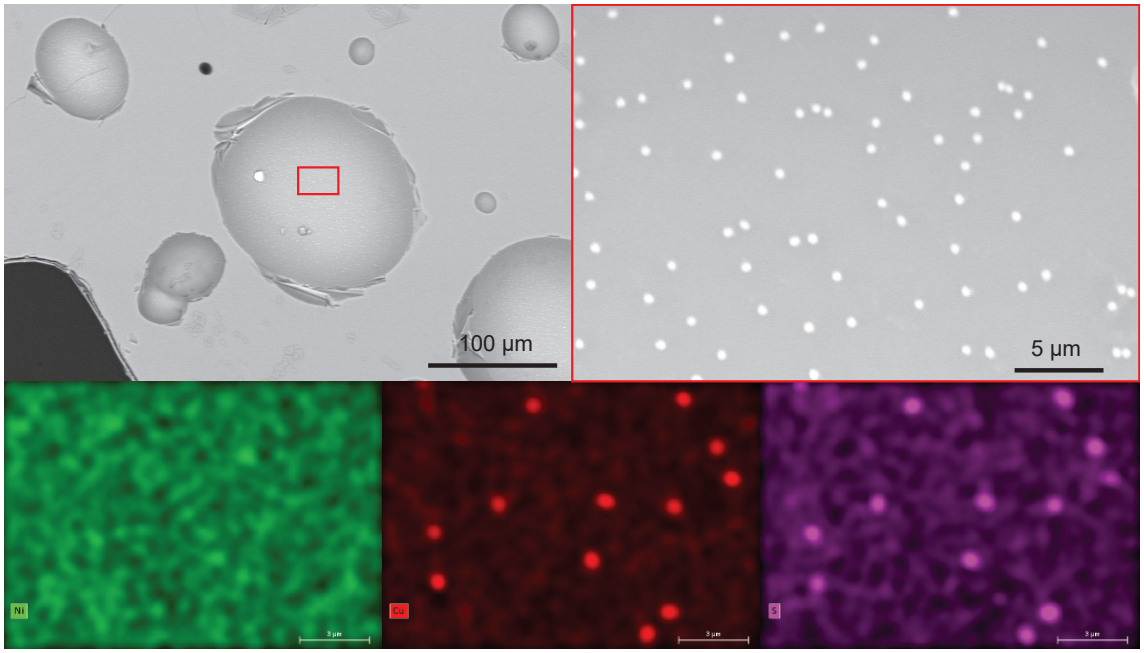

Figure A7: Tiny Fe-Cu-rich sulfides within matrix glass vesicles.

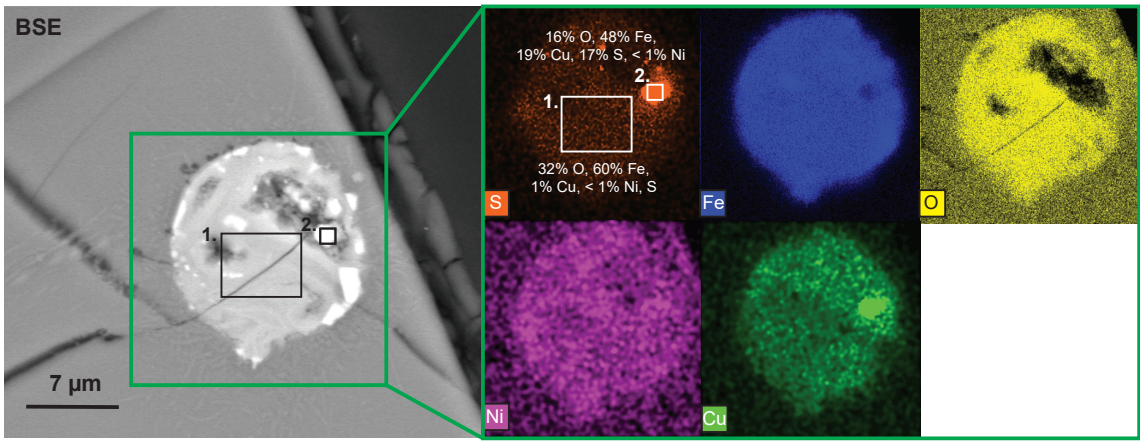

Figure A8: A broken down sulfide within degassed matrix glass. Area 1 is almost entirely composed of iron oxides, while area 2 is still relatively sulfur and copper-rich (although it also contains significant amounts of O, unlike pristine sulfides; see Fig. A9).

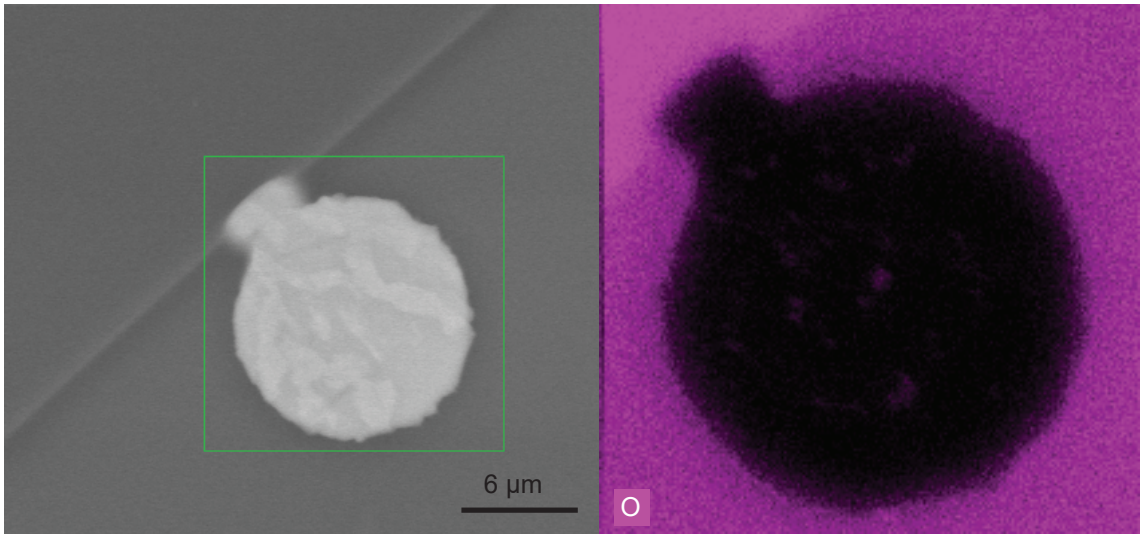

Figure A9: Map of O in a sulfide which does not show textural evidence for resorption. The sulfide is very O-poor (compare to Fig. A8, Fig. 6).

Figure A10: The range of fractionation-corrected Ba concentrations in matrix glasses from the three rift eruptions indicate that the mantle source experienced melt extents of ~F=0.08–0.095 (for Ba_i=6.85; Palme and O'Neill, 2014). Other incompatible trace elements such as La and Ce give similar F values.

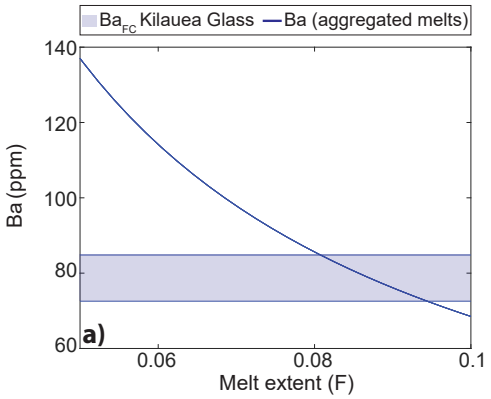

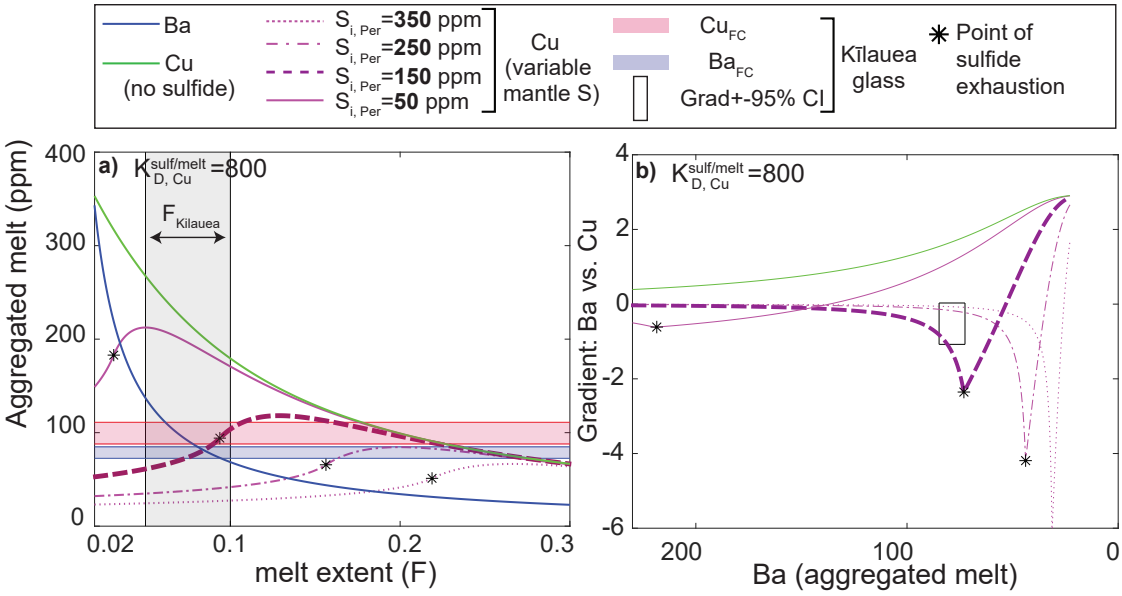

Figure A11: Models for S_i=350, 250, 150 and 50 ppm. Although the S_i=150 ppm model scenario recreates observed Cu concentrations, if sulfides are exhausted, it doesn't mass through observed gradients or Ba concentrations.

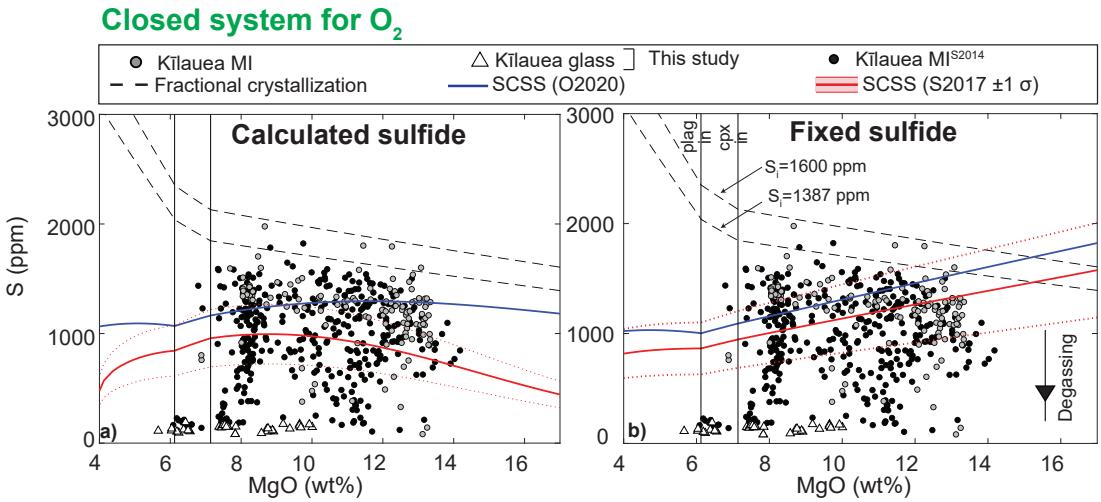

Figure A12: $SCSS^{2-}$ models for the closed system model ($Fe^{3+}/Fe_{T,initial}$=0.1). Using the calculated sulfide composition from the O2020 and S2017 model results in an $SCSS^{2-}$ that is significantly lower than measured melt inclusion S contents.

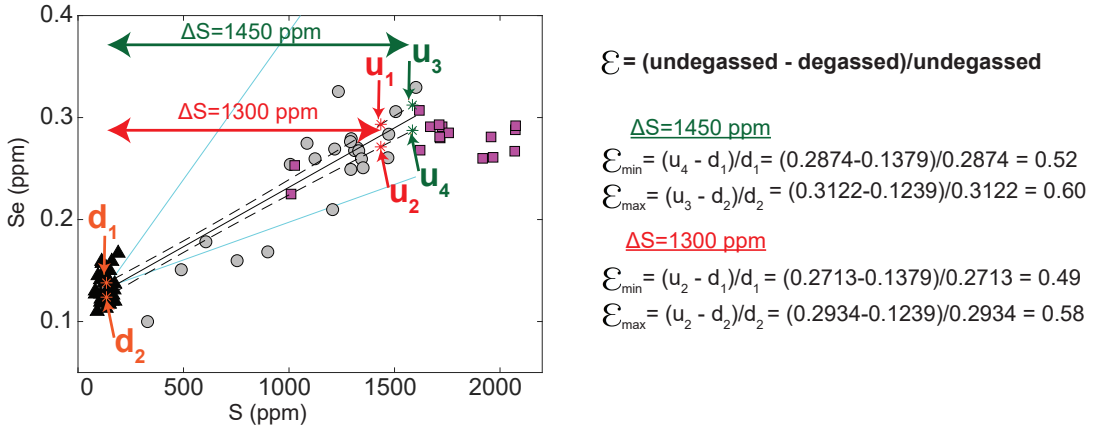

Figure A13: The upper and lower bounds of the 95% confidence interval on the regression of a given element against S were used to estimate an upper and lower bound on the emanation coefficient for each ΔS value.

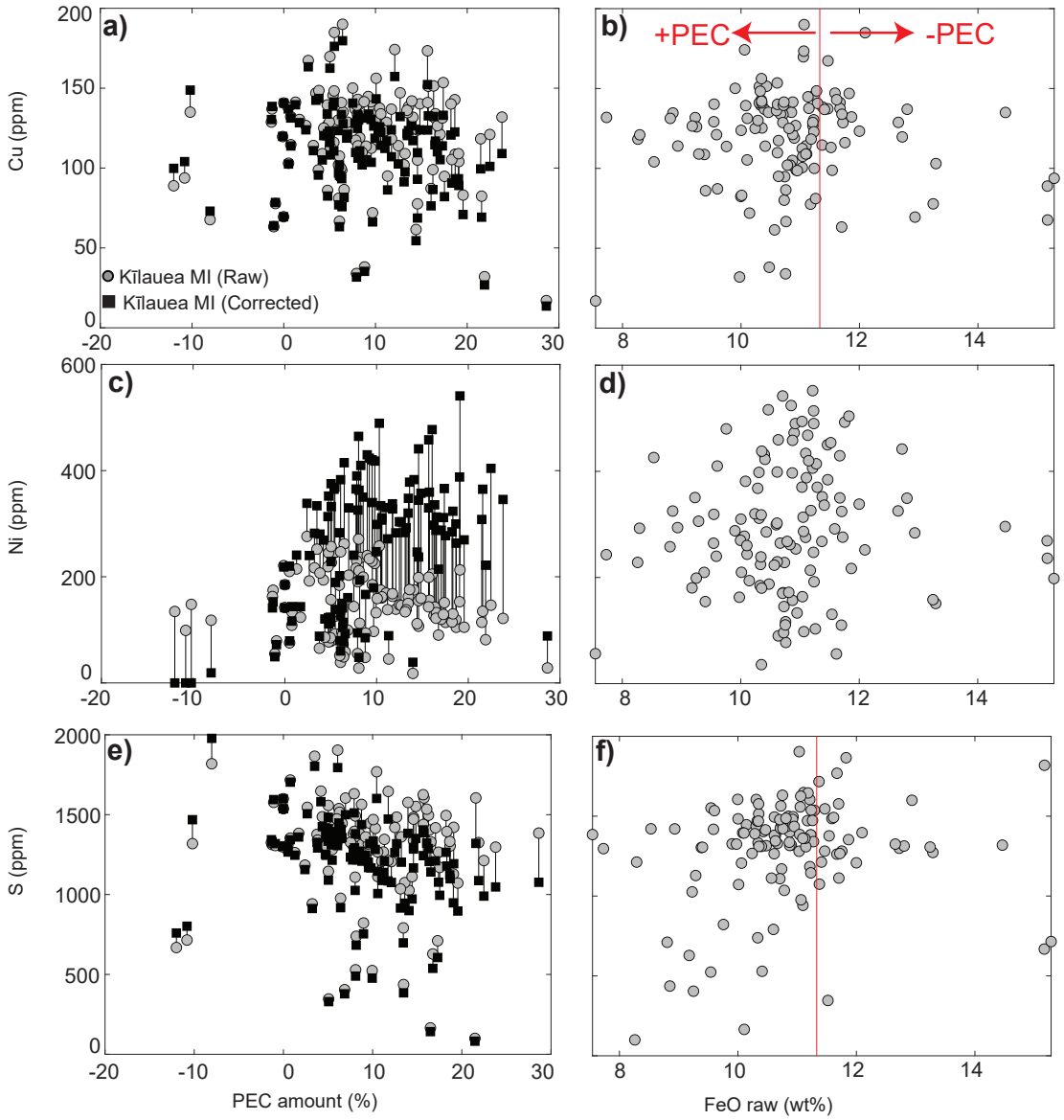

Figure A14: There is no correlation between the Ni and Cu contents of melt inclusions and the amount of PEC crystallization (calculated in Petrolog3), or the melt inclusion FeO content (which is inversely proportional to the amount of FeO loss). Due to their incompatible behaviour, the PEC correction does not alter the Cu or S contents by very much. Due to its compatability (here $K_{D,Ni}^{ol/melt}$ = 10.6), corrected Ni concentrations are significantly higher than raw data, but there are still no correlations with PEC amount of FeO.

2. Correcting Matrix Glass Compositions for Fractional Crystallization

The amount of olivine crystallization experienced by matrix glasses was calculated in Petrolog3 using the "Reverse Crystallization" tool, assuming primary melts contain 17.1 wt% MgO (Clague et al., 1991). Models were run using the olivine model of Danyushevsky, 2001, with K_D=0.3, at 1 kbar, using the QFM buffer and the model of Kress and Carmichael, 1988.

3. Mantle Melting Model Details

The concentrations of Cu and Ba in melts produced during melting of a sulfide-bearing mantle were calculated using an adapted version of the modelling approach of Lee et al. (2012). The composition of batch melts calculated at small F steps (termed instananeous melts, with 3001 steps between F=0 and F=0.3) were pooled to calculate the composition of the aggregated melt. Unlike the approach of Lee et al. (2012) where P and D in the batch melting equation are assumed to be equal, this approach considers the non model melting behaviour of sulfide in each step. These approaches converge as the Δ F tends to zero. In the equations below, the mass of the mantle residue (M) is used (where F=1–M). A Jupyter notebook performing these calculations is provided as an electronic supplement.

The change in the mass of the mantle residue during step i was calculated from M at the end of the previous melting step and M at the end of this melting step:

$$\Delta M^i = M^{i-1} - M^i \tag{1}$$

The proportion of melt produced at step i relative to the mass of the system at the start of that melting step was calculated from:

$$X^i_{F,\,Step} = \frac{\Delta M^i}{M^{i-1}} \tag{2}$$

The amount of S left in the residual mantle after each melting step was using a mass balance (Equations 10, 11):

$$[S]^i_{Residue} = \frac{[S]^{i-1}_{Residue} - [S]^i_{Melt} \times X^i_{F,\,Step}}{1 - X^i_{F,\,Step}} \tag{3}$$

Once sulfide was exhausted, $S_{Residue}$ was set to 0.

The proportion of sulfide was calculated from the S content of the residual mantle and the S content of mantle sulfides:

$$X^i_{Sulf} = \frac{S^i_{Residue}}{S_{Sulf}} \tag{4}$$

The change in the amount of sulfide during a given melting step was calculated from the change in the amount of S in the mantle during that step:

$$\Delta X^i_{Sulf} = \frac{S^{i-1}_{Residue} - S^i_{Residue}}{S_{Sulf}} \tag{5}$$

By mass balance, the change in the amount of silicate during a given melting step is equal to the amount of melt produced in that step minus the change in the amount of sulfide:

$$\Delta X^i_{Sil} = \Delta M^i - \Delta X^i_{Sulf} \tag{6}$$

The concentration of element [A] in instantaneous melts created at step i was calculated from the batch melting equation:

$$[A]^i_{Inst.\,melt} = \frac{[A]^{i-1}_{Residue}}{K^{i-1}_{D,Bulk} + (1 - P^i) \times X^i_{F,\,Step}} \tag{7}$$

Where $[A]^{i-1}_{Residue}$ is the concentration of element A in the mantle residue at the end of the previous step, P^i is the bulk distribution coefficient weighted by the proportion that each phase contributes to the melt. K^{i-1}_D is the bulk distribution coefficient of the solid residue following melt extraction in the previous step, calculated from:

$$K^{i-1}_{D,Bulk} = K_{D,Sil} \times (1 - X^{i-1}_{sulf}) + K_{D,Sulf} \times X^{i-1}_{Sulf} \tag{8}$$

Incorporating non-modal melting for silicates (rather than a constant value of $K_{D,Sil}$) requires accurate estimates of changing mineral modes at high pressures (problematic at >3 GPa, Ghiorso et al, 2002). Fixing the value of $K_{D,Sil}$ has negligible effects on modelled Cu concentrations, as $K_{D,\,Sulf}$ is 4–5 orders of magnitude higher than $K_{D,\,Sil}$, and silicate phases have similarly low partition coefficients (Table A2). $K_{D,\,Sil}$ was calculated assuming the mantle source contains 59.8% olivine, 21.1% orthopyroxene, 7.6% clinopyroxene and 11.5% garnet (Mckenzie and O'Nions, 1991). Silicate-melt partition coefficients from Ba are from Gibson and Geist (2010), and those for Cu are from Liu et al. (2014).

Element	Gnt-melt K_D	Cpx-melt K_D	Opx-melt K_D	Ol-melt K_D
Ba	0.00007	0.0004	0.000006	0.000005
Cu	0.03	0.06	0.04	0.05

Table A2: Silicate-melt K_Ds used in mantle melting models

The fraction of silicate and sulfide phases in the melting assemblage were calculated by dividing ΔX^i_{Sil} and ΔX^i_{Sulf} by the proportion of melt produced in this step (ΔM^i). These fractions were then multipled by their respective partition coefficients to calculate P:

$$P^i = K_{D,\,Sil} \times \frac{\Delta X^i_{Sil}}{\Delta M^i} + K_{D,\,Sulf} \times \frac{\Delta X^i_{Sulf}}{\Delta M^i} \tag{9}$$

Mass balance equations were written for the concentration of element A in the peridotite residue at the end of the previous melting step, the end of this melting step, and the composition of the instantaneous melt produced in this step:

$$[A]^{i-1}_{Residue} = [A]^i_{Residue} \times (1 - X^i_{F,\,Step}) + [A]^i_{Inst.\,melt} \times X^i_{F,\,Step} \tag{10}$$

Re-arranging for $[A]^i_{Residue}$ gives the form shown in Equation. 3:

$$[A]^i_{Residue} = \frac{[A]^{i-1}_{Residue} - [A]^i_{Inst.\,melt} \times X^i_{F,\,Step}}{1 - X^i_{F,\,Step}} \tag{11}$$

Similarly, aggregated melt compositions were calculated from the instantaneous melts using mass balance between the aggregated melt at the end of the previous step, and the instanteous melt produced in this step:

$$[A]^i_{Agg.\,melt} = [A]^{i-1}_{Agg.\,melt} \times (1 - X^i_{F,Start}) + [A]^i_{Inst.\,melt} \times X^i_{F,Start} \tag{12}$$

Note that instead of using the proportion of melt produced in a given step ($X^i_{F,\,Step}$), this equation uses the proportion of melt produced in this step compared with the total amount of melt produced from the very start of the model:

$$X^i_{F,Start} = \frac{\Delta M^i}{M^1 - M^i} \tag{13}$$

Where M^1=1.

4. Analytical Methodology

Details of EPMA analysis and LA-ICP-MS analysis of lithophile elements can be found in Wieser et al., 2019.

4.1. EDS Analysis

EDS maps were collected using two 3||60 Bruker flash detectors (90 kcps) at 20 kV, with a spot size of 4.5, for 15–20 minute acquisition times. To allow assessment of the precision and accuracy of this method, a pyrite (UWPy-1), chalcopyrite (Nifty) and pentlandite (GLAHM) standard were characterized using the Cameca SX100 EPMA in the Department of Earth Sciences, University of Cambridge (standards kindly provided by John Craven and Sally Gibson). Ni, Cu, Se and Fe were analysed at 20 kV, 20 nA, using a 5 μm spot. Crystals, calibration materials and acount times are shown in Table A3.

Element	Crystal	Calibration Material	Peak Count Time
S	PET	Pyrite	10 s
Cu	LLIF	Cu metal	30 s
Ni	LIF	Ni metal	30 s
Fe	LIF	Pyrite	10 s

Table A3: Analytical conditions for characterization of in-house sulfide standards.

During each analytical session, EDS maps of small (10–30 μm) areas of thse three in-house standards were collected using the same analytical conditions as maps of unknown Kīlauean sulfides. The spectra from all mapped areas were quantified in Esprit2.1 software, using a P/B ZAF model. Comparison of EPMA and EDS data for

the sulfide standards demonstrated that the automatic background fit in Esprit2.1 results in a significant underestimation of S concentrations, due to an anomalous background window close to the low energy Skα peak. Deletion of this background window resolved this discrepancy, and was performed during quantification of each spectra. For Kīlauean sulfides, maps were quantified for a hand-drawn area to exclude the outer rim of each sulfide (which exhibited a mixed spectra with significant contributions from the host olivine/glass, assessed by quantifying the Si, Mg and Ca peak). Based on repeated maps of in-house sulfide standards, precision for EDS quantification was less than 1%, and the accuracy relative to EPMA measurements of these standards was within $\pm$5%. EDS results were corrected for consistent offsets from EPMA measurements by a factor of 0.96 for Fe, and 1.025 for Ni and Cu.

4.2. LA-ICP-MS Analyses

Two separate analytical conditions were used for LA-ICP-MS analysis. All reported concentrations of elements except Se and As were analysed in the "trace element" routine (although this was altered slightly for 25 μm spot sizes). All analyses were conducted with a fluency of 3.63 J/cm^2, 0.9 l/min of He, 0.77 l/min of Ar carrier gas, and 15 l/min of Ar plasma gas. 5 ml/min N_2 was added downstream for trace element spots sizes of 25 μm, and Se-As analyses, to increase sensitivity. Additional information is provided below:

	Background	Signal length	Repetition rate	Scan Speed	Oxygen Flow
Spot analyses (trace elements)	30 s	20 s	10 Hz	N/A	N/A
Spot analyses (Se+As)	30 s	20 s	20 Hz	N/A	N/A
Line scans (Se+As)	30 s	dependent on line length	50 Hz	50 μm/sec	0.47 l/min

Table A4: Conditions for spot and line LA-ICP-MS analyses

Se-As line scans started and ended in the surrounding olivine to maximise the length of the useable signal. In order to select the signal from the melt inclusion (rather than a mixed signal between the melt inclusion and the surrounding olivine), we analysed masses ^{29}Si, ^{43}Ca, ^{60}Ni, ^{75}As (shifted to ^{91}As) and ^{80}Se (shifted to ^{96}Se). The signal from the olivine is characterized by low Ca and high Ni. As the laser starts ablating the host olivine and melt inclusion, a mixed signal is acquired, characterised by rapidly decreasing Ni concentration as the line scan moves further into the melt inclusion. Signals were selected based on the presence of a flat Ni plateau, and the concentrations from this plateau were compared to the Ni concentrations collected during spot analysis of the same inclusion (Supplementary Fig. A1).

Additional References

1. Gibson, S.A. and Geist, D., 2010. Geochemical and geophysical estimates of lithospheric thickness variation beneath Galápagos. Earth and Planetary Science Letters, 300(3-4), pp.275-286.
2. McKenzie, D., and O'Nions, R., 1991, Partial melt distributions from inversion of rare earth element concentrations. Journal of Petrology, 32, no. 5, p. 1021-1091.
3. Ryan, W. B. F. et al. Global multi-resolution topography synthesis. Geochem. Geophys. Geosyst. 10, 1–9 (2009).